NASA TECHNICAL MEMORANDUM

NASA TM X-1331

NASA TM X-1331

FLIGHT TEST AND ANALYSIS OF A METHOD FOR REDUCING RADIO ATTENUATION DURING HYPERSONIC FLIGHT

by William F. Cuddihy, Ivan E. Beckwith, and Lyle C. Schroeder

Langley Research Center
Langley Station, Hampton, Va.

NATIONAL AERONAUTICS AND SPACE ADMINISTRATION • WASHINGTON, D. C. • MARCH 1967

CLASSIFICATION CHANGED

FLIGHT TEST AND ANALYSIS OF A METHOD FOR REDUCING

RADIO ATTENUATION DURING HYPERSONIC FLIGHT

By William F. Cuddihy, Ivan E. Beckwith,
and Lyle C. Schroeder

Langley Research Center
Langley Station, Hampton, Va.

GROUP 4
Downgraded at 3 year intervals;
declassified after 12 years

NATIONAL AERONAUTICS AND SPACE ADMINISTRATION

CONTENTS

FLIGHT TEST AND ANALYSIS OF A METHOD FOR REDUCING
RADIO ATTENUATION DURING HYPERSONIC FLIGHT*

By William F. Cuddihy, Ivan E. Beckwith,
and Lyle C. Schroeder
Langley Research Center

SUMMARY

A method of overcoming ionization blackout of radio communication from a hypersonic vehicle by injecting water into the flow field was verified by a flight test. The test vehicle was a 9° half-angle cone-cylinder with a spherically blunted nose of 4-inch (10.2-cm) radius. Attenuation levels with and without water injection were measured during the ascending portion of the trajectory for radio frequencies of 30.8, 225.7, 244.3, 5600, and 9210 megacycles. Data were obtained up to the peak altitude of 290 000 feet (88.4 km). The maximum flight velocity was 17 840 feet per second (5.438 km/sec). Water was injected intermittently from orifices located in the stagnation region and just aft of the sphere-cone junction. Water injection was found to cause complete or substantial recovery of the 30.8-, 225.7-, and 244.3-megacycle signals. The 244.3-megacycle signal was completely blacked out during periods of no injection. The 5600- and 9210-megacycle signals were not noticeably attenuated at any time throughout the flight test. For the flight test conditions, stagnation injection was more efficient than side injection.

Various mechanisms that could be responsible for the reduction in free electrons and subsequent signal recovery are discussed and analyzed. During stagnation injection, the mechanisms of aerodynamic shaping (modification of the bow shock to a pointed shape) and stagnation cooling may have contributed to the reduction of free electrons. For side injection, the analysis indicates that homogeneous cooling due to evaporation and dissociation of the injected water could contribute significantly to electron removal if ionized gas flow times in the vicinity of the vehicle were large compared with recombination times. Calculations indicate, however, that heterogeneous reactions which occur on or near the surface of the water droplets are the predominant mechanism for electron removal during side injection.

---

*Title, Unclassified.

The loss of radio communication with hypersonic vehicles is known to be caused by the free electrons in the plasma layer that surrounds the vehicle. Free electrons in the plasma interact with electromagnetic radiation to and from the vehicle and cause signal attenuation (refs. 1 to 5, for example). The plasma results from thermal ionization of the constituents of the air as it is compressed and heated by the strong bow shock or heated within the boundary layer next to the surface (refs. 2, 4, and 6). In general, when the plasma frequency approaches the radio-signal frequency, the signal is greatly attenuated or lost altogether. The plasma frequency is proportional to the square root of the concentration of free electrons in the ionized gas. It would therefore be expected that the addition of a foreign material which tends to reduce the electron concentration would also have the effect of improving radio transmission. This effect has been observed in the present flight experiments as well as in ground facility tests (refs. 7 and 8), in a flight test in which signal attenuation due to rocket exhaust was observed (ref. 9), and in a Gemini-Titan 3 experiment (refs. 10 and 11).

There are several possible mechanisms that might account for the reduction in free electron concentration due to material addition: (1) increased recombination of electrons and ions and increased molecular or atomic attachment of electrons as a result of reduced temperatures and increased density (homogeneous cooling and electrophilic action); (2) reduced ion formation in the stagnation region during stagnation injection (stagnation cooling effect); (3) modification of the bow shock shape by forward injection from the stagnation region (aerodynamic shaping); (4) recombination of electrons with ions on or near the surface of solid particles or droplets (heterogeneous reactions); and (5) attachment or absorption of electrons at the surface of particles or droplets (surface attachment). In any given situation, one or more of these mechanisms could be responsible for the observed effects, depending on the flow configuration, mode of injection, and composition of the injected material. Methods are well developed for the quantitative evaluation of electron concentration and distribution in the uncontaminated flow fields of hypersonic vehicles (refs. 6, 12, 13, and 14). When foreign materials are added, either as products of ablation or for the purpose considered herein, the cooling action can be evaluated if all chemical and evaporation processes are assumed to be in equilibrium. For typical flight conditions where nonequilibrium effects predominate, the chemical reactions and their rate constants for both homogeneous and heterogeneous reactions are not well known. Also, in the case of water addition, the important parameters of liquid droplet size, evaporation rates, and other fluid mechanics aspects of the flow are not well known. For these reasons, accurate calculations of the effects of water addition on the plasma characteristics are not yet possible. Estimates of the electrophilic action of carbon tetrachloride have been made in reference 15. In reference 16, a theoretical analysis of the

2

effect of recombination of electrons and ions at the surface of droplets is given. The results of these investigations indicate that, with the assumptions and conditions used, the electrophilic action of some gases and recombination on the surface of droplets may both be very effective in reducing electron concentrations.

In reference 17, an experimental study of the effects of water sprays on suppressing ion and electron concentrations in seeded laboratory combustion plasmas is described. The results indicated that free electron concentrations are reduced very rapidly by three or four orders of magnitude by ion-electron recombination processes involving the water droplets as sticky third bodies, that is, by heterogeneous recombination processes. The results of reference 17 also indicated that attachment or electrophilic processes were not important for water addition. In reference 11, a quasi-one-dimensional method for estimating the effects of water injection on the flow conditions and electron concentrations in the shock layer of a supersonic vehicle was applied to the same flight conditions as those of the present report. The results indicated that the principal mechanism for electron suppression with side injection during the RAM B2 flight was the heterogeneous reactions. Furthermore, the values of an efficiency factor for the heterogeneous recombination of electrons and ions as deduced from the flight results can be shown to be in good agreement with the laboratory results of reference 17 and the theoretical predictions of reference 16.

The effectiveness and efficiency of mechanisms (1), (2), (4), and (5) depend on the proper location, penetration, and distribution of the injected material in the flow field. Mechanism (3) may depend primarily on the forward momentum of the injected liquid. These fluid mechanics aspects of the problem have been considered in reference 18, which is a report of an experimental and theoretical investigation of liquid injection and evaporation processes in the flow fields of hypersonic vehicles.

The complete simulation of a reentry plasma and other flight conditions is not possible in a ground facility. Therefore, the RAM B2 flight was undertaken with the principal objective of testing the concept of electron suppression by water injection under actual reentry blackout conditions. Secondary objectives were to determine the amount of water required to alleviate blackout and to examine the relative effects of injection from the stagnation point and from the sides of the vehicle. This report presents the radio attenuation data obtained. Possible mechanisms for electron suppression are analyzed in some detail in relation to the flight results and conditions. The flight test was carried out as part of the RAM (Radio Attenuation Measurement) research program at the NASA Langley Research Center. References 19 to 29 give some results obtained in this program. A preliminary report of the attenuation results of the present flight test is given in reference 30. The RAM B2 vehicle design and performance are given in reference 31.

The RAM B3 vehicle, which was identical in size and shape to the present vehicle, was flown on April 10, 1964. The primary purpose of the RAM B3 flight test was to obtain local measurements of electron concentration in an uncontaminated flow field, that is, for no material addition. Experimental results and a preliminary analysis are given in reference 32. Complete flow field calculations for the RAM B3 flight are reported in reference 33. Since the RAM B3 trajectory was essentially the same as that of the present test vehicle, the data obtained in the test of reference 32 and the calculations of reference 33 are applicable to the present conditions during water-off periods.

Appendix A of this report, by Ivan E. Beckwith, Dennis M. Bushnell, and J. L. Hunt, presents an analysis and calculations of a cooling mechanism for reduction in electron concentration. Ivan E. Beckwith and Sadie P. Livingston wrote appendix B, which presents a quasi-one-dimensional theory for mean droplet motion and evaporation. Appendix C, by Ivan E. Beckwith, presents an analysis of free electron depletion by heterogeneous reactions.

SYMBOLS

The units used for the physical quantities defined in this paper are given both in the U.S. Customary Units and in the International System of Units (SI). Factors relating the two systems are given in reference 34.

A — cross-sectional area of flow, feet^2 $\left(\text{meters}^2\right)$; or function of M in equation (B14) for drag coefficient (see appendix B and table III)

C_D — droplet drag coefficient

$C_{D,B}$ — body drag coefficient

$C_{D,C}$ — continuum droplet drag coefficient (appendix B)

$C_{D,FM}$ — free molecule droplet drag coefficient (appendix B)

$\left(C_D\right)_{M=0}$ — droplet drag coefficient for $M = 0$

C_p — pressure coefficient

$\bar{C}_p$ — pressure coefficient normalized with respect to stagnation point value, $\dfrac{C_p}{C_{p,max}}$

c_p specific heat

$\bar{c}_p$ frozen specific heat

D_B total body drag back to station 2, pounds force (newtons)

d   model nose diameter, feet (meters)

d_O orifice diameter, inches (centimeters)

E   voltage

F   force, pounds force (newtons)

f   frequency, cycles/second

f_c capture efficiency factor (eq. (C6) of appendix C)

$\bar{f}_c$ mean effective value of f_c

f_i fraction of intercepted flow contained in end of mixing region

f_O resonant frequency, cycles/second

Δf frequency difference required to give a VSWR of 3 on either side of resonance, cycles/second

H   stagnation enthalpy per unit mass, feet^2/second^2 (Joules/kilogram); or hydrogen

h   static enthalpy per unit mass, feet^2/second^2 (Joules/kilogram)

k   thermal conductivity

L   latent heat of liquid

M   Mach number

$\overline{M}$ molecular weight

m	mass, pounds (kilograms)
$\dot{m}$	mass flow rate, pounds/second (kilograms/second)
N	number of injection orifices or nitrogen
N_e	electron number density, electrons/cm^3
N_d	droplet number density, droplets/cm^3
N_{Nu}	Nusselt number for heat transfer to droplets
$N_{Nu,C}$	continuum Nusselt number (eq. (B19))
$N_{Nu,FM}$	free molecule Nusselt number (eq. (B20))
N_{Pr}	Prandtl number
$N_{Re,f}$	film Reynolds number, $\dfrac{\rho_m V2r}{\mu_f}$
N_{St}	free molecule Stanton number (eq. (B21))
n	function of M in equation (B14) for drag coefficient (appendix B)
$\bar{n}$	number of free electrons removed from gas flow per drop
p	pressure, pounds/$foot^2$ or atmospheres (Newtons/$meter^2$) (1 atm = 1×10^5 N/m^2)
p_a	ambient pressure near injection site
Q	characteristic number for antenna bandwidth, $\dfrac{f_o}{\Delta f}$
q	heat-transfer rate per unit area to droplet
R	ratio of droplet radius to the initial value, $\dfrac{r}{r_1}$
$\bar{R}_m$	gas constant of mixture, $\dfrac{\mathcal{R}}{\bar{M}_m}$

$\mathcal{R}$	universal gas constant, energy/mole
r	droplet radius, feet (microns) (1 micron = 1 micrometer)
$\bar{r}$	radius of effective capture cross section of droplet
r_B	body radius of vehicle
r_i	radius of intercepted stream tube (see appendix A)
r_N	nose radius of vehicle, inches (centimeters)
r_2	radius to r_i streamline at station 2 (appendix A)
S	speed ratio, $\dfrac{V}{\sqrt{2\bar{R}_m T}}$
T	temperature, ^{O}Rankine (^{O}Kelvin)
T^*	momentum ratio parameter, $\left(\dfrac{\dot{m}_c}{\dot{m}_{ref}}\right)\left(\dfrac{V_l}{V_\infty}\right)$
t	time, seconds
V	velocity, feet/second (meters/second)
V_d	droplet velocity, feet/second (meters/second)
V_e	mean thermal electron velocity, feet/second (meters/second)
V_l	liquid velocity at injection site, feet/second (meters/second)
$\bar{V}$	specific mass flow parameter, $\dfrac{\rho_l V_l}{\rho_\infty V_\infty}$
W^*	ratio of coolant mass flow to air mass flow entrained in mixing region, $\dfrac{\dot{m}_c}{\dot{m}_a}$
X,Y	body coordinate axes with origin at injection site and X-axis alined with free stream (see sketch (a) in appendix A)
x	distance along X-axis, inches (meters)
X_i	mole fraction of species i

y_{max} — maximum penetration of liquid spray in Y-direction, inches (meters)

Δy_{max} — distance in Y-direction from vehicle surface to maximum spray penetration, inches (meters)

z — altitude, feet (meters)

β — constant in exponential expression for atmospheric density

γ — ratio of specific heats

δ_x — bow shock standoff distance (or forward penetration of liquid jet or spray), feet (meters)

δ_y — shock layer thickness in Y-direction, inches (meters)

$\eta_{r,0}$ — droplet recovery factor for zero mass transfer

$\eta_{r,FM}$ — free molecule recovery factor for sphere

θ — semivertex angle of cone

θ_i — injection angle of liquid (appendix A)

θ_s — angular spread of liquid spray in lateral direction (appendix A)

μ — viscosity

ρ — density, pounds/foot^3 (kilograms/meter^3)

Subscripts:

a — air

av — average

aw — for zero heat transfer at surface of droplet

c — coolant

8

e   electron

f   evaluated at mean temperature of droplet film

g   gas just upstream of injection site

l liquid

m   mixture of air and water vapor

max   maximum value

min   minimum value

ref   reference quantity

s   saturated liquid or vapor

t   total

v   vapor

w   surface of droplet

x   X-direction

y   Y-direction

0   just upstream of injection site, or for zero mass transfer

1   at injection site

2   downstream station at end of mixing region

∞ free stream ahead of bow shock

APPARATUS

Launch Vehicle

The launch vehicle was an unguided, three-stage configuration with solid propellant rocket motors. It was designed to place a 175-pound (79.5-kg) payload on an ascending trajectory at an altitude of 180 000 feet (54.9 km) with a velocity of about 18 000 ft/sec (5.5 km/sec). The first and second stages consisted of the Castor-E8 and Antares-IA1 rocket motors, respectively, and were aerodynamically stabilized by means of swept fins. The third stage consisted of the Alcor rocket motor and the test vehicle, which was flare stabilized. Shortly after launch the vehicle was spun up to approximately 3 revolutions per second by means of two Hotseat rocket motors attached on opposite sides of the first-stage motor. Figure 1 is a drawing of the vehicle. Complete details on the rocket motors and construction of the launch vehicle are given in reference 31.

Test Vehicle

The test vehicle or payload was a 9° half-angle cone-cylinder-flare configuration with a spherically blunted nose of 4-inch (10.2-cm) radius. The diameter of the cylindrical section was 22 inches (55.8 cm). The total length of the test vehicle including the 13° half-angle flare was 138.2 inches (351 cm). In order to provide a flow field with a minimum of ablation products, the forward portion of the vehicle was constructed of a beryllium shell that varied in thickness from 1.5 inches (3.81 cm) at the stagnation point to 0.16 inch (0.4 cm) at the downstream end. The axial length of this beryllium heat sink was 18.81 inches (47.8 cm). The rest of the test vehicle was protected by an ablation material consisting of a modified epoxy resin. Figure 2 shows the antenna locations and the injection sites, and figure 3 shows the internal arrangement of the water tank, the rotary distribution valve, and other equipment in the nose portion of the vehicle. A complete description of the test vehicle including the interior layout and construction detail is given in reference 31.

Communications Systems

Radio-frequency systems.- The radio-frequency (rf) systems flown are described in order of the location of their antennas, beginning with the most forward and proceeding aft. Information about antenna station, signal frequency, antenna gain, voltage standing-wave ratio (VSWR), bandwidth, transmitter power, and signal margin is given in the following table. The signal margin from the vehicle to the Wallops Island station was calculated for the vehicle location at the time of third-stage burnout (the time of maximum velocity).

Vehicle antenna station		Frequency, Mc/sec	Antenna gain, dB (a)	VSWR	Bandwidth, Mc/sec	Transmitter power, watts	Signal margin (Wallops), dB
in.	cm						
7.4 to 18.4	18.8 to 46.7	244.3	-8	2:1	1.6	8	37
17.4	44.2	9210	-3			1000 (peak)	20
47.4	120.3	30.8	-2	3:1	2.2	1	33
92.7 to 121.0	235.5 to 307.3	225.7	0	2:1	4	10	38
121.0	307.3	5600	1			400 (peak)	7

[a]Antenna gain is based on the gain of a standard dipole.

The 244.3-Mc antenna was a 0.5- by 12-inch (1.3- by 30.5-cm) alumina-filled slot which served as the delayed-time telemetry link. A typical radiation pattern is shown in figure 4(a).

The X-band (9210-Mc) system used four antennas spaced around the periphery of the vehicle, and the signal transmitted was a free-running beacon. The 30.8-Mc antenna used the front and aft parts of the test vehicle as a dipole. This system transmitted an unmodulated signal, and a typical radiation pattern is shown in figure 4(b).

The 225.7-Mc antenna was a coaxial horn antenna composed of structural members of the flare. This system served as the real-time telemetry system, and a typical radiation pattern is shown in figure 4(c). The C-band (5600-Mc) system was a rearward-looking radar beacon. This transponder signal was used for real-time tracking of the vehicle.

The differences in location and construction of the antennas have been noted. The differences in the bandwidth characteristics of the antennas should be emphasized since a plasma may have adverse effects on transmission by antenna detuning (ref. 35). The 244.3-Mc antenna was the most sharply tuned with $Q = 97$. The 30.8-Mc antenna was the most broadly tuned with $Q = 14$. The 225.7-Mc antenna was also broadly tuned with $Q = 25$.

Telemetry.- The onboard telemetry was an FM/FM system of 14 standard Inter-Range Instrumentation Group (IRIG) subcarrier frequency data channels which modulated two separated rf links to the ground receiving stations. The 225.7-Mc antenna (aft) relayed real-time data, while the 244.3-Mc antenna relayed data delayed 80 seconds by a continuous-loop tape recorder. Figure 5 is a block diagram of the telemetry system showing instrumentation, battery, and transmitter utilization. The information telemetered consists of the following: (1) RF system information including the VSWR and transmitter temperature of the 244.3-Mc, 225.7-Mc, X-band, and 30.8-Mc systems, and the VHF antenna impedances; (2) vehicle data, consisting of data from accelerometers, vibrometers, skin-temperature indicators, pressure sensors to determine vehicle angle of attack, and a sun scanner to determine roll rate and orientation (these data are discussed in ref. 31); and (3) water-injection-system data, consisting of the pressure in the water tank and at the injection nozzles, position of the rotary valve, and the time at which

water injection started. The water-injection system was monitored to determine whether or not the system was functioning correctly, and to determine the output flow rate of the system during flight. These data were provided by four sensors as follows: a thermistor bonded to the squib valve indicating when water injection started; a transducer measuring tank pressure; a cam-operated switch which referenced the position of the rotary valve in the programed water injection cycle; and a transducer on the largest side nozzle supply tube which redundantly referenced the position in the cycle and gave an indication of output pressure. These data were supplemented during prelaunch check-out by monitoring a thermocouple sensing tank temperature and a meter indicating external current supplied to the motor.

Range stations.- Locations of the receiving stations used during the flight are shown in figure 6. Receiving stations were located at Wallops Station, Virginia; Langley Station, Virginia; Coquina Beach, North Carolina; on a ship in the Atlantic Ocean 315 nautical miles (584 km) from the launch site on an azimuth of 124.4^O; and at Bermuda. A list of the receiving systems with pertinent characteristics is given in table I. The flight path and time history of the test vehicle during the primary data period (from 100 to 200 sec) are given in figure 6.

Water Injection System

The water injection system had to conform to the following design requirements: (1) a known range of flow rates was to be supplied separately at the stagnation and the side injection sites; (2) water was to be injected out of both sides simultaneously to minimize undesirable vehicle motions; and (3) during a given injection cycle, the flow rate was to be varied without appreciably affecting the penetration and atomization. This latter requirement could be satisfied by maintaining the pressure drop across the nozzles as nearly constant as possible. Therefore the flow rate was varied by changing the number of nozzles used during an injection cycle rather than by throttling the pressure in the supply tube. A schematic of the water injection system is shown in figure 7. The basic components are tank, squib valve, feed tubes, rotary valve and drive motor, cam switch, check valves, and injection nozzles. Some of these items will be discussed briefly.

Tank.- The water tank was an 11-inch (27.9-cm) inside-diameter aluminum sphere. The tank was loaded with 22 pounds (10.0 kg) of water, and the remaining volume was pressurized to 600 psi (4.14×10^6 N/m^2) with nitrogen gas. A flexible diaphragm separated the water and gas.

Squib valve.- The squib valve which initiated the experiment was located at the water exit of the tank. This squib valve allowed water to flow from the tank into two tubes which fed the motorized rotary valve.

Motorized rotary valve.- The motorized valve consisted of a hollow cylinder rotating inside a stationary valve body which was sealed watertight by close machining

tolerances. A pattern of ports was machined in the circumference of the rotor and valve body, and leads were connected from the valve body to the injection nozzles. Water was supplied from the tank to the inside of the rotor and released to the nozzles when the ports on the rotor coincided with the outlet ports on the sleeve. The rotor was driven by a 12-volt direct-current motor. A schematic layout of the rotor and sleeve is shown in figure 8. The ports were designed so that water was injected from the stagnation region through a known range of flow rates and shut off and then injected from the sides through a known range of flow rates and shut off. This cycle was repeated continuously, as the rotor was driven at a constant speed throughout the data period. The flow rate was increased linearly through seven levels for either stagnation injection or side injection by using three sets of outlet ports that supplied increasing numbers of orifices as indicated in figure 7. One port supplied a unit flow, the second supplied two units, and the third supplied four units. (The number of flow units was proportional to the number of nozzles supplied by the ports.) Combinations of flows from these three ports, therefore, will produce linearly increasing steps from one to seven units of flow, as illustrated in figure 8. The resulting idealized flow-rate variation with time for one cycle is shown in figure 8 for a constant pressure supply. As can be seen, each pulse consisted of increasing flow-rate levels and was of 2 seconds duration. The pulses were separated by a no-injection period of 1 second.

Injection nozzles.- The water was injected in the programed sequence just described from three injection sites: one at the stagnation (or nose) region, and two identical sites on opposite sides of the conical portion about 1.3 inches (3.3 cm) aft of the sphere-cone junction. A detailed layout of the injection sites and nozzles is given in figure 9. The injection site on the nose had six orifices arranged in a circular pattern and one orifice at the center for a total of seven orifices, all of which were 0.08 inch (0.2 cm) in diameter. The flow rate through each orifice gave one flow unit in this case. Each side injection site had 14 separate nozzles with 7 orifices of 0.015-inch (0.03-cm) diameter in each nozzle, giving a total of 98 orifices per side. In this case, a flow unit was obtained with 2 nozzles from each side for a total of 4 nozzles or 28 orifices.

TEST CONDITIONS

Launch and Trajectory

The RAM B2 vehicle was launched May 28, 1963, at 2:59:09 e.d.t. from the NASA Wallops Station. All systems operated as planned. First-stage burnout occurred at 38.4 seconds after launch at an altitude of 33 000 feet (10 km); second-stage burnout and third-stage ignition occurred simultaneously at 89.1 seconds at an altitude of 117 000 feet (35.7 km); third-stage burnout occurred at 118.5 seconds at an altitude of 160 000 feet (48.8 km) and a velocity of 17 840 ft/sec (5.438 km/sec). The third stage, which included

the payload, proceeded through the blackout region and reached an apogee of 290 000 feet (88.4 km). Altitude variation with velocity is shown in figure 10(a), and the variation of altitude and velocity with time is shown in figure 10(b). The data were taken during the ascending part of the flight in order to provide telemetry coverage close to the launch site. Real-time telemetry was transmitted from the 225.7-Mc telemetry system and an 80-second delayed-playback signal was transmitted from the 244.3-Mc telemetry system. Thus, in case of loss of signal due to blackout, the same telemetry information would have been obtained from the playback signal after the third stage had emerged from the blackout region.

Azimuth, Elevation, and Slant Range

The azimuth and elevation angles and the actual distance (slant range) to the vehicle from the five receiving stations are given in figure 11. These data are of use in interpreting signal-strength records to be presented in another section of the report.

The vehicle aspect angles (that is, the angle between the forward-directed longitudinal axis and the line of sight from the vehicle to the ground station) can be obtained from the approximate formula (since elevation angles are small according to fig. 11):

$$\text{Aspect angle} \approx \text{Azimuth angle} - \text{Vehicle heading} + 180^\circ$$

where vehicle heading is approximately the effective launch azimuth of 102°. (See ref. 31.) Hence

$$\text{Aspect angle} \approx \text{Azimuth angle} + 78^\circ \tag{1}$$

Water Flow Rates and Efflux Velocities

Figure 12 shows the variation of water flow rate with time that was obtained during the RAM B2 flight. The water addition was initiated 110 seconds after launch during third-stage burning and ended about 200 seconds after launch. The squib valve that turned on the water supply fired during a side injection period, so that the first pulse consisted of the last portion of a side injection sequence, as shown in the figure. Thereafter, each injection cycle, during which the flow was varied through a range of rates and was injected alternately from the stagnation nozzles and side nozzles, lasted about 6 seconds. The maximum flow rate per cycle varied throughout the data period from about 1.5 to 0.25 lbm/sec (0.114 to 0.681 kg/sec), and the minimum flow rate varied from about 0.3 to 0.07 lbm/sec (0.135 to 0.032 kg/sec) for stagnation injection, and from about 0.2 to 0.05 lbm/sec (0.09 to 0.023 kg/sec) for side injection. The flow rate at any point of a cycle is less than that at a comparable point on a previous cycle because of the decrease in tank pressure with exhaust of water.

The data shown in figure 12 were actually obtained from a calibration for which all pertinent flight conditions were duplicated as closely as possible. These conditions

included the supply tank pressure, exit pressure, rotary valve speed, and vehicle spin rate, all of which were monitored during the flight.

Seven distinct levels of flow are evident for each stagnation and side injection period up until the stagnation injection period at about 162 seconds, when only four levels can be distinguished. This same change in mass flow variation was observed during several calibrate runs and was believed to be caused by a partial closing of the tank outlet by the diaphragm when the tank was nearly empty. Since the change occurred near the end of the injection period and appeared to be reasonably predictable, no modifications to the injection system were made and it was assumed that the observed variation also occurred in flight. The integral of the flow-rate curve of figure 12 is 21.5 pounds (9.8 kg), which compares favorably with the total of 22 pounds (10.0 kg) of water initially loaded in the tank.

In order to obtain estimates of the ratio W^* of water mass flow to air mass flow in the mixing region, the maximum penetration of the water spray must be determined. In reference 18, the maximum penetration of a liquid spray for cross-current injection was correlated in terms of the free-stream density and velocity and the efflux velocity and density of the liquid. The variation of efflux velocities with time is shown in figure 13. These velocites were computed for the maximum and minimum mass flow rates by using the data from figure 12 and the corresponding total exit area of the orifices. That is, for side injection (fig. 13(a)) with the maximum flow rate, all 28 nozzle stations on both sides were in operation for a total of 196 orifices. For side injection with the miminum flow rate, 4 nozzle stations or 28 orifices were in operation. For stagnation injection (fig. 13(b)), the maximum flow rate was obtained with 7 nozzles and the minimum rate with 1 nozzle. The velocities are larger for the smaller flow rates because of the smaller losses in the system. An estimate of the total losses in the system can be obtained by comparing the maximum and minimum flow-rate velocity results with the velocity computed directly using the measured tank pressure with the assumption of no losses. The results of this latter computation are also plotted in figure 13.

RESULTS

Signal-Strength Records

Variations in signal strength with time for the HF, VHF, C-band, and X-band transmissions were recorded at the Wallops Station, Langley Station, Coquina Beach, Range Recoverer, and Bermuda receiving stations. The signal strength is obtained from the voltage level of the automatic gain control (AGC) of the receiver. All signal-strength data in this report are given as the relative signal strength in decibels, that is

$$\text{Decibel} = 20 \log_{10} \frac{E}{E_{ref}}$$

where E is the AGC voltage. The reference signal strength for zero dB is chosen as the peak signal level obtained at a given receiver during the flight.

Portions of typical oscillograph records obtained at the Wallops and Coquina Beach stations during the water injection period are shown in figure 14. The effect of water injection for two injection cycles (approximately 12 seconds) is shown. Significant signal recovery occurred during the water injection periods which are indicated on the figure. The 3-cycle-per-second variation, which was caused by antenna pattern change with vehicle roll (see fig. 4), can be seen on the records during the periods of signal recovery. This roll effect is particularly noticeable on the 244.3-Mc signal which was transmitted by the forward slot antenna. A low-frequency oscillation of approximately 30 cps occurred during the stagnation injection pulses. This oscillation is typical of all signal-strength records obtained during stagnation injection.

Signal-strength measurements from the five receiving stations for the entire data period (80 to 180 seconds after launch) for frequencies of 244.3 Mc, 30.8 Mc, and 225.7 Mc are given in figures 15 to 19. The variations in signal strength can be conveniently correlated with the water injection pulses from the side or stagnation region by means of the water injection key superimposed at the top of the figures. The variations of signal strength due to vehicle roll and the low-frequency oscillations during stagnation injection as shown in figure 14 have been removed for clarity in figures 15 to 19 by fairing through the peak values of recorded signals. Parts (a), (b), and (c) of these figures present the data according to increasing downstream distance from the injection site. These data are from the 244.3-Mc, 30.8-Mc, and 225.7-Mc antennas, respectively, which will be referred to as the forward slot, middle ring, and rear flare antennas (fig. 2). Since each figure shows data for a particular receiving station, a different look angle and range applies to each figure at a given point in time. These look angles and the slant range can be obtained from the data of figure 11.

Several receivers, as listed in table I, were used for the same signal frequency at a number of the stations. Wide- and narrow-bandwidth receivers and different receiving antenna configurations were used. Wide-bandwidth (200-kc) receivers were required to handle telemetry data, but narrow-bandwidth (16-kc on 244.3-Mc and 8-kc on 30.8-Mc) receivers were also used to monitor signal strength since they provide more gain and hence more margin. The receivers from which the data of figures 15 to 19 were obtained are identified in table I. At a given station and frequency, these signal-strength data are essentially the same; therefore, in all the figures, only one typical record for each frequency has been shown.

Typical signal-strength records of C-band and X-band frequencies, as received at the Wallops and Coquina Beach receiving stations, respectively, are shown in figures 20 and 21. These results will be discussed in more detail in a subsequent section, but it is believed that no significant attenuation of the C-band and X-band signals due to the plasma occurred.

Voltage Standing-Wave Ratios (VSWR)

VSWR measurements made on board the vehicle were transmitted in real time from the 225.7-Mc system and on an 80-second delayed-playback signal from the 244.3-Mc system. The VSWR values provide an indication of any antenna detuning that might be attributed to the plasma sheath (ref. 35); therefore, VSWR records are an important aid in interpreting the data. VSWR records for the 244.3-Mc and 30.8-Mc antennas are shown in figure 22. The 225.7-Mc measurement of VSWR showed no change in level during the flight, and is not presented. During water injection periods for both stagnation and side injection, the VSWR values for the forward slot antenna (fig. 22(b)) return to approximately their free space values, an indication that no detuning effects are present for this antenna during water injection. The VSWR values for the middle antenna (fig. 22(a)) return to free space values during stagnation injection, but during side injection the VSWR values are somewhat greater than free space values, an indication that a slight amount of detuning occurs in this case. VSWR measurements during water-off periods will be discussed later.

DISCUSSION OF ATTENUATION RESULTS
DURING WATER-OFF PERIODS

Signal Strength

The signal-strength records at the Wallops and Langley receiving stations (figs. 15 and 16) indicate that attenuation began at about 90 seconds from launch, just after third-stage ignition. At the Coquina and Range Recoverer stations (figs. 17 and 18), however, no attenuation was observed until about 100 seconds from launch. Since the former two stations have a more rearward aspect angle as compared with the latter two stations (fig. 11 and eq. (1)), the earlier onset of attenuation at the former stations was evidently caused by the rocket exhaust. The relatively rapid increase in attenuation of the signal from the rear antenna (figs. 15(c) and 16(c)), which must transmit through the rocket exhaust to these stations, is a further indication of this effect. This well-known phenomenon of attenuation due to rocket exhaust has been observed and analyzed previously (refs. 24 and 36). It is apparent that attenuation due to the plasma layer on the vehicle did not commence until about 100 seconds from launch (fig. 17) and from then until

third-stage burnout (118.5 seconds) the attenuation observed at the Wallops and Langley receiving stations would be due to a combination of rocket exhaust and plasma effects.

The data from the Coquina station (fig. 17) would thus best represent the effects of the plasma layer alone, up to 118.5 seconds. As the vehicle approached its maximum velocity of 17 840 ft/sec (5.438 km/sec) (at third-stage burnout), the 30.8-Mc and 225.7-Mc signals (figs. 17(b) and (c)) were attenuated by approximately 20 and 22 dB, respectively, during the no-injection periods. The 244.3-Mc signal (fig. 17(a)) dropped below the receiver system noise level and was therefore attenuated at least 32 dB. During the water-off periods, the observed signals remained below noise levels until approximately 160 seconds (230 000 ft (70.1 km) of altitude), when signal levels began approaching free space values. Free space values were attained at about 170 seconds on the forward and middle antenna signals but were down about 10 dB from values before onset of attenuation because of the increased distance between the Coquina station and the vehicle.

The minimum observed values of relative signal strength after third-stage burnout for no injection are listed in the following table:

Signal frequency, Mc	Relative signal strength in decibels				
	Wallops (fig. 15)	Langley (fig. 16)	Coquina (fig. 17)	Range Recoverer (fig. 18)	Bermuda (fig. 19)
244.3	<-48	<-38	<-36	<-33	<-22
30.8	-31	-25	-22		
225.7	-32	-32	-32	-31	-17

The values listed in the table include the decrease in the free space signal levels as well as the attenuation of the signal due to the plasma. If it is assumed that stagnation injection returns the signal level to free space values (this assumption will be justified later), then the approximate value of attenuation caused by the plasma alone can be determined. The maximum values of plasma attenuation determined in this manner are listed in the following table:

Signal frequency, Mc	Values of plasma attenuation in decibels				
	Wallops (fig. 15)	Langley (fig. 16)	Coquina (fig. 17)	Range Recoverer (fig. 18)	Bermuda (fig. 19)
244.3	>35	>27	>32	>25	>20
30.8	25	15	20		
225.7	22	20	22	23	15

The 30.8-Mc signal was not blacked out and was attenuated much less than the VHF signal from the forward antenna. This difference in attenuation between the HF and forward VHF signals is due in part to the more favorable location of the HF antenna and the differences in design and bandwidth characteristics of the antennas. (See sections entitled "Apparatus and Voltage Standing-Wave Ratios.")

The C-band signal at 5600 Mc (fig. 20) and the X-band signal at 9210 Mc (fig. 21) were not attenuated to any large extent by the plasma layer at any time throughout the flight. The sudden increase in the C-band signal at about 89 seconds from launch is due to the exposure of the C-band antenna (located in the test vehicle flare, fig. 2) when the test vehicle is separated from the second-stage booster. The reason for the increase in the signal at about 98 seconds from launch is not known. The slight decreases in the level for both C-band and X-band signals from about 114 seconds through the remainder of the data period are due to increasing range. The X-band signal-strength record toward the end of the data period is also influenced strongly by antenna pattern.

VSWR Values

Some of the signal loss observed during periods of no injection can be attributed to antenna detuning, as indicated by the increases in VSWR values for the forward and middle antennas (fig. 22). A maximum VSWR value of 6.5 was recorded for the middle antenna (fig. 22(a)) and the VSWR for the rear antenna showed no variation during the entire flight. Hence, no plot for this rear antenna is shown.

The VSWR for the forward antenna (fig. 22(b)) increased to a value of at least 10, which is beyond the accurate range of the instrument. During the period from launch to the beginning of attenuation, the VSWR for this antenna increased from about 1.5 to 3.0. The reason for this gradual increase is not known, although an increase in temperature could be a factor. After 110 seconds, the VSWR for the forward antenna could not be accurately determined, but it is believed that signal losses due to detuning effects were not large compared with total signal losses. This belief is based on the results of ground tests reported in reference 35 and unpublished results obtained at the Langley Research Center of an experiment on the RAM B3 flight where the effects of detuning on narrow- and broad-bandwidth antennas were compared.

ANALYSIS AND DISCUSSION OF RESULTS FOR WATER INJECTION

The signal-strength data presented have shown that both stagnation and side injection are effective. Also, for the flight conditions of the present investigation, the results indicate that stagnation injection causes greater signal recovery.

19

In the following sections, some of the mechanisms that may contribute to electron depletion or suppression are analysed for the RAM B2 flight conditions. Details of the analyses used are given in the appendixes, with only the principal results presented in the text. The mechanisms for stagnation and side injection are discussed separately.

For stagnation injection, the mechanisms considered are aerodynamic shaping and homogeneous cooling. Both these mechanisms would suppress the electron formation processes which normally occur in the stagnation region. The flight results are examined to determine, if possible, the range of conditions over which these mechanisms may have been effective.

Greater signal recovery during stagnation injection could have been caused by the same mechanisms (operating at greater efficiency) as those involved in side injection. It is also possible that mechanisms not applicable to side injection cause the improved performance of stagnation injection. Since nearly complete signal recovery was obtained for side injection and since the water injected during stagnation injection is eventually swept past the side injection sites, the effectiveness of the additional stagnation mechanisms cannot be directly deduced from these test results. For instance, if the additional stagnation mechanisms were not at all effective, the greater signal recovery observed during stagnation injection could still occur due to longer dwell times of the injectant, more effective distribution in the flow field, or a more optimum water droplet size. On the other hand, if a stagnation mechanism were completely effective, it would also explain the observed greater signal recovery during stagnation injection.

For side injection, electron concentrations can be reduced by homogeneous processes (that is, reactions that occur between the gaseous constituents of the flow), or by heterogeneous processes, which are those reactions that occur in the vicinity of or at interfaces such as the water droplet surfaces. The free electrons are produced in the stagnation region and are generally present in the afterbody flow in higher concentrations than would be predicted on the basis of equilibrium ion-electron recombination. The injection of relatively large amounts of liquid water could tend to catalyze both ionic and neutral reactions so that plasma conditions after water injection would approach equilibrium more rapidly.

In the following analysis of homogeneous cooling, the ionic and neutral species are assumed to be in equilibrium, and the effects of both complete evaporation and finite evaporation rates of the injected water are considered. It is emphasized, however, that the assumption of thermodynamic and chemical equilibrium can only be correct as a limiting condition when gas flow time (i.e., the time for a reference volume of gas to flow from the bow shock region to the location being considered) is large compared with recombination time. For conditions of the present flight, it is known that nonequilibrium conditions prevail during water-off periods. During water injection, the homogeneous reaction rates should increase significantly, while at the same time, gas flow times should

20

increase because of momentum exchange between the gas and the liquid spray. At present, however, the chemistry of the system is not well understood when liquid water is present. Hence, it is necessary to resort to simplifying assumptions with the hope that gross changes in flow conditions and electron concentrations can be described.

After the homogeneous cooling processes are considered, it is convenient to analyze the mechanism of heterogeneous recombination separately. The results are then compared with predictions of references 16 and 17. Finally, the flight results are compared with predictions of the various analyses in an attempt to determine which effects predominate.

It should be noted that in the analyses, it is necessary to determine or assume the electron density before and after injection. The initial electron density is determined by calculation and from measurements made in a similar flight test. (See ref. 32.) The electron density after injection is estimated from the transmitted signal levels; high attenuation indicates the plasma electron density exceeds critical density, and low attenuation indicates the electron density is less than critical. This method of estimating electron density after injection is satisfactory provided that ν/ω $\left(\dfrac{\nu}{\omega} = \dfrac{\text{Plasma collision frequency}}{2\pi \text{ transmission frequency}}\right)$ is small and that the dominant influence on the signal is the plasma in the near vicinity of the antenna. For the forward slot antenna, since the radiated energy is localized in the vicinity of the slot, and the plasma is essentially adjacent to the antenna, signal strength measurements can be used to estimate plasma electron concentrations. However, the rearward 225.7-Mc antenna is not as suitable for this purpose since most of the energy from this antenna was directed into the wake rather than into the plasma sheath. The 30.8-Mc signal-strength measurements are not descriptive of the local plasma sheath since for this antenna, energy is radiated from the entire spacecraft. Also, for this latter frequency, the critical electron concentration (which is 10^7) does not define a sharp signal attenuation since ν/ω is about 1. For these reasons, the signal strength measurements obtained for the forward slot antenna (for which the critical N_e is 10^9 electrons per cm^3) provide the most reliable indication of local N_e levels in the flow field over the conical portion of the vehicle.

Stagnation Injection

Aerodynamic shaping.- When material is injected into the stagnation region of a supersonic vehicle, the bow shock standoff distance and shape may be considerably modified. For example, the effect of gas injection on the shock standoff distance for a blunt-nose cone is shown in reference 37 to depend mainly on the ratio of the injected mass flow to the airstream mass flow. In this instance, the gas was injected from a spherically shaped porous segment that formed the nose of the model. The shock shape described in reference 37 was not affected much by injection, probably because of the small momentum of the injected gas.

In reference 18, tests conducted in a wind tunnel at Mach 8 with liquid injection at the stagnation point of a hemisphere cylinder are reported. In these tests the material used was liquid nitrogen, which was injected from a single orifice to obtain large momentum of the injected material. The maximum shock standoff distance was correlated in the form

$$\frac{\delta_x}{d} = 2.16(T^*)^{0.43} \tag{2}$$

where T^* is the ratio of the momentum of the injected liquid to the momentum of the free stream contained in a stream tube with the same diameter as the model nose. The results of reference 18 indicated that when $T^* > 0.05$ the bow shock was unsteady and oscillated at high frequencies between a pointed configuration and a blunted or broken-front configuration. When $T^* \approx 0.01$ the magnitude of the oscillations was much smaller but the shock still assumed a pointed shape.

Recent wind-tunnel test data (unpublished) obtained at the Langley Research Center indicate that the shock standoff distance (and forward penetration of the liquid jet) for water injection would be greater than that predicted by equation (2) for liquid nitrogen injection because of the smaller vapor pressure of water. These data, as well as those of reference 18, were obtained with models of nose diameter less than 1.8 inches (4.6 cm) and generally with a single orifice. Therefore, only tentative conclusions can be obtained by extrapolating the correlations to the RAM B2 vehicle, which had a nose diameter of 8 inches (20.3 cm) and used from one to seven orifices for stagnation injection.

The variation of the momentum ratio parameter with time during the RAM B2 flight is shown in figure 23(a) for the maximum and minimum stagnation injection rates. During the data period (except during the minimum injection rates) the momentum ratio was greater than 0.01. Hence, the results of reference 18 and the previous discussion indicate that during most of the injection period the bow shock might be oscillating between the pointed configuration and the collapsed configuration, as in the tunnel tests. During the time when the shock assumed a pointed shape, the production of free electrons normally occurring behind the bow shock would essentially cease. Since the normal-shock regions are the source of the electrons in the flow field for the RAM flight conditions, as indicated in reference 6, recovery of radio transmission due to the effect of bow shock modification would be expected for stagnation injection. This effect is analogous to that produced by aerodynamic shaping, or the use of a pointed or slightly blunted cone to reduce the temperature and the amount of shock-heated air.

Stagnation cooling.- Signal recovery due to shock modification could occur simultaneously with other effects of material addition such as cooling or attachment and heterogeneous mechanisms. Therefore, it may not be generally possible to ascribe observed transmission changes to any one mechanism. In figure 23(b), the ratio of injected flow

rate to the reference free-stream airflow rate is plotted as a function of time for the RAM B2 flight. The fact that this mass-flow ratio is as large as 15 indicates that some cooling or quenching effects would be expected during stagnation injection, particularly in the stagnation region where flow-field densities and species "dwell times" are large.

An analysis of the cooling effect of stagnation injection is included in appendix A. The assumptions of complete evaporation and complete thermal equilibrium were used in this analysis, and the results indicate that the flight values of injected flow rate would have been sufficient to give complete signal recovery. These assumptions, however, may not be valid for the range of conditions of the present flight test.

Observed signal recovery during third-stage burning period.- For convenience, the test data for stagnation injection are discussed in two parts Some of the data was affected by third-stage burning, and these data will be considered first.

As mentioned previously, the data from the Coquina Beach station (fig. 17) should be free of rocket exhaust effects during third-stage burning because of the aspect angle, which varied from about 105° to 127° for this station (fig. 11 and eq. (1)). The first injection pulse from the stagnation nozzles at 112.4 seconds resulted in complete recovery of the signal at Coquina Beach (fig. 17) from all three antennas. The minimum flow rate was 0.3 lbm/sec (0.136 kg/sec) (fig. 12) and the corresponding ratio of coolant mass flow rate to reference air mass flow rate was 0.58 (fig. 23(b)). The computed shock layer thicknesses of reference 38 indicate that the flow rate of air contained within the undisturbed shock layer near the forward antenna station at this time would be about 4.5 lbm/sec (2.040 kg/sec); therefore, the value of W^* is approximately 0.07 if the injectant is assumed to be confined to the shock layer. The minimum momentum ratio parameter at this time was about 0.006 (fig. 23(a)), a value which, according to data of reference 18, would be too small to cause any large modifications to the bow shock. The results of reference 18 indicate that the cause of signal recovery for minimum stagnation injection rates at this time would be a cooling (or quenching) effect that would presumably take place mostly in the stagnation region. However, according to the previously discussed unpublished data for stagnation injection (see subsection under "Stagnation Injection" entitled "Aerodynamic shaping") the bow shock modifications and forward penetration of the liquid jet would be large even for the minimum value of the momentum parameter, and the principal mechanism might well be aerodynamic shaping. The question regarding the magnitude of the bow shock disturbances and forward penetration for these conditions is at present unresolved.

An effect of interest that was noted during third-stage burning is that no recovery was obtained (during both stagnation and side injection) for the signal from the rear antenna at the Wallops or Langley stations. Thus, figures 15(c) and 16(c) show no signal recovery until after third-stage burnout, which was at 118.5 seconds. Because of the aspect angles of the Wallops and Langley stations (180° and 158°, respectively, at

118.5 seconds; see eq. (1) and fig. 11) and the rear antenna location, transmission in this case was largely through the rocket exhaust plume. It is therefore evident that water injection from either the stagnation or side nozzles had little effect on electron concentrations associated with the rocket plume.

The fact that only partial recovery of signal from the forward antenna at the Wallops station (fig. 15(a)) occurred for the first two water pulses is also probably due to rocket exhaust interference. However, the partial recovery at the Range Recoverer station (fig. 18) at the forward and rear antennas for the first two or three pulses is probably due to the forward aspect angle (approximately 30°; see eq. (1) and fig. 11) of this station during this time period and the associated azimuth (or yaw plane) antenna patterns (figs. 4(a) and 4(c)).

Observed signal recovery after third-stage burning.- Practically complete recovery was noted for the HF and VHF signals during stagnation injection at all stations except Bermuda (fig. 19), which was not in range until 128 seconds from launch. In most cases even the smallest flow rate, which was obtained by injection from the single orifice at the stagnation point, gave essentially complete recovery throughout the data period up to the time of about 163 seconds. At this time the minimum flow rate is 0.1 lbm/sec (0.045 kg/sec) (fig. 12), and the corresponding value of W^* near the forward antenna station is approximately 0.4 if the injectant is confined to the undisturbed shock layer. Inasmuch as the momentum parameter for this case is nearly 0.01 (fig. 23(a)), the results of reference 18 indicate that the bow shock was probably modified to a pointed configuration. Preliminary correlations of the unpublished stagnation injection data (referred to previously) would also indicate that the bow shock at this time would be pointed, as a result of the large forward penetration of the injected water. For a pointed shock configuration, the electron production is much less than for an undisturbed bow shock configuration. The tests of reference 18 showed that the pointed shock configuration was unstable and tended to collapse and re-form at a high frequency. This phenomenon would explain the oscillations in signal strength during stagnation injection, as shown in figure 14. These oscillations were observed for stagnation injection during the entire data period, and they indicate the presence of an unsteady flow effect which must have been due to the bow shock oscillations. The magnitude of the oscillations noted in the signal-strength records (fig. 14) is not large compared with the total signal-strength recovery level; consequently, it is believed that homogeneous cooling and heterogeneous mechanisms may have accounted for part of the signal recovery, particularly during the time when the bow shock was in a collapsed position. These mechanisms are considered for the side injection case in a later section. No attempt has been made to compute the effect of these mechanisms for stagnation injection (other than the simplified analysis of appendix A) since the characteristics of the flow field during stagnation injection are not known. However, wind-tunnel tests in which droplet evaporation distances were scaled

24

(ref. 18) showed that liquid injected at the stagnation point existed as droplets far down-stream of the injection site. The heterogeneous and cooling mechanisms should be more effective for stagnation injection than for side injection, since the gas species and liquid droplet dwell times would be greater. It is therefore concluded that heterogeneous and cooling mechanisms could be important in explaining the recovery due to stagnation injection.

The reason for the loss of signal at the Range Recoverer station during stagnation injection from 155 to 157 seconds (fig. 18) is not known. Some reduction in effective-ness of stagnation injection near these times is also noted on some of the other records (figs. 15(a), 15(c), and 17(a)). It is possible that the vehicle oscillatory motions, which by this time had probably built up to an angle of attack of nearly 10° (ref. 31), are respon-sible for the reduced effectiveness of stagnation injection at this time.

<center>Side Injection</center>

Water spray distribution and estimates of water-to-air mass flow ratio.- In order to apply the various theories that will be discussed in the following sections, an estimate of the concentration of injected water at any station is required. In the one-dimensional treatments to be used, this concentration is assumed to be uniform at any given stream-wise station and is expressed as the ratio of the flow rate of injected liquid to the flow rate of air within the region occupied by the spray at that station. The area occupied by the spray is based partly on the maximum cross-current penetration of the spray.

Maximum spray penetration: Correlation formulas for the maximum spray pene-tration on a RAM B model are given in reference 18. These formulas are

$$\frac{y_{max}}{d_o} = 1.79\left[\overline{V}\left(\frac{p_v}{p_a}\right)^{-0.24}\right]^{0.25}\left(\frac{x}{d_o}\right)^{0.5} \tag{3}$$

for water injection with $1 < \frac{p_v}{p_a} < 10$ and

$$\frac{y_{max}}{d_o} = 0.89\overline{V}^{-0.3}\left(\frac{x}{d_o}\right)^{0.5} \tag{4}$$

for liquid nitrogen injection with $90 < \frac{p_v}{p_a} < 700$. It should be noted again that the tests of reference 18 were conducted on small-scale models with a single orifice; therefore, extrapolation of the results to the RAM B2 flight conditions is considered tentative.

The spray penetration predicted by these formulas for the RAM B2 flight conditions is plotted as a function of time from launch in figure 24 for values of x of 20, 60, and 120 inches (50.8, 152.4, and 304.8 cm), which correspond approximately to the locations of the 244.3-Mc, the 30.8-Mc, and the 255.7-Mc antennas, respectively. The actual

efflux velocities in figure 13(a) were used in these calculations. The formula for liquid nitrogen is applied only at the last three trajectory points where $\frac{p_v}{p_a} > 10$. (It was assumed that $p_v = 0.025$ atmosphere, corresponding to the vapor pressure of water at 70° F (272° K). The variation of p_a is given in appendix A.) The shock layer thickness δ_Y (that is, the distance between the vehicle surface and the undisturbed shock) was estimated as 5, 9, and 14 inches (12.7, 22.9, and 35.6 cm) for the forward, middle, and rear antenna stations. These estimates are based on the shock shapes for sphere-cones given in reference 39. Comparison of the predicted spray penetration (in terms of the distance out from the surface Δy_{max}) with these estimated shock layer thicknesses indicates that up to the time of 150 seconds the penetration was about the same or somewhat less than the undisturbed shock layer thickness. For times greater than 150 seconds, the predicted penetration became greater than the undisturbed shock layer thickness and increased to almost twice as large at the end of the data period (about 180 seconds). If the spray penetration was actually larger than the shock layer thickness, induced secondary shocks could exist, and also the spray would not be utilized efficiently as a coolant. (See ref. 18.)

Calculation of W^* for forward antenna location: Since, as shown in figure 24, the water spray penetrated to approximately the location of the undisturbed shock, the amount of air in the mixing region is essentially the quantity of free-stream flow contained in a stream tube which has a radius determined by the maximum penetration distance. A reasonable estimate of W^* that would represent a mean value in the region of the spray would then be given by the formula

$$W^* = \frac{\frac{1}{2}(\dot{m}_c)_t}{\pi\left(r_B + \Delta y_{max}\right)^2 \rho_\infty V_\infty f_i} \tag{5}$$

where r_B is the body radius, Δy_{max} is the maximum spray penetration from the body surface, f_i is the fraction of the total 360° around the body that is occupied by the spray from one side, and $(\dot{m}_c)_t$ is the side injection mass flow rate for both sides of the vehicle as obtained from figure 12. Maximum and minimum values of $\frac{1}{2}(\dot{m}_c)_t$ were obtained from the data of figure 12 for side injection. The corresponding values of W^* computed from equation (5) for $x = 20$ inches (50.8 cm) (corresponding to the forward antenna station) are plotted as a function of time in figure 25. The assumed values of f_i shown in this figure are based on observations in reference 18 that the spray, even from a single orifice, may spread at least halfway around the body when p_v/p_a is large, corresponding, in this case, to the higher altitudes. (See also the temperature-time data of figs. 15(c) and 20(e) in ref. 40.) During the first part of the injection period when the altitude was less than 160 000 feet (48.8 km), the water spray would not be expected to spread very far in the lateral direction from the injection nozzles. The change in lateral extent of the spray with altitude is caused by the change in the ratio of liquid vapor pressure to

flow-field pressure p_v/p_a near the injection site. When this ratio is much greater than one, the liquid jet explodes, in effect, when it enters the flow field, and droplets are thrown far to either side of the nozzle. When this pressure ratio is about one, or less than one, the liquid jet penetrates farther into the flow field and is atomized only by pressure and shear forces of the airstream.

The preceding discussion and the results of figure 25 indicate that, for applying the theory to the RAM B2 flight conditions, values of W^* between 0.5 and 1.0 are representative of conditions for the maximum injection rates and values of W^* between 0.1 and 0.3 are representative of conditions for the minimum injection rates. These values of W^* are applicable at the forward antenna station at $x = 20$ inches (50.8 cm). Forward of this station the values of W^* would be greater because of the smaller area occupied by the spray and the resultant smaller amount of air in the mixing region. That is, the liquid spray tends to spread out and move farther away from the body (because of its initial outward momentum) as it is swept downstream. For RAM B2 flight conditions, estimates of values of W^* at $x = 5$ inches (12.7 cm) were computed in reference 40 by using the same method as that used herein; for the minimum injection rates, values of W^* from 0.2 to 0.75 were obtained. Hence, a mean value of W^* corresponding to minimum injection rates for the mixing region upstream of the forward antenna station would be about 0.5; this value will be used in the evaporation calculations.

Effect of W^* on observed signal recovery level.- In a first attempt to analyze the effect of water injection on signal strength, the recovery signal level for the seven steps of increasing water flow rate (see fig. 12) during several side injection pulses was read from the original signal-strength records for typical receivers at the Coquina and Wallops stations (fig. 14). The differences between these recovery signal levels and the corresponding reference free space levels (the differences are hereinafter referred to as adjusted recovery signal levels) are plotted as functions of W^* in figure 26. The values used for W^* were obtained by extrapolation from figure 25, and hence, they represent conditions near the forward antenna station.

The procedures used to obtain the pertinent free space signal levels and the values of W^* are discussed in the following paragraphs. (Typical free space signal levels and the corresponding water flow rates are shown for the second and third side injection pulses in figure 14(b). The resulting adjusted recovery signal levels for the 244.3-Mc antenna and other data for the second and third pulses are given in table II.)

Free space signal levels were first computed by correcting the initial free space level before the onset of attenuation (obtained directly from signal-strength records at about 88 seconds) for the changes in range and antenna pattern during the data period. These computed free space signal levels were found to be in reasonable agreement with the observed signal recovery levels during stagnation injection. Hence, a line drawn through the peaks in signal level for stagnation injection, as illustrated in figure 14(b),

was used as the reference free space level. The maximum signal level during each step of the water flow was then read. The corresponding value of W^* was obtained by multiplying the maximum value of W^* from figure 25, at the time considered, by the ratio of the observed values of flow rate to the maximum flow rate for the particular side pulse being considered. The adjusted signal recovery levels, obtained by subtracting these maximum levels at each flow rate from the reference free space levels, are plotted as functions of the corresponding values of W^* in figure 26. Data from the first side injection pulse are not used since this cycle was incomplete and the transient flow rates could not be accurately determined. Data beyond the ninth side injection cycle are not included since subsequent signal recovery pulses were poorly defined.

While there is considerable scatter in the data, it is seen that reasonable correlation was obtained. The scatter is probably partly caused by variations in antenna pattern (fig. 4), which could cause rapid variations in free space signal level not accounted for in the procedures used. Nevertheless, two important conclusions can be made from these plots: (1) Increasing W^* above approximately 0.3 caused no significant increase in signal level; and (2) The minimum value of W^* of about 0.1 (corresponding to the first step in water injection flow rate) resulted in signal recovery levels that were approximately 2 to 10 dB below the maximum recovery levels, but were still well above receiver noise levels in all cases. Hence, the minimum injection flow rates represent essentially minimum requirements to obtain usable signal recovery for the test conditions.

Another trend that is evident in the data from the forward slot antenna (figs. 26(a) and (d)) is the reduction in adjusted signal recovery level with increasing altitude (excluding data for the ninth pulse). This trend, which is particularly noticeable for values of W^* greater than about 0.5, indicates that the efficiency of side injection decreases with altitude. The deviation of the data for the ninth side pulse from this trend is believed to be caused by increases in vehicle angle of attack (see ref. 31) which reduced the signal recovery level for stagnation injection and thereby introduced an erroneous value of reference free space signal level in the procedure used to obtain the data of figure 26.

It is emphasized that the values of W^* used in figure 26 are for conditions near the forward slot antenna and that values of W^* upstream of this antenna are believed to be larger, as discussed in the previous section. Also, for the first four steps of increasing flow rate, the lateral extent of the spray around the vehicle would tend to increase as W^* increases because of the physical arrangement of the injection orifices and their use in the injection sequence. (See figs. 7, 8, and 9.) In figure 14(b), clearly defined steps of increasing signal strength corresponding to steps of increasing flow rate can be seen on the 30.8-Mc record. It is therefore possible that for this middle ring antenna, the observed steps in signal strength are associated with the increase in lateral extent of the spray rather than with increases in W^*. In general, however, the increase

in flow rate rather than the increase in lateral extent of the spray is believed to be the main cause of the increased signal recovery observed after the initial recovery for each pulse. Two references support this belief: first, the attenuation tests of reference 7 show that water injection from a single orifice on one side of a model (approximately 1/4-scale model of the RAM B2) gave recovery of VHF with a signal-strength pattern essentially the same as that for free space; and second, the wind-tunnel tests of reference 18 indicate that the effects of liquid injection from a single orifice extended halfway around the model downstream of the injection orifice. It is therefore concluded that the minimum flow rates used during the RAM B2 flight experiment correspond directly to minimum amounts required to give the partial signal recovery observed at the beginning of the side injection pulses. Nevertheless, for these and other reasons it is obvious that the correlations of figure 26 are not general and should not be applied indiscriminately to other configurations or flight conditions. In order to generalize the present results with any success it is necessary to analyze the local flow conditions in the spray region in some detail and to consider the effect of various assumed mechanisms on electron levels. Also, as pointed out previously, the signal strength results from the forward slot antenna are the only data that are suitable for obtaining reliable estimates of the local N_e levels after water injection.

Theory for homogeneous cooling.- The results of references 11 and 17 tend to indicate that homogeneous cooling mechanisms were probably not of much significance for the RAM B2 conditions. Nevertheless, it is considered worthwhile to present the theory for homogeneous cooling with the assumptions of ionic and thermodynamic equilibrium because the experimental results appear to be in partial agreement with predictions from such an analysis. Also, equilibrium conditions represent a limiting state that could be attained for long species dwell times and fast reaction mechanisms. The processes required to reach this final equilibrium state would involve both heterogeneous and homogeneous mechanisms. If the homogeneous cooling effects of the added material contribute to electron suppression through the mechanisms of increased ionic recombination and atomic or molecular attachment rates, it seems advantageous to inject a liquid rather than a gas. Some of these advantages are illustrated in figure 27 which shows a comparison of the general appearance of gas injection with liquid injection. The bow shock configuration is scaled from actual wind-tunnel tests with injection from a single orifice just aft of a hemispherical nose, as indicated. The gas injection results are based on some unpublished data obtained in the Langley 11-inch hypersonic tunnel and the liquid injection results are based on the data of reference 18. The ratio of injected mass flow to reference air mass flow $\dot{m}_c/\dot{m}_{ref}$ was about 1.5 in both instances. The first thing to be noted is the larger initial disturbance with gas injection, with the possible additional ionization caused by the secondary or induced shock. The hot ionized gases generated by this secondary shock, as well as by the bow shock at the nose, are forced away from the

vehicle surface and cooled in the subsequent mixing region which may extend far downstream. In contrast, the liquid injection produces a smaller initial disturbance because of the smaller added volume. The liquid jet is rapidly atomized by the high-velocity airstream into a spray of fine droplets which are more or less uniformly distributed across the shock layer. The effective "mixing length" is then determined by the distance required to evaporate the droplets since the added material will be uniformly mixed with the airstream about as rapidly as it evaporates.

Other advantages associated with liquid injection are the larger heat-sink capability due to the latent heat, the better control of initial penetration and distribution in the flow field, and the ease in handling and storage. The investigation of reference 18 indicates that a liquid spray can be properly located in the flow field and that evaporation occurs rapidly for low-altitude conditions. Thus, except at high altitudes where evaporation rates are small and nonequilibrium effects predominate, some homogeneous cooling should be possible, although the resulting effect on electron concentration depends entirely on the relative values of recombination times and species dwell (or flow) times.

Complete evaporation: Estimates of the amount of injected material required to cool the flow field can be obtained by assuming equilibrium conditions and by using the conservation equations for mass, momentum, and energy (see appendix A for details). A specified fraction of the air contained in an intercepted stream tube of radius r_i is assumed to be cooled in the mixing region. Downstream of the mixing region at some station denoted by the subscript 2, the coolant is assumed to be completely evaporated and uniformly mixed across the portion of the shock layer that extends out to the streamline which would pass through the r_i shock point. That is, it is assumed that the coolant can be made to penetrate just out to this particular streamline and no farther. (This streamline would be displaced outward from its location with no injection.) Chemical and thermodynamic equilibrium are assumed at station 2, and only the "average" flow properties are considered since there is no way to compute the actual variation in local flow conditions across the layer of mixed water vapor and air. The thermodynamic properties of the mixture were obtained as functions of temperature for given values of p_2 and mixture ratio from the computer program of reference 41.

The complete analysis and results for the RAM B2 conditions are given in appendix A. A simplified form of the energy equation which has been found to give fairly good estimates of required flow rates and also serves to identify the important parameters will be used in this section. This simplified energy equation is obtained by neglecting the kinetic energy of the injected liquid and also the kinetic energy of the gas mixture at the downstream exit station. (See eq. (A3) in appendix A.) The energy equation thereby becomes

$$\dot{m}_a \frac{V_\infty^2}{2} \approx \dot{m}_c \Delta h_{c,2} + \dot{m}_a \Delta h_{a,2} \tag{6}$$

30

where $\Delta h_{c,2}$ is the increase in enthalpy of the liquid from injection conditions to exit conditions and $\Delta h_{a,2}$ is the increase in the enthalpy of the air from free-stream conditions to exit conditions. The mass flow of air is given by

$$\dot{m}_a = f_i \pi r_i^2 \rho_\infty V_\infty \qquad (7)$$

where f_i is the fraction of the intercepted free-stream flow that is contained in the mixing region. The enthalpy increases of the liquid and air are computed from the approximate relations

$$\Delta h_{c,2} = h_{c,2} - h_{c,ref} + c_{p,v}\left(T_{ref} - T_{l,0}\right) + L$$

$$\Delta h_{a,2} = h_{a,2} - h_{a,ref} + c_{p,a}\left(T_{ref} - T_\infty\right)$$

The temperature at the end of the evaporation and mixing region T_2 is chosen so that for equilibrium conditions the electron concentration N_e would be less than 10^9 electrons/cm^3. Calculations (appendix A) indicate that $N_{e,2} < 10^9$ electrons/cm^3 for $T_2 \approx 5000^\circ$ R (2778° K) for a wide range of pressures and mass ratios of water vapor to air. It can also be shown from results given in appendix A that for a similar range of conditions and for $T_2 \approx 5000^\circ$ R (2778° K),

$$\Delta h_{c,2} \approx 4.4 \times 10^8 \; \frac{ft^2}{sec^2} \left(17\,500 \; \frac{Btu}{lbm}; \quad 40.7 \times 10^6 \; J/kg\right)$$

$$\Delta h_{a,2} \approx 0.5 \times 10^8 \; \frac{ft^2}{sec^2} \left(2000 \; \frac{Btu}{lbm}; \quad 4.6 \times 10^6 \; J/kg\right)$$

The large value of $\Delta h_{c,2}$ is due to the appreciable dissociation of water that has already occurred at this temperature and indicates the large heat-sink capability of water. For convenience, the ambient density in equation (7) is assumed to be given by the exponential form

$$\rho_\infty = \rho_{ref} e^{-\beta z}$$

Substituting equation (7) into equation (6) and rearranging then gives an expression for the coolant mass flow rate per unit of vehicle frontal area as

$$\frac{\dot{m}_c}{f_i \pi r_N^2} = \rho_{ref} \left(\frac{r_i}{r_N}\right)^2 V_\infty \frac{\frac{V_\infty^2}{2} - \Delta h_{a,2}}{\Delta h_{c,2}} e^{-\beta z} \qquad (8)$$

The nose radius of the vehicle is introduced as a convenient reference. Also the ratio r_i/r_N does not vary greatly for most blunt vehicles at zero angle of attack. Calculations in appendix A indicate that for RAM B flight conditions r_i/r_N varied from about 0.9 to 1.4 during the attenuation period of the flight, where r_i is the radius to the shock point

where the downstream value of N_e is less than 10^9 electrons/cm^3. For a blunt-face vehicle at angle of attack, such as the Apollo reentry module, r_i should be taken as the distance from an axis (parallel to the velocity vector) through the aerodynamic stagnation point to the critical streamline for $N_e < 10^9$.

Equation (8) shows that at a given altitude the flow rate (based on equilibrium cooling only) would vary essentially as the cube of the flight velocity and as the frontal area of the vehicle. If the injected material can be confined to a small slot on one side of the vehicle, then the required flow rate would be reduced by the fraction f_i, which is the ratio of this slot area to the cross-sectional area of the flow field. For large blunt vehicles at angle of attack, the flow rate can be reduced further by injecting from the windward side where r_i/r_N would be less than 1.0.

The coolant flow-rate parameter from equation (8) is plotted in figure 28 as a function of altitude for various flight velocities from 15 000 to 35 000 ft/sec (4.6 to 10.7 m/sec). Values used for ρ_{ref}, β, $\Delta h_{a,2}$, and r_i/r_N are given in the figure legend. For the RAM B vehicle with $r_N = 4$ inches (10.2 cm) and $f_i = 1$, the required flow rates from figure 28 would be about 0.27 lbm/sec (0.123 kg/sec) at 160 000 feet (48.8 km) of altitude and 0.007 lbm/sec (0.003 kg/sec) at 250 000 feet (76.2 km).

Included for comparison in figure 28 is a curve (dashed line) computed from the actual minimum flow rates injected on each side during the RAM B2 flight. The values of f_i used in this computation were obtained from figure 25. Since these minimum flow rates resulted in significant signal recovery over the entire data period (see fig. 26) it can be assumed that levels of N_e in the flow field were reduced to the critical value for VHF, or approximately 10^9 electrons/cm^3, corresponding to the value used in equation (8). A comparison of the dashed curve with the solid lines from equation (8) indicates that the assumptions of equilibrium cooling and complete evaporation should not be used. Refinements in the complete evaporation theory as presented in appendix A do not affect these results, so it is necessary to consider finite evaporation rates as the next significant improvement over the complete evaporation theory.

Finite evaporation rates: In the previous paragraphs, the amount of coolant required was estimated by assuming that all the injected material was evaporated and uniformly mixed at the downstream station, which, for the RAM B calculations, was taken as the forward antenna site. In actuality, the distance required to evaporate the spray depends on a number of variable factors such as initial droplet size, latent heat of the liquid, and flow-field densities. In order to determine whether the injected material can be utilized effectively as a coolant, it is necessary to examine the effect of these factors on evaporation rates.

The theoretical analysis described herein is intended to provide estimates of evaporation rates and distances for cross-current injection from a site which is well

downstream of the vehicle nose. The injected liquid is given an initial momentum normal to the approaching airstream so that approximations of the penetration and trajectories of the droplets can be obtained. The principal assumptions used in the derivation which is given in appendix B are as follows:

(1) Quasi-one-dimensional constant-pressure mixing and steady flow occurs.

(2) Flow upstream of injection site is uniform and parallel.

(3) Droplet size, velocity, and distribution at any streamwise station are uniform.

(4) Nusselt number and drag coefficient for the droplets (or ice particles) in the spray are the same as for isolated spheres.

(5) The effect of mass transfer on heat transfer is accounted for by using a "film" concept for the evaporating droplets.

(6) Atomization of the liquid jet occurs at the nozzle exit.

(7) The ratio of coolant mass flow to air mass flow entrained in the mixing region is constant.

(8) The droplet temperature is constant and is assumed to be the boiling temperature at the local static pressure in the vicinity of the droplet.

A similar analysis and approximate solutions are given in reference 18. The present results were obtained from solutions of the general equations (appendix B) on an IBM 7094 electronic data processing machine. The thermodynamic properties and the mole fractions of the constituents of the mixture of vapor and air were obtained as functions of pressure, enthalpy, and mass ratio of evaporated coolant to air from the computer program for chemical equilibrium compositions of reference 41. The initial droplet radius was obtained from the correlations of reference 42.

Application of the theory to conditions typical of the RAM B2 data period are shown in figures 29 and 30. In figure 29 the mixture temperature, electron concentration, and fraction of injected water still in liquid phase are plotted as a function of distance from the injection point. In figure 30 the mole fractions of the various constituents of the mixture are plotted as a function of distance from the injection point. Input values that represent conditions at three altitudes during the RAM B2 trajectory have been used in the calculations. These altitudes were taken as 157 000, 210 000, and 235 000 feet (47.8, 64.0, and 71.6 km) corresponding to 115, 145, and 165 seconds from launch, respectively, and the corresponding results are given in parts (a), (b), and (c) of figures 29 and 30. The local pressures used in the solutions correspond to a value of $C_p/C_{p,max}$ of 0.06, as obtained from reference 38. The initial airstream velocity and temperature used in the solutions are listed in table III. These values were computed for a streamline that traverses a normal shock at the given flight conditions and then isentropically expands to the local pressure with equilibrium air properties assumed.

At an altitude of 157 000 feet (47.8 km) (fig. 29(a)), more than 50 percent of the injected water would be evaporated at only 0.5 foot (0.15 m) from the injection point when $r_1 = 2.2 \times 10^{-5}$ foot (6.7 microns), which is the mean droplet radius for the local conditions as obtained from the correlations of reference 42. When the maximum droplet radius (r_1) of 6×10^{-5} foot (18 microns) (obtained from ref. 42) is used, about 35 percent of the injected liquid would be evaporated at $x = 0.5$ foot (0.15 m), and the mixture temperature is slightly higher. The mixture temperature decreases from the initial value of about 7300° R to 5000° R (4056° to 2778° K) in this distance and the electron concentration decreases accordingly. At an altitude of 210 000 feet (64.0 km) (fig. 29(b)) where the local pressure is about one-sixth that at the altitude of figure 29(a), the evaporation rate is considerably slower with about 25 percent of the injected water evaporated at 0.5 foot (0.15 m). At 2 feet (0.6 m) from the injection point, corresponding to the location of the forward antenna, about 40 percent has evaporated. According to the theoretical calculation, this percent evaporation still results in a significant reduction in temperature and electron concentration. At an altitude of 235 000 feet (71.6 km) (fig. 29(c)) where the pressure is only 2.64 lbf/ft^2 (126.4 N/m^2), just 25 percent of the injected water is evaporated at $x = 2$ feet (0.6 m).

The rapid reduction in temperature calculated for these conditions is caused partly by the large latent heat of water and specific heat of steam, but the greatest effect is caused by the dissociation of the water molecules, as indicated by the rapid increase in hydrogen atoms downstream of injection. (See fig. 30). The main source of electrons is the nitric oxide (NO), which is seen to increase up to about $x = 1$ foot (0.3 m). While the nitric oxide is increasing, the mixture temperature is decreasing, and the net effect is to reduce the electron number density N_e. The constituent that has the next largest effect on N_e was found to be the hydroxyl neutral (OH) which attaches an electron to form the negative hydroxyl ion. Although the mole fraction of OH becomes appreciable, it is still insufficient to give any significant reduction in N_e at these conditions except for the high-pressure condition (fig. 29(a)) for $x > 0.1$ foot (0.03 m), where there was as much as a 20-percent reduction in N_e due to the formation of OH$^-$.

It should be noted that for the three cases considered the predicted value of N_e at the forward antenna station was always less than 10^9 (fig. 29), an indication that for the value of W^* of 0.5, signal recovery would be expected if the assumptions of equilibrium ionic and thermodynamic conditions were valid. As mentioned previously, the value $W^* = 0.5$ is considered as a mean for the flow conditions between the injection site and the antenna station. Solutions for the minimum values of W^* from figure 25 were obtained to determine the effect of W^* on the computed levels of N_e. The results at $x = 2$ feet (0.6 m) are given in the following table:

Trajectory point			W^*	T		R^3	N_e, electrons/cm^3
Time, sec	Altitude						
	ft	km		$^\circ R$	$^\circ K$		
115	157×10^3	47.8	0.1	5410	3006	0.21	6×10^9
145	210	64.0	.14	5320	2956	.55	1.5
165	235	71.6	.23	5210	2894	.73	.5

Comparison of these values of T and R^3 with the curves of figure 29 at x = 2 feet (0.6 m) indicates that these values of R^3 are somewhat smaller and these values of T are larger than those for $W^* = 0.5$. The values of N_e decrease with altitude to or below the critical level, an indication that even for these small values of W^* water injection would be effective at the higher altitudes if equilibrium conditions could be achieved. The altitude trend indicated by these results is opposite to the trend shown by the data of figure 26 which showed, in general, a tendency for decreasing signal recovery with altitude for $W^* \gtrsim 0.3$.

Since the calculated homogeneous cooling depends on the amount of water evaporated, it is of interest to compare predictions from the finite evaporation theory with those from the simple theory assuming complete evaporation. The values listed in the following table correspond to the three altitude conditions used for figure 29:

Time, sec	Altitude		R^3 at x = 2 ft (0.6 m) (fig. 29)	Minimum $\dot{m}_c$ per side (fig. 12)		f_i (fig. 25)	$\dfrac{\dot{m}_v}{f_i \pi r_N^2}$
	ft	km		lbm/sec	kg/sec		
115	157×10^3	47.8	0.26	0.10	0.045	0.25	0.848
145	210	64.0	.59	.057	.026	.40	.167
165	235	71.6	.75	.037	.017	.50	.053

The parameter $\dot{m}_v$ is the flow rate of evaporated vapor given by the relation

$$\dot{m}_v = \left(1 - R^3\right)\dot{m}_c$$

These values of $\dot{m}_v/f_i \pi r_N^2$ are for the x = 2-foot (0.6-m) station and are plotted in figure 28 as the circular symbols. Comparison with the results of the simple theory (the solid lines) indicates that the amount of water vapor calculated to be present at the antenna station during the flight experiment is in reasonable agreement with the amount of water vapor calculated to give the observed signal recovery on the basis of the simple theory with complete evaporation. Since these calculated amounts of water vapor are based on the minimum water flow rates that resulted in signal recovery (fig. 26), it is apparent that the simplified equilibrium theory and equation (8) may be used to provide

design estimates of required water flow rates if the fraction of the injected water that evaporates is used in the equation as $\dot{m}_c$.

In order to obtain a further check on the validity of this simplified method for estimating water-flow-rate requirements, the results of the Gemini-Titan 3 (GT-3) reentry communication experiment (refs. 10 and 11) are analyzed in the same manner as that used for the RAM B2 results. In the GT-3 experiment, signal recovery was obtained on VHF down to an altitude of 245 500 feet (74.8 km) where a flow rate of $\dot{m}_c$ = 6.8 lbm/sec (3.1 kg/sec) was required to give marginal signal recovery (refs. 10 and 11). From reference 43 the values of f_i and R^3 at this altitude were f_i = 0.4 and R^3 = 0.75. Then with r_N = 3.75 feet (1.1 m) there is obtained

$$\frac{\dot{m}_V}{f_i \pi r_N^2} = 0.096 \frac{lbm}{sec\text{-}ft^2} \left(0.48 \frac{kg}{sec\text{-}m^2}\right)$$

which is plotted in figure 28 at the altitude of 245 500 feet (74.8 km). The vehicle velocity at this altitude was 23 840 ft/sec (7.3 km/sec), so the experimental value of 0.096 is somewhat higher than the predicted requirement according to equation (8). The agreement is considered remarkably good, however, since the size, configuration, and flow conditions for the GT-3 experiment are considerably different from those of the RAM case.

It should be emphasized that these results do not imply that homogeneous equilibrium recombination is responsible for the reduction in electron concentration for any of the present flight conditions. Rather, it may imply only that some other mechanism causes the N_e levels to approach equilibrium values.

Theory of free electron depletion by heterogeneous reactions.- The mechanisms for reduction in electron concentration to be considered in this section are ionic reactions that may occur at or in the immediate vicinity of the surface of the water droplets. At the low static pressures occurring in the flow field for flight conditions, the water droplets may freeze. When electrons collide with a droplet, which thus may be either liquid or solid, several things may occur: (1) the electrons could be reflected diffusely or specularly; (2) they could be attached to the water molecules or other species at or near the surface of the droplet; (3) they could recombine with ions which have also collided with the droplet; (4) they could be absorbed as free electrons and as such would remain on the surface of the droplet because of mutual repulsive forces.

The number of electrons that can be captured and held as free electrons by a droplet are limited by two main effects. One of these is the number of surface electron charges required to shatter the droplet against the forces of surface tension. Another effect limiting the rate of electron collisions is the repulsive forces due to net accumulative charge on the droplet. These limiting effects have been considered in reference 16,

36

where it is shown that for typical flight conditions the first effect is negligible. The repulsive forces due to accumulated charge vary the capture cross section, and after a very short transient period these forces limit the electron collision rate to the same as that for ions.

The present analysis (appendix C) considers the mean electron removal rate that occurs in the spray mixing region, and, by including an arbitrary capture efficiency factor or an effective capture cross section, any or all of the mechanisms mentioned previously can be accounted for. The objective of the analysis is to obtain estimates of effective values of the factor which would account for the observed effect of the water injection on signal attenuation in the RAM B2 flight. If the attachment or capture mechanisms considered here are the dominant ones, then these values can be compared with the theoretical predictions of reference 16 and also can be used to estimate the amount of water required to give signal recovery under different conditions.

Details of the analysis are given in appendix C. The general equation for electron concentration is

$$\frac{N_e}{N_{e,1}} = \frac{(V_m A_m)_1}{V_m A_m} \exp\left(-\frac{\dot{m}_c \bar{f}_c}{\frac{4}{3} r_1 \rho_l} \int_0^t \frac{R^2 V_e}{V_m A_m} dt\right) \tag{9}$$

where N_e is considered the peak value at any streamwise station. An approximate solution which is applicable near the injection site for RAM B2 conditions is

$$\frac{N_e}{N_{e,1}} = \exp\left[-178 \frac{\dot{m}_c}{\rho_{m,1} V_{m,1} A_{m,1}}\left(1 + W_{av}^*\right)^{0.149}\left(\frac{\rho_{m,1} x}{\rho_l r_1}\right)^{0.575} \bar{f}_c\right] \tag{10a}$$

or, solving for $\bar{f}_c$ gives

$$\bar{f}_c = -0.00562 \frac{\rho_{m,1} V_{m,1} A_{m,1}}{\dot{m}_c\left(1 + W_{av}^*\right)^{0.149}}\left(\frac{\rho_l r_1}{\rho_{m,1} x}\right)^{0.575} \ln\frac{N_e}{N_{e,1}} \tag{10b}$$

The apparent variation of $\bar{f}_c$ with altitude that would be required to reduce the value of N_e to 8×10^8 (the critical value for VHF transmission) is plotted in figure 31. The minimum water flow rates from figure 12 were used in the computation; other values used are given in table III. The initial values of electron concentration just upstream of the injection site $N_{e,1}$ are based on measured values obtained during the RAM B3 flight, as reported in reference 32. The lines shown in figure 31 are for constant values of r_1 as indicated, and the three circular symbols represent values of r_1 computed from the correlation equations of reference 42. Included for comparison are theoretical values computed by the method of reference 16 and semiempirical values from reference 11.

The values of $\bar{f}_c$ from these references, as well as the present empirical values, are all in reasonable agreement with experimental values deduced from the measurements of reference 17. It is therefore concluded that the principal mechanism causing signal recovery was the heterogeneous reactions. This conclusion is in agreement with the results of reference 11 where typical finite rate homogeneous reactions were included in the analysis and were found to have a negligible effect on electron depletion for the RAM B2 flight conditions.

Observed signal recovery during third-stage burning period.- Since the signal levels from the Coquina station (fig. 17) are free of rocket exhaust effects during third-stage burning (because of the favorable aspect angle, see figs. 6 and 11(c)), these data will be used for the discussion in this section. The first injection pulse was from the side nozzles and varied from about 1.0 to 2.0 lbm/sec (0.45 to 0.9 kg/sec) (fig. 12). Complete recovery was immediately obtained for the forward and middle antenna signals which had been attenuated by about 18 and 9 dB, respectively. The signal from the rear antenna had not as yet been attenuated noticeably.

The next side injection pulse started at 115.5 seconds, and by 117 seconds complete recovery occurred for the forward antenna (fig. 17(a)), but only partial recovery of 9 to 10 dB occurred for the middle and rear antennas (figs. 17(b) and 17(c)). This amount of recovery for the middle antenna signal was the same as that observed for the first side injection pulse from this antenna. This result would be expected since the minimum flow rate for the first side pulse (1.0 lbm/sec (0.45 kg/sec)) was the same as the maximum value for the second side pulse, and the pertinent values of W^* would then be about the same. The fact that full recovery occurred at the forward antenna but only partial recovery occurred at the downstream antennas indicates that for this flow rate there may have been narrow regions of plasma still present on each side of the conical portion of the vehicle (at locations displaced laterally 90° from the injection sites) where the spray had not penetrated. As the flow moved downstream, these narrow regions of high electron concentration would spread out by diffusion or mixing until transmission from the downstream antennas was partially blocked. The concentration of water spray would be much less at these downstream antennas than at the forward antenna because of the increased normal penetration of the spray as it is swept downstream. (See fig. 24.) Apparently the local water concentrations were then too small to reduce the average values of N_e below the critical level. These results indicate that it might be difficult to maintain a narrow slot of reduced levels of N_e for long streamwise distances of several feet in an ionized flow field. On the other hand, as mentioned previously, data for the downstream antennas probably should not be used for reliable estimates of N_e.

Observed signal recovery after third-stage burning.- In general, the side injection pulses did not result in complete signal recovery, and they were more effective for the

forward antenna than for the middle or rear antenna (figs. 15 to 18). The smallest recovery was generally obtained at the rear antenna. This decreasing effectiveness of side injection with increasing streamwise distance from the injection site has been discussed previously.

From third-stage burnout until about 140 seconds the maximum signal strength from the forward antenna during side injection was down only 2 to 8 dB from the recovery level obtained during stagnation injection. (See part (a) of figs. 15 to 17.) From 140 seconds to the end of the data period, the maximum signal strength was below recovery for stagnation injection by as much as 8 to 12 dB. This decrease in effectiveness of side injection with altitude has been noted previously in the discussion of figure 26 for $W^* \gtrsim 0.3$. Since W^* is increasing with altitude, the injected water is apparently being utilized less efficiently as the altitude increases. This reduced efficiency may be associated with changes in the heterogeneous processes with altitude.

The present analysis of equilibrium homogeneous cooling effects indicates that concentrations of N_e would be reduced to less than critical by these effects alone. (See fig. 29.) When the actual minimum injection rates are used together with the theoretical evaporation predictions, the resulting flow rates of water vapor are in reasonable agreement with simple theoretical predictions of flow rates required to give critical values of N_e, as shown by the points plotted in figure 28. Since these minimum flow rates apparently do correspond to approximately the minimum required to give significant (but not complete) signal recovery, it appears that the equilibrium homogeneous assumptions including finite evaporation rates give results which are in reasonable agreement with the experimental results. It is emphasized again, however, that homogeneous mechanisms do not account for the observed reductions in N_e, since the analysis of reference 11 of the combined effects of heterogeneous and homogeneous mechanisms indicated that the former was predominant. The assumptions of equilibrium homogeneous conditions merely provide a convenient design tool.

CONCLUDING REMARKS

A flight test has been conducted to determine whether radio attenuation during hypersonic flight can be alleviated by the injection of water into the flow field. The test vehicle was a cone-cylinder-flare configuration with a spherically blunted nose of 4-inch (10.2-cm) radius. Attenuation levels with and without water injection were measured during the ascending portion of the trajectory for transmission frequencies of 30.8, 225.7, 244.3, 5600, and 9210 megacycles over a range of altitudes from 120 000 to 290 000 feet (36.6 to 88.4 km) and a range of velocities from 9000 to 17 840 ft/sec (2.7 to 5.4 km/sec).

For the conditions of this test, the signals with frequencies of 5600 Mc and higher were not noticeably attenuated, but the lower frequency signals were attenuated because of the plasma from approximately 15 to 35 decibels, depending on the bandwidth characteristics and location of the antennas. The 244.3-megacycle signal was completely blacked out. Attenuation due to the plasma layer started at an altitude of 130 000 feet (39.6 km) and a velocity of 10 700 feet per second (3.3 km/sec) and ended at an altitude of approximately 250 000 feet (76.2 km) and a velocity of 17 400 feet per second (5.3 km/sec). During third-stage burning, attenuation due to rocket exhaust was observed at receiving stations located behind the vehicle.

Water injection was initiated at an altitude of 148 000 feet (45.1 km) and a velocity of 14 000 ft/sec (4.3 km/sec). The water was injected in pulses alternately from the stagnation region and from the sides just aft of the sphere-cone junction. Each pulse consisted of increasing flow-rate levels and was of 2 seconds duration. The pulses were separated by a no-injection period of 1 second.

After third-stage burnout and during stagnation injection, practically complete signal recovery was observed at all stations within range and for all attenuated frequencies. The minimum water flow rate varied during this time from about 0.3 lbm/sec to 0.1 lbm/sec (0.136 to 0.045 kg/sec). The forward penetration of the liquid jet may have been large enough to modify the bow shock to a sharp configuration. For these conditions, the production of free electrons would be reduced sufficiently to allow radio transmission. Oscillations in signal strength (apparently caused by fluctuations in forward penetration) and theoretical calculations indicated that homogeneous cooling mechanisms and heterogeneous mechanisms were also effective during stagnation injection. Consequently, it is not possible to identify any particular mechanism as the predominant cause of signal recovery for stagnation injection.

During third-stage burning, complete or substantial signal recovery was obtained from all vehicle antennas except the most rearward one, and at all ground stations except the two having the most rearward aspect angles. These results showed that attenuation due to rocket exhaust was not affected by water injection in this flight test.

In general, the side injection pulses did not result in complete signal recovery, and they were more effective for the forward slot antenna (244.3 Mc) than for the midbody ring antenna (30.8 Mc) or the rear flare antenna (225.7 Mc). The minimum flow rates for side injection decreased from about 0.1 to 0.05 lbm/sec (0.045 to 0.023 kg/sec) per side during the data period. The decreasing effectiveness with increasing streamwise distance from the injection site is believed to be caused by cross-current mixing and diffusion of free electrons that would come from forward regions of the flow field where the spray had not penetrated.

The fact that partial but significant signal recovery was obtained during side injection indicated that the minimum test flow rates used were near the minimum amounts required, and indicated that an evaluation of an empirical factor that represents a mean recombination efficiency factor for heterogeneous reactions can be made. Comparisons of the present values of this factor with theoretical calculations and laboratory measurements made elsewhere for an analogous factor indicate good agreement. Calculations in the present report indicate that the assumptions of finite evaporation rates and equilibrium conditions provide reasonable estimates of water flow rates required to give signal recovery. The principal mechanism for electron depletion, however, is apparently the heterogenous processes that occur on or near the surface of the water droplets.

Langley Research Center,
National Aeronautics and Space Administration,
Langley Station, Hampton, Va., August 12, 1966,
125-21-02-09-23.

APPENDIX A

COOLING PREDICTIONS BASED ON INTERCEPTED FLOW CONCEPT

By Ivan E. Beckwith, Dennis M. Bushnell, and James L. Hunt

The intercepted flow method is intended to provide estimates of injected mass flow that would be consistent with the concept of a cooling mechanism for reduction in electron concentration. The main parameter is the final equilibrium temperature T_2 of the mixture. A value of T_2 can be adopted that is presumably effective in electron suppression for a given set of experimental conditions (such as those of the RAM B2 flight) wherein a corresponding amount of injected material was observed to provide recovery of radio transmission. Whether this value of T_2 actually was obtained in the test is moot; the objective is merely to provide a consistent frame of reference for projection of experimental results to other conditions.

Assumptions

The principal assumptions used in the analysis are as follows:

1. The flow is one-dimensional and steady.

2. The coolant just penetrates to the streamline that has passed through the bow shock at a point which is the radial distance r_i from the vehicle axis. The values of r_i are determined such that for no injection this amount of intercepted air mass flow $\left(\pi r_i^2 \rho_\infty V_\infty\right)$ would have a mean electron concentration of 10^9 at the final downstream station in the flow field.

3. The coolant is completely evaporated and the mixture is in chemical and thermodynamic equilibrium at the downstream station.

4. For localized side injection, the flow-field pressures and body pressures are the same as for the undisturbed case, and the entering flow streamlines do not deviate from the meridian plane.

5. The bow shock shape ahead of the injection station is not modified by side injection.

The last two assumptions are based on the experimental observations of reference 18.

Equations

The control volume used for application of the conservation equations is defined in the following sketch:

APPENDIX A

$$\dot{m}_c = \frac{\pi d_o^2}{4} N \rho_l V_l$$

$$f_i = \frac{\theta_s}{\pi}$$

Sketch (a)
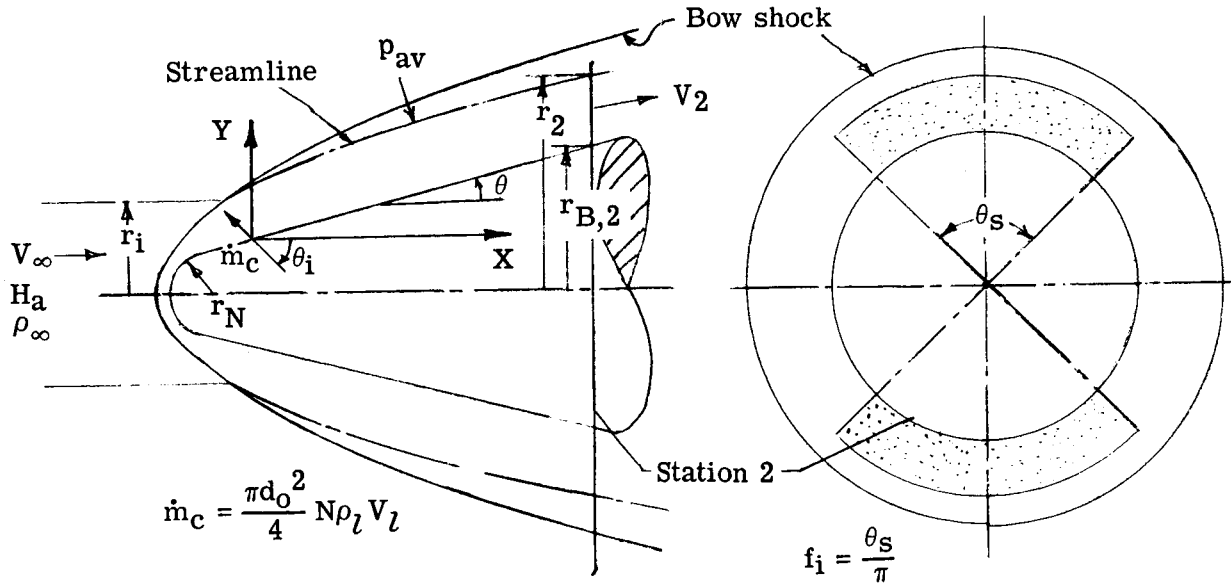
The coolant is injected at the rate $\dot{m}_c$ and the liquid jet may be inclined at the angle θ_i, as indicated. At station 2, the coolant is assumed to be distributed uniformly in the area $f_i \pi \left(r_2^2 - r_{B,2}^2 \right)$. For symmetrical injection from both sides of the vehicle, as for the RAM B2 flight, $f_i = \frac{\theta_s}{\pi}$. The previously mentioned assumptions then give the entering air mass flow as

$$\dot{m}_a = f_i \pi r_i^2 \rho_\infty V_\infty$$

Conservation of mass then requires that

$$f_i \pi r_i^2 \rho_\infty V_\infty + \dot{m}_c = f_i \pi \rho_2 V_2 \left(r_2^2 - r_{B,2}^2 \right)$$

or, from the definition of $W^* = \dfrac{\dot{m}_c}{\dot{m}_a}$, this equation can be written

$$1 + W^* = \frac{\rho_2 V_2}{\rho_\infty V_\infty} \left[\left(\frac{r_2}{r_i} \right)^2 - \left(\frac{r_{B,2}}{r_i} \right)^2 \right] \tag{A1}$$

The equation for conservation of momentum in the X-direction may be written as

$$\dot{m}_a V_\infty + f_i \pi r_i^2 p_\infty - f_i D_B + p_{av} f_i \pi \left(r_2^2 - r_i^2 \right) - \dot{m}_c V_l \cos \theta_i$$

$$= \left(\dot{m}_a + \dot{m}_c \right) V_2 \cos \theta + p_2 f_i \pi \left(r_2^2 - r_{B,2}^2 \right)$$

Division of this equation by $\dot{m}_a V_\infty$ and substitution for r_2/r_i from equation (A1) then gives

$$\left(\frac{V_2}{V_\infty}\right)^2 - \frac{U}{(1+W^*)\cos\theta}\frac{V_2}{V_\infty} - \frac{1}{\gamma M_\infty^2 \cos\theta}\frac{T_2}{T_\infty}\frac{\overline{M}_\infty}{\overline{M}_2}\left(\frac{p_{av}}{p_2} - 1\right) = 0 \qquad (A2)$$

where

$$U = 1 - \frac{1}{2}C_{D,B}\left(\frac{r_{B,2}}{r_i}\right)^2 + \frac{1 + \frac{p_{av}}{p_\infty}\left[\left(\frac{r_{B,2}}{r_i}\right)^2 - 1\right]}{\gamma M_\infty^2} - W^*\frac{V_l}{V_\infty}\cos\theta_i$$

$$C_{D,B} = \frac{D_B}{\frac{1}{2}\rho_\infty V_\infty^2 \pi r_{B,2}^2}$$

and, from the equation of state, $\frac{\rho_2}{\rho_\infty} = \frac{p_2}{p_\infty}\frac{T_\infty}{T_2}\frac{\overline{M}_2}{\overline{M}_\infty}$. The quantity D_B is the total body drag for a hemisphere-cone of base radius $r_{B,2}$, and may include the skin-friction drag.

The conservation of energy requires that

$$\dot{m}_a H_a + \dot{m}_c\left(h_{c,0} + \frac{V_l^2}{2}\right) = (\dot{m}_a + \dot{m}_c)h_2 + (\dot{m}_a + \dot{m}_c)\frac{V_2^2}{2} \qquad (A3)$$

where the heat transfer to the body surface is neglected. In order to utilize the computer program of reference 41, it is convenient to define a reference enthalpy as

$$h_{ref} = h_2 - \Delta h$$

where $\Delta h = \Delta h(p_2, T_2, W^*)$ and at T_{ref} all the constituents of the mixture are in the gas phase and still undissociated. The first term on the right-hand side of equation (A3) can then be written as

$$(\dot{m}_a + \dot{m}_c)h_2 = (\dot{m}_a + \dot{m}_c)\Delta h + \dot{m}_a h_{ref,a}$$

$$+ \dot{m}_c\left[h_{c,0} + c_{p,l}(T_s - T_{l,0}) + c_{p,v}(T_{ref} - T_s) + L\right]$$

and equation (A3) then becomes

$$\left(\frac{V_2}{V_\infty}\right)^2 = \frac{1 + \frac{2c_{p,a}(T_\infty - T_{ref})}{V_\infty^2}}{1 + W^*} - \frac{W^*}{1 + W^*}J - \frac{2\Delta h}{V_\infty^2} \qquad (A4)$$

where

$$J = \frac{1}{2} V_\infty^2 \left[L + c_{p,l}\left(T_s - T_{l,0}\right) + c_{p,v}\left(T_{ref} - T_s\right)\right] - \left(\frac{V_l}{V_\infty}\right)^2$$

<div align="center">Calculation of r_i</div>

As mentioned previously, the radius of the entering stream tube of air is obtained by specifying that this amount of air would have a mean electron concentration $N_{e,2}$ of 10^9 electrons/cm^3 at the downstream station for the condition of no injection. This value was chosen for application to the RAM B2 flight with the idea that it would certainly result in the maximum amount of air that would have to be cooled.

Equations (A2) and (A4) are used with $W^* = 0$ to obtain the required values of r_i. Thus, by setting $W^* = 0$ and solving equation (A2) for $r_i/r_{B,2}$, there is obtained

$$\frac{r_i}{r_{B,2}} = \left[\frac{\frac{1}{2} C_{D,B} - \frac{1}{\gamma M_\infty^2} \frac{p_{av}}{p_\infty}}{1 - \frac{V_2}{V_\infty}\cos\theta + \frac{V_\infty}{V_2} c \cos\theta - \frac{1}{\gamma M_\infty^2}\left(\frac{p_{av}}{p_\infty} - 1\right)} \right]^{1/2} \tag{A5}$$

where, from equation (A4) with $W^* = 0$,

$$\frac{V_2}{V_\infty} = \left[1 - \left(\frac{2h_2}{V_\infty^2}\right)_{W^*=0} + \frac{2c_{p,a}T_\infty}{V_\infty^2} \right]^{1/2} \tag{A6}$$

The quantity c is defined as

$$c = \frac{1}{\gamma M_\infty^2 \cos\theta}\left(\frac{T_2}{T_\infty}\frac{\overline{M}_\infty}{\overline{M}_2}\right)_{W^*=0}\left(\frac{p_{av}}{p_2} - 1\right)$$

For the given values of p_2 and the specified value of $N_{e,2}$ $\left(10^9 \text{ electrons/cm}^3\right)$, the corresponding values of T_2, M_2, and h_2 are obtained for air. Then with $C_{D,B}$ and p_{av} specified, the corresponding value of r_i is calculated from equations (A5) and (A6). These values of r_i are then used in the general equations (A2) and (A4) to find the values of W^* required to give specified temperatures at station 2. The values of $\left(r_i/r_N\right)^2$ used in the calculation are plotted in figure 32. This radius ratio is related to the reference air mass flow $\dot{m}_{ref}$ by the equation

$$\left(\frac{r_i}{r_N}\right)^2 = \frac{1}{f_i W^*}\frac{\dot{m}_c}{\dot{m}_{ref}}$$

APPENDIX A

where

$$\dot{m}_{ref} = \pi r_N^2 \rho_\infty V_\infty$$

Application

Equations (A2) and (A4) are solved simultaneously for V_2/V_∞ and T_2, with W^* as a parameter. The molecular weight of the mixture $\overline{M}_2$ and Δh were obtained by using the computer program of reference 41. Typical plots of Δh as a function of T for various values of W^* are shown in figure 33. These plots illustrate the effect of the large heat of dissociation of water vapor on the enthalpy of the air-water mixture, and they indicate that dissociation of the water vapor is appreciable at 4500° R (2500° K). The pressures of 0.005 and 0.0005 atmosphere are representative of flow-field pressures for the RAM B2 flight, as indicated by figure 34, which is a time-variation plot of typical pressures based on the flow-field solutions of reference 38.

The variation of electron concentration with temperature for mixtures of air and water vapor for typical pressures is shown in figure 35. These plots show that for equilibrium conditions the electron concentration at a fixed temperature and pressure is generally reduced slightly by the addition of water vapor. In these calculations, the concentrations of neutrals were obtained with the computer program of reference 41, and the main contributing ions for temperatures below 7200° R (4000° K) were found by using Saha's equation to be NO^+, O_2^+, H_2O^+, and OH^-. Above 7200° R (4000° K), the main contributors were H^+, N^+, and O^+.

The results of the calculation for the RAM B2 flight conditions are shown in figure 36 where T_2 is plotted as a function of W^* for six trajectory points from 110 to 190 seconds. Station 2 in this figure was taken at an axial distance of 25 inches (63.5 cm) from the nose near the upstream end of the 244.3-Mc slot antenna (see fig. 2). Figure 36(a) is for side injection with a body drag coefficient $C_{D,B}$ of 0.30, and figure 36(b) is for nose injection with a value of $C_{D,B}$ of 0.06. This latter value would be for the condition when the bow shock is pointed, as obtained in reference 18 for large mass flow ratios.

Figures 38 and 37(b) were obtained by interpolation for W^* from figures 36(a) and 36(b), respectively, at the desired values of T_2. The coolant mass flow ratio was then computed from the identity

$$\dot{m}_c = \pi f_i r_i^2 \rho_\infty V_\infty W^*$$

where r_i was obtained from figure 32.

The computed water flow rates for injection from the stagnation region, shown in figure 37, are not affected by f_i, which would always be unity for this case. For large injection rates, the body drag would be changed because of the effect of stagnation

46

APPENDIX A

injection on the bow shock shape. In reference 18, it was shown that when the ratio of the momentum of the injected liquid to the momentum of the airstream contained in a stream tube of model nose diameter exceeded about 0.01, then the bow shock modification becomes appreciable. For small values of this momentum ratio parameter of about 0.005 or less, the bow shock is essentially undisturbed. The minimum and maximum extremes in body drag due to changes in bow shock shape can therefore be approximated, respectively, as the drag for a sharp 9° cone, corresponding to large shock modification, and the drag for the undisturbed hemisphere cone, corresponding to small shock modification and small injection flow rates.

This maximum body drag is used in figure 37(a) and the minimum drag is used in figure 37(b). These results show that a smaller injection flow rate is required to obtain a given value of T_2 when the minimum drag is used, that is, when the momentum ratio is large enough to modify the shock. As discussed previously (see the section entitled "Stagnation Injection"), the spray penetration was probably large enough during most of the injection period to modify the shock to some extent. The predicted water flow rates corresponding to actual body drag would therefore be somewhere between the extremes shown in figures 37(a) and 37(b). It is thus indicated by comparison of the predicted curves for $T_2 = 4000^\circ$ R $(2200^\circ$ K$)$ with the actual flow rates injected at the stagnation region (also plotted in fig. 37) that the minimum amount supplied would be sufficient to give signal recovery, on the basis of this idealized analysis of equilibrium cooling effects.

Typical results for side injection are shown in figure 38 where the predicted values of water flow rates $\dot{m}_c$ for various mixture temperatures T_2 are plotted as a function of time from launch. Also included in the figures are curves representing the envelopes of the maximum and minimum mass flow rates injected during the flight, as obtained from figure 12.

The value of W^* in these calculations corresponds to the mass ratio of water vapor to air required to give the specified value of T_2 at the downstream station. These values of T_2 were taken as 2000°, 3000°, and 4000° R $(1100^\circ$, 1700°, and 2200° K$)$. On the basis of the tests of reference 18, the value of f_i for injection from both sides has been estimated to range from about 0.5 to 1, depending on the number of orifices operating and the altitude. (Typical values of f_i for injection from one side are shown in fig. 25).

The value of f_i of 0.5 which was used for figure 38(a) thus represents conditions at lower altitudes, or when only a few orifices are operating. A value of f_i of 0.75, as used in figure 38(b), is more representative of conditions at higher altitudes, or when all injection nozzles are operating. The numbers with each computed point in figure 38(a) are the values of W^* which are obtained from cross plots of T_2 as a function of W^*, as discussed previously. The equilibrium electron concentration for $T_2 = 4000^\circ$ R

(2200° K) (the maximum value used in the calculations) would be less than 10^9 electrons/cm^3. Thus the present idealized cooling analysis, in which complete evaporation and equilibrium conditions were assumed, indicates that the minimum flow rates for side injection during the flight should be sufficient to give signal recovery since these minimum flow rates are generally larger than the predictions for $T_2 = 4000^{\circ}$ R (2200° K).

APPENDIX B

QUASI-ONE-DIMENSIONAL THEORY FOR MEAN

DROPLET MOTION AND EVAPORATION

By Ivan E. Beckwith and Sadie P. Livingston

General Equations

The following approximate theoretical analysis is intended to provide first-order estimates of spray penetration and evaporation times and distances. Since a rigorous treatment of the problem is not at present feasible, several assumptions are introduced in order to simplify the solution. It is believed, however, that the essential characteristics and parameters of the problem are retained. The analysis is similar to that of reference 44.

Steady flow is assumed and the conservation of mass, momentum, and energy is required in a control volume indicated in the following sketch:

Sketch (b)
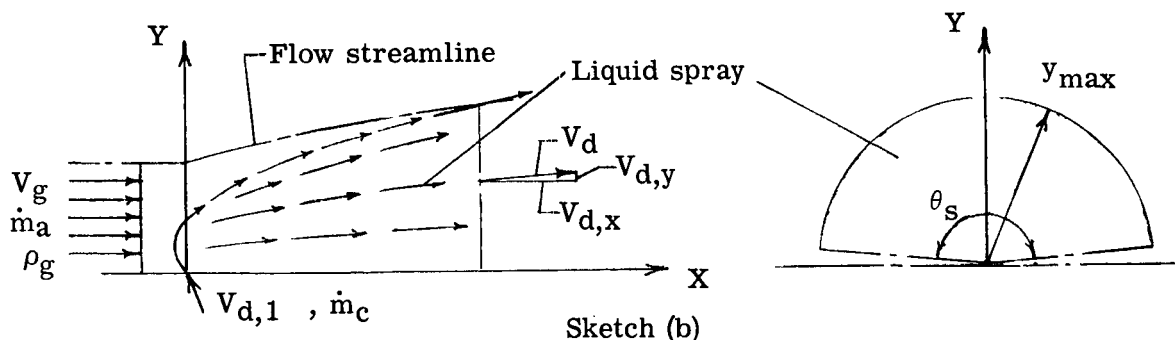
It is assumed that the liquid jet is injected into a parallel and uniform gas stream from a single point at the origin where it breaks up into a spray of uniformly sized droplets. At some distance x from the origin, the spray is assumed to be uniformly distributed over an area $\frac{1}{2}\theta_s y_{max}^2$, and the mean effective velocity of the droplets is $V_d = \sqrt{V_{d,x}^2 + V_{d,y}^2}$. The mean velocity of the mixture at this same station is $V_m = \sqrt{V_{m,x}^2 + V_{m,y}^2}$; therefore, the local relative velocity between droplets and gas mixture is $V = \sqrt{\left(V_{m,x} - V_{d,x}\right)^2 + \left(V_{m,y} - V_{d,y}\right)^2}$.

Conservation of mass.- The free-stream mass flow rate contained in the spray region at any station x is $\dot{m}_a$. Hence

$$\dot{m}_a + \dot{m}_c = \dot{m}_m + \dot{m}_l \tag{B1}$$

where $\dot{m}_c$ is the injected coolant mass flow rate (a constant), $\dot{m}_m$ is the mass flow rate of the mixture of gas and evaporated coolant, and $\dot{m}_l$ is the mass flow rate of

coolant still in liquid form. The mean droplet radius r is therefore defined by

$$\left(\frac{r}{r_1}\right)^3 \equiv R^3 = \frac{\dot{m}_l}{\dot{m}_c} \tag{B2}$$

where r_1 is the initial droplet radius at the injection site. The ratio of injected coolant flow rate to the flow rate of gas is

$$W^* = \frac{\dot{m}_c}{\dot{m}_a} \tag{B3}$$

which is, in general, a function of x because of the spreading of the liquid spray as it is blown downstream. From equations (B1), (B2), and (B3),

$$\frac{\dot{m}_m}{\dot{m}_c} = 1 - R^3 + \frac{1}{W^*} \tag{B4}$$

Momentum.- The mixing and evaporation process is assumed to occur at constant pressure; therefore, if shear forces at the body surface are neglected, the momentum equation in the X-direction is

$$\dot{m}_a V_{g,x} + \dot{m}_c V_{d,x,1} = \dot{m}_m V_{m,x} + \dot{m}_l V_{d,x} \tag{B5}$$

By the use of equations (B2), (B3), and (B4), equation (B5) can be written as

$$V_{m,x} = \frac{V_{g,x} + W^* V_{d,x,1} - W^* R^3 V_{d,x}}{1 + W^*\left(1 - R^3\right)} \tag{B6}$$

Similarly, the momentum equation in the Y-direction is

$$V_{m,y} = \frac{V_{g,y} + W^* V_{d,y,1} - W^* R^3 V_{d,y}}{1 + W^*\left(1 - R^3\right)} \tag{B7}$$

Energy.- If the heat transfer to the model surface is neglected, then conservation of energy requires that

$$\dot{m}_a\left(h_{g,1} + \frac{V_g^2}{2}\right) + \dot{m}_c\left(h_{l,1} + \frac{V_{d,1}^2}{2}\right) = \dot{m}_m\left(h_m + \frac{V_m^2}{2}\right) + \dot{m}_l\left(h_l + \frac{V_d^2}{2}\right) \tag{B8}$$

The use of equations (B2), (B3), and (B4), the introduction of the latent heat as

$$L = h_{v,s} - h_{l,s}$$

and the assumption that

$$h_l = h_{l,1} = h_{l,s}$$

then give the result

$$\Delta h_m = \left[1 + W^*(1 - R^3)\right]^{-1} \left\{ \frac{V_\infty^2}{2} - \left(h_{ref} - h_\infty\right)_g + W^*\left(\frac{V_{d,1}^2}{2} - R^3 \frac{V_d^2}{2}\right) \right.$$

$$\left. - W^*(1 - R^3)\left[L + \left(h_{ref} - h_s\right)_v\right] \right\} - \frac{1}{2} V_m^2 \tag{B9}$$

where $\Delta h_m = h_m - h_{m,ref}$. For convenience in the use of the computer program of reference 41, the value of T_{ref} is chosen to be between the condensation temperature and the dissociation temperature of the injected material; therefore,

$$h_{m,ref} = \left[1 + W^*(1 - R^3)\right]^{-1}\left[W^*(1 - R^3)h_{v,ref} + h_{g,ref}\right]$$

which has been used to obtain equation (B9).

Motion of droplets.- The total force on a droplet is

$$F = \frac{1}{2} \rho_m V^2 \pi r^2 C_D \tag{B10}$$

The force in the X-direction is given by the mass times the acceleration

$$F_x = \frac{4}{3} \pi \rho_l r^3 \frac{dV_{d,x}}{dt} \tag{B11}$$

If the droplet is spherical, the total force vector is in the same direction as the relative velocity V, so that

$$F_x = \frac{V_{m,x} - V_{d,x}}{V} F$$

The acceleration in the X-direction can then be written as

$$\frac{dV_{d,x}}{dt} = \frac{3}{8\rho_l r_1} \frac{\left(V_{m,x} - V_{d,x}\right)V\rho_m}{R} C_D \tag{B12}$$

Similarly, the acceleration in the Y-direction is

$$\frac{dV_{d,y}}{dt} = \frac{3}{8\rho_l r_1} \frac{\left(V_{m,y} - V_{d,y}\right)V\rho_m}{R} C_D \tag{B13}$$

For convenience in machine computations, two expressions for drag coefficient for different ranges in Mach number are used. For $M \geq 0.5$, an expression similar to that of reference 45 is

$$C_D = C_{D,C} + \left(C_{D,FM} - C_{D,C}\right)e^{-A\left(N_{Re,f}\right)^n} \tag{B14}$$

51

where

$$M = \frac{V}{\sqrt{\gamma_m \overline{R}_m T}}$$

$$N_{Re,f} = \frac{\rho_m V 2r}{\mu_f}$$

The quantities $C_{D,C}$, $C_{D,FM}$, A, and n are given as functions of M in table IV. The basic expression of reference 45 was modified to match the data of references 46 to 48. The values for the continuum drag coefficient $C_{D,C}$ are taken from the data of references 49 and 50, while the values for the free molecule drag coefficient $C_{D,FM}$ are taken from reference 51, page 704. An expression for M < 0.5 was also derived to match available data (refs. 52 and 53) and is

$$C_D = \frac{(C_D)_{M=0} + \frac{51.1M}{N_{Re,f}}}{1 + 0.256M\left[(C_D)_{M=0} + \frac{51.1M}{N_{Re,f}}\right]} \tag{B15}$$

where

$$(C_D)_{M=0} = \frac{24}{N_{Re,f}} + 0.4 + 1.6 \exp\left[-0.028(N_{Re,f})^{0.82}\right] \tag{B16}$$

Heat transfer to droplets.- The heat-transfer rate per unit area into a droplet is assumed to be used entirely for the heat of vaporization, and radiation is neglected; therefore

$$4\pi r^2 q = -L \frac{4}{3}\pi \rho_l \frac{dr^3}{dt}$$

or

$$q = -\frac{1}{2}\frac{\rho_l L}{r}\frac{dr^2}{dt}$$

The Nusselt number for heat transfer to the droplets is defined as

$$N_{Nu} = \frac{q 2r c_{p,w,0}}{k_f(h_{aw} - h_w)_0}$$

where the subscript 0 denotes zero mass transfer conditions and k_f is the droplet film thermal conductivity. Because of the small size of the droplets and their associated boundary layer or film, it is assumed that the gas composition is frozen across the film, so that

$$(h_{aw} - h_w)_0 = \eta_{r,0}\frac{V^2}{2} + \bar{c}_{p,m}(T_m - T_w)$$

where $\bar{c}_{p,m}$ is the frozen specific heat of the mixture and $\eta_{r,0}$ is the recovery factor for the droplet with zero mass transfer.

During the lifetime of the droplet its relative velocity varies from approximately V_g to zero, and its radius varies from r_1 to zero. If the initial acceleration is large and the evaporation rate is small, the relative velocity may become small before the droplet has lost much mass. The Nusselt number may thus vary from values in the free molecule regime up to values in the continuum regime. In order to provide for a continuous transition from free molecule to continuum values and also to include the effect of mass transfer on heat transfer, the Nusselt number is written as

$$N_{Nu} = \frac{N_{Nu,C}\frac{q}{q_0}}{1 + \frac{N_{Nu,C}\frac{q}{q_0}}{N_{Nu,FM}}} \tag{B17}$$

This expression is similar to one developed by Kavanau (ref. 51, p. 725). The ratio q/q_0 is adapted from reference 54, page 21 as

$$\frac{q}{q_0} = \frac{L}{c_{p,v,f}\Delta T} \ln\left(1 + \frac{c_{p,v,f}\Delta T}{L}\right) \tag{B18}$$

where

$$\Delta T = \eta_{r,0}\frac{V^2}{2\bar{c}_{p,m}} + T - T_w$$

The expression for the Nusselt number in continuum flow is (ref. 54, p. 22)

$$N_{Nu,C} = 2 + 0.6\left(N_{Pr,f}\right)^{1/3}\left(N_{Re,f}\right)^{1/2} \tag{B19}$$

where, for the present analysis,

$$N_{Pr,f} = \left(\frac{\bar{c}_p\mu}{k}\right)_f$$

The Nusselt number for free molecule flow is written as

$$N_{Nu,FM} = \frac{\gamma_m + 1}{\gamma_m} N_{St}\rho_m V 2r \frac{c_{p,w}}{k_f} \frac{\eta_{r,FM}\frac{V^2}{2} + h_m - h_w}{\eta_{r,0}\frac{V^2}{2} + h_m - h_w} \tag{B20}$$

where it is again assumed that $h_m - h_w = \bar{c}_{p,m}(T - T_w)$. The free molecule Stanton number N_{St} is given in reference 51, page 699. This exact variation of N_{St} can be matched satisfactorily by the expression

APPENDIX B

$$N_{St} = \frac{0.104}{S^{1.14}} + 0.125\left[1 - e^{-1.166(S)^{0.408}}\right] \tag{B21}$$

where

$$S = \frac{V}{\sqrt{2\overline{R}_m T}}$$

The free molecule recovery factor $\eta_{r,FM}$ (ref. 51, p. 699) can be matched by the expression

$$\eta_{r,FM} = \frac{\gamma_m}{\gamma_m + 1}\left(2 + 0.7e^{-0.707S}\right) \tag{B22}$$

Gas Properties

Thermodynamic properties.- The thermodynamic properties of the mixture of gas and vapor depend on the ratio of the mass of evaporated coolant to the mass of original gas

$$\overline{W}^* = W^*\left(1 - R^3\right) \tag{B23}$$

The ideal gas law is used for the density

$$\rho_m = \frac{p}{\overline{R}_m T} \tag{B24}$$

where, for thermodynamic equilibrium

$$T = T\left(h_m, p, \overline{W}^*\right) \tag{B25}$$

$$\overline{R}_m = \frac{\mathcal{R}}{\overline{M}_m} \tag{B26}$$

The computer program of reference 41 for the equilibrium thermodynamic properties of arbitrary gas mixtures is used in the present solution.

An alternate procedure for evaluating the thermodynamic properties is also available wherein the gas species entering the control volume at the injection site are assumed to be frozen and the evaporated liquid is assumed not to dissociate. The specific heats of the entering gas mixture and the evaporated liquid are assumed to be constant. This procedure was used for the computations of reference 40 and is described in more detail in that report.

Transport properties.- The transport properties were computed from the mixture equations of reference 55 when the gases are all nonpolar. The film viscosity and thermal conductivity were evaluated at the film temperature, which is defined as

54

APPENDIX B

$$T_f = \frac{1}{2}\left(\frac{V^2}{2\bar{c}_{p,m}} + T + T_w\right)$$ (B27)

The mole fractions of the various gas species, as required in the equations of reference 55, were modified to represent an average composition in the film. Because of the small thickness of the film, it was assumed that for the computation of transport properties no recombination of free-stream species or dissociation of the evaporated liquid takes place within the film. Thus, if X_1 is the mole fraction of the gas phase of the injected material, the value in the film is

$$X_{1,f} = \frac{1}{2}\left(X_{1,w} + X_{1,m}\right)$$ (B28)

It was also required that for any other species

$$\frac{X_{i,f}}{\displaystyle\sum_{i=2}^{\nu} X_{i,f}} = \frac{X_{i,m}}{\displaystyle\sum_{i=2}^{\nu} X_{i,m}}$$ ($i \geq 2$) (B29)

so that from equation (B28) and the requirement that $\displaystyle\sum_{i=1}^{\nu} X_{i,f} = \sum_{i=1}^{\nu} X_{i,m} = 1$, the mole fraction of the other species in the film is

$$X_{i,f} = \frac{1 - \frac{1}{2}\left(X_{1,w} + X_{1,m}\right)}{1 - X_{1,m}} X_{i,m}$$ ($i \geq 2$) (B30)

where there are ν species present and $X_{i,m}$ are the mole fractions in the free stream as obtained with the computer program of reference 41.

When one or more of the gases present was highly polar, as for example water vapor, the viscosity was still computed from the equations of reference 55 with the constants obtained from reference 56. In the calculation of thermal conductivity, however, two alternate methods were programed. In the first method the term which would normally appear in the mixture equations of reference 55 for water vapor (species 1) as

$$0.88\left(\frac{2}{5}\frac{\overline{M}_1 c_{p,1}}{\mathcal{R}} - 1\right)$$

was replaced by

$$\left(\frac{4}{15}\frac{\overline{M}_1 c_{p,1}}{\mathcal{R}} - 1\right)$$

since the data for water in references 57 and 58 indicate that the value of the Prandtl number for water vapor may be assumed as unity for a wide range of conditions. In the second method, the film viscosity was assumed to be that of water by using the method and constants of reference 56. The film thermal conductivity was then computed from this viscosity by assuming that $N_{Pr} = 1$ and by using the specific heat of water from the program of reference 41. It should be noted that both methods gave essentially the same results when applied to the conditions shown in figures 29 and 30 of the text.

Solution

The equations derived in this appendix have been programed for solution on the IBM 7094 electronic data processing machine. The integration technique employed is based on the classical fourth-order Runge-Kutta method and a variable interval size. The variable interval size controls local truncation error by comparing a full-step size with two half-step sizes, and adjusting the interval accordingly. Extrapolation to zero interval size is then employed, which gives rise to fifth-order integration. Partial double precision is used internally to control roundoff error. The equilibrium thermodynamic properties of the gas mixture are computed at each step of the Runge-Kutta method.

In these solutions, W^* has been assumed constant, since no satisfactory method for determination of θ_s and y_{max} was found. This assumption yields reasonable results (within the basic limitations of the theory) except in the region just downstream of the injection site. In order to simplify the calculations, γ_m was taken as the frozen specific-heat ratio of the mixture.

APPENDIX C

FREE ELECTRON DEPLETION BY HETEROGENEOUS REACTIONS

By Ivan E. Beckwith

In this appendix a quasi-one-dimensional analysis is developed that accounts for all possible ionic or attachment processes that may occur on or near the surface of water droplets (or ice particles). These processes are known as heterogeneous reactions, since their occurrence depends on the presence of an interface (the droplet surface) between the liquid and the gas. The analysis is similar to that of reference 11 except that homogeneous recombination terms are not included since it was shown in that reference that these terms as formulated did not have any significant effect.

Conservation of Free Electrons

A control volume is set up that is bounded by gas flow streamlines, as indicated in the following sketch:

Sketch (c)
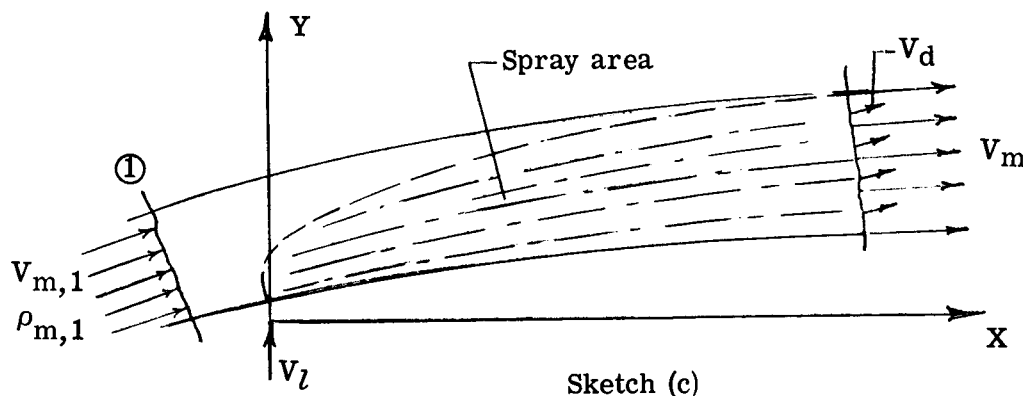
The parameter $V_{m,1}$ is the mean mass velocity of the gas entering the control volume. The concentration of free electrons in this gas is $N_{e,1}$; therefore, the number of free electrons entering the control volume per unit time is

$$N_{e,1} V_{m,1} A_1 \tag{C1}$$

At some station x distance downstream, the gas mixture velocity is V_m and the droplet velocity V_d. The number of free electrons leaving the control volume at this station is

$$N_e V_m A_m \tag{C2}$$

where, in general, $A = A_m + A_l$.

Now if it is assumed that the only mechanism present for removal of free electrons from the gas flow is heterogeneous reactions at or near the surface of the droplets, there

would be a total of (on the average) $\bar{n}$ free electrons removed from the gas flow per drop, during the time a "mean" droplet traverses the distance x from the injection site to station x. The number of droplets leaving at station x is

$$N_d V_d A$$

where V_d is the droplet velocity (average) and N_d is the droplet concentration

$$N_d = \left(\frac{\dot{m}_c}{\frac{4}{3} \pi r_1^3 \rho_l} \right) \frac{1}{V_d A} \tag{C3}$$

The quantity in the brackets is the number of droplets per second that are injected into the control volume. For steady flow this number is a constant.

In order to conserve the number of electrons originally entering as free electrons, the following equation must be satisfied:

$$N_{e,1} V_{m,1} A_1 = N_e V_m A_m + \bar{n} N_d V_d A$$

or, from equation (C3),

$$N_{e,1} V_{m,1} A_1 = N_e V_m A_m + \bar{n} \frac{\dot{m}_c}{\frac{4}{3} \pi r_1^3 \rho_l} \tag{C4}$$

Rate of Electron Depletion Per Droplet

From simple kinetic theory concepts, an approximate expression for the number of free electrons removed (per unit time per unit volume) by heterogeneous reactions from a static gas with suspended particles is

$$f_c \pi \bar{r}^2 N_d N_e V_e \tag{C5}$$

where V_e is the mean thermal velocity of the electrons, f_c is a capture efficiency factor, or the fraction of total collisions (as defined) that result in the removal of an electron, and $\bar{r}$ is the radius of the effective collision cross section of the droplets or ice particles. The parameters N_d and N_e are the droplet and electron concentrations in a system that would be at rest; that is, there is no relative mean mass motion between gas, electrons, and droplets. If relative motion between the gas and droplets is imposed, it is assumed that the effect would be small, since any mean mass velocity would be small compared with V_e. Thus, for application of equation (C5) to a dynamic system, it can be assumed that the rate of removal of free electrons per droplet is given by

$$\frac{d\bar{n}}{dt} = f_c \pi \bar{r}^2 N_e V_e \tag{C6}$$

where, by definition, the time derivative follows the mean droplet.

58

~~CONFIDENTIAL~~

APPENDIX C

General Equation

Taking the derivative of equation (C4) (following the droplet) gives

$$\frac{d}{dt}\left(N_e V_m A_m\right) = - \frac{\dot{m}_c}{\frac{4}{3}\pi r_1^3 \rho_l}\frac{d\bar{n}}{dt}$$

Substitution of equation (C6) and rearrangement gives

$$\frac{d\left(N_e V_m A_m\right)}{N_e V_m A_m} = - \frac{\dot{m}_c}{\frac{4}{3} r_1 \rho_l}\frac{\left(\frac{\bar{r}}{r}\right)^2 f_c R^2 V_e}{V_m A_m}dt$$

where $R = \frac{r}{r_1}$. Integrating over the time of "flight" or exposure of the mean droplet then gives

$$\frac{N_e}{N_{e,1}} = \frac{\left(V_m A_m\right)_1}{V_m A_m}\exp\left(-\frac{\dot{m}_c \bar{f}_c}{\frac{4}{3} r_1 \rho_l}\int_0^t \frac{R^2 V_e}{V_m A_m}dt\right) \qquad (C7)$$

where $\bar{f}_c$ is a mean effective value of the product $(\bar{r}/r)^2 f_c$ over the specified time interval. As mentioned previously, the objective is to evaluate $\bar{f}_c$ from the RAM B2 flight results, where signal recovery was obtained by water injection. Then with the assumption that the same values apply to other situations, it should be possible to determine the minimum injection mass flow of water required to give signal recovery for any other problem where the flow variables, geometry, and size are not too different from the RAM B2 case.

Approximate Solution

Because of the exponential form of equation (C7), most of the reduction in N_e would occur for small times before the droplets move very far downstream. For this condition, the values of ρ_m, V_e, and r can be assumed constant at their initial values, and the conservation of mass requires that $V_m A_m = V_{m,1} A_{m,1}$. Equation (C7) then becomes

$$\frac{N_e}{N_{e,1}} = \exp\left(-\frac{\dot{m}_c \bar{f}_c}{\frac{4}{3} r_1 \rho_l}\frac{V_{e,1}}{V_{m,1} A_{m,1}}t\right) \qquad (C8)$$

An approximate expression for the instantaneous acceleration of the droplets in the X-direction is used to determine the exposure time t of the droplets. The general expression for this acceleration is (see appendix B)

$$\frac{dV_{d,x}}{dt} = \frac{3\rho_m C_D}{8\rho_l r}\left(V_{m,x} - V_{d,x}\right)V \qquad (C9)$$

~~CONFIDENTIAL~~

The values of ρ_m, C_D, and r can here be assumed to be equal to their initial values. The relative velocity V between the droplets and the airstream is given approximately by

$$V = V_{m,x} - V_{d,x}$$

The constant pressure momentum relation (eq. (B6)) becomes

$$V_{m,x} = V_{m,x,1} + W^* V_{d,x,1} - W^* V_{d,x}$$

Substituting these results into equation (C9) and integrating twice over the droplet exposure time (with W^* assumed constant at an average value) gives the following relation between x and t:

$$\chi = \left(1 + W_{av}{}^* \frac{V_{d,x,1}}{V_{m,x,1}}\right)\tau - \ln\left[1 + \left(1 - \frac{V_{d,x,1}}{V_{m,x,1}}\right)\tau\right] \qquad (C10)$$

where

$$\chi = \left(1 + W_{av}{}^*\right)^2 \frac{3\rho_{m,1} C_{D,1}}{8\rho_l} \frac{x}{r_1}$$

$$\tau = \left(1 + W_{av}{}^*\right)\frac{3\rho_{m,1} C_{D,1}}{8\rho_l} \frac{V_{m,x,1} t}{r_1}$$

Equation (C10) is applicable for forward injection, that is, where $V_{d,x,1} \neq 0$. For the RAM B2 injection configuration it is assumed that $V_{d,x,1} = 0$ and equation (C10) reduces to

$$\chi = \tau - \ln(1 + \tau)$$

For the range of conditions of interest, this expression can be closely approximated by

$$\chi = a\tau^b \qquad (C11)$$

where $a = 0.313$ and $b = 1.74$. Substitution of t from equation (C11) into equation (C8) gives the following relation for $N_e/N_{e,1}$:

$$\frac{N_e}{N_{e,1}} = \exp\left[-\frac{3}{4a^{1/b}}\left(\frac{3C_{D,1}}{8}\right)^{(1-b)/b} \frac{\dot{m}_c}{\rho_{m,1} V_{m,1} A_{m,1}} \frac{V_{e,1}}{V_{m,1}}\left(1 + W_{av}{}^*\right)^{(2-b)/b}\left(\frac{\rho_{m,1} x}{\rho_l r_1}\right)^{1/b} \bar{f}_c\right] \qquad (C12)$$

where $W_{av}{}^*$ is obtained from equation (5) with Δy_{max} evaluated at an average value of x between the injection point and the antenna site. The value of $A_{m,1}$, however, is taken as the spray cross-sectional area at the injection site ($x = 0$). For this purpose a correlating equation for the spray penetration on a sphere-cone shape, similar to an equation in reference 18, has been obtained:

$$\frac{y_{max}}{d_0} = 1.56\bar{V}^{0.25}\left(\frac{x}{d_0} + 0.3\bar{V}^{0.5}\right)^{0.5}$$

This equation represents a reasonable compromise for injection of water and liquid nitrogen. In particular, the penetration predicted by this equation for $x = 0$ is in good agreement with wind-tunnel data of the type presented in reference 18. As in reference 11, the spray area is then computed as

$$A_m = \frac{\pi}{2}y_{max}^2$$

so that

$$A_{m,1} = 1.155d_0^2\bar{V}$$

Values of $A_{m,1}$ and other quantities required in equation (C12) are listed in table III. The values of $N_{e,1}$ are based on reflectometer measurements obtained during the RAM B3 flight (ref. 32).

REFERENCES

1. Dirsa, Edward F.: The Telemetry and Communication Problem of Re-Entrant Space Vehicles. Proc. IRE, vol. 48, no. 4, Apr. 1960, pp. 703-713.

2. Sisco, W.; and Fiskin, J. M.: Shock Ionization Changes EM Propagation Characteristics. Space/Aeron., vol. 31, no. 3, Mar. 1959, pp. 66-70.

3. Ginzburg, V. L. (Royer and Roger, trans.): Propagation of Electromagnetic Waves in Plasma. Gordon and Breach, Sci. Publ., Inc., c.1961.

4. Ellis, Macon C., Jr.; and Huber, Paul W.: Radio Transmission Through the Plasma Sheath Around a Lifting Reentry Vehicle. NASA TN D-507, 1961.

5. Huber, Paul W.; and Nelson, Clifford H.: Plasma Frequency and Radio Attenuation. Proceedings of the NASA-University Conference on the Science and Technology of Space Exploration, Vol. 2, NASA SP-11, 1962, pp. 347-360. (Also available as NASA SP-25.)

6. Evans, John S.; and Huber, Paul W.: Calculated Radio Attenuation Due to Plasma Sheath on Hypersonic Blunt-Nosed Cone. NASA TN D-2043, 1963.

7. Cuddihy, W. F.; and Hughes, J. Kenrick: Simulated Reentry Tests of a Method for Reducing Radio Blackout by Material Addition to Ionized Flow Field. NASA TM X-988, 1964.

8. Kuhns, Perry W.; and Cooper, Dale W.: Effect of Water Addition on Microwave Transmission Through a Cold Plasma Layer. NASA TM X-874, 1963.

9. Sims, Theo E.; and Jones, Robert F.: Rocket Exhaust Effects on Radio Frequency Propagation From a Scout Vehicle and Signal Recovery During the Injection of Decomposed Hydrogen Peroxide. NASA TM X-529, 1961.

10. Schroeder, Lyle C.: Gemini Reentry Communications Experiment. NASA paper presented at Third Symposium on the Plasma Sheath (Boston, Mass), Sept. 21-23, 1965.

11. Beckwith, Ivan E.; and Bushnell, Dennis M.: Depletion of Free Electrons by Water Injection Into the Flow Fields of Hypersonic Vehicles. NASA paper presented at Third Symposium on the Plasma Sheath (Boston, Mass.), Sept. 21-23, 1965.

12. Wood, A. D.; Springfield, J. F.; and Pallone, A. J.: Determination of the Effects of Chemical and Vibrational Relaxation on an Inviscid Hypersonic Flow Field. RAD-TM-63-88 (Contract AF04(694)-239), AVCO Corp., Jan. 1964.

13. Blottner, F. G.: Non-Equilibrium Laminar Boundary Layer Flow of Ionized Air. AIAA Preprint No. 64-41, Jan. 1964.

14. Pallone, Adrian J.; Moore, Jeffrey A.; and Erdos, John I.: Nonequilibrium, Nonsimilar Solutions of the Laminar Boundary-Layer Equations. AIAA J., vol. 2, no. 10, Oct. 1964, pp. 1706-1713.

15. Spencer, Dwain F.: An Evaluation of the Communication Blackout Problem for a Blunt Mars-Entry Capsule and a Potential Method for the Elimination of Blackout. Tech. Rept. No. 32-594 (Contract No. NAS 7-100), Jet Propulsion Lab., C.I.T., Apr. 15, 1964.

16. Evans, John S.: Charge Recombination on Water Droplets in a Plasma. NASA TM X-1186, 1965.

17. Kurzius, S. C.; and Ellison, R.: Effects of Water Droplets on Re-Entry Plasma Sheaths. TP-123 (Contract NAS1-4418), AeroChem Res. Labs., Inc., Nov. 1965.

18. Beckwith, Ivan E.; and Huffman, Jarrett K.: Injection and Distribution of Liquids in the Flow Fields of Blunt Shapes at Hypersonic Speeds. NASA TM X-989, 1964.

19. Huber, Paul W.; and Evans, John S.: Theoretical Shock-Layer Plasma Flow Properties for the Slender Probe and Comparison With the Flight Results. NASA paper presented at the Second Symposium on the Plasma Sheath (Boston, Mass.), Apr. 10-12, 1962.

20. Brummer, E. E.; and Harrington, R. F.: A Unique Approach to an X-Band Telemetry Receiving System. Proc. 1962 Nat. Telemetering Conf., Vol. 1, May 1962. (Sponsored by Am. Rocket Soc., Am. Inst. Elec. Engr., Inst. Aerospace Sci., Instr. Soc. Am., Inst. Radio Eng.)

21. Brummer, E. A.: X-Band Telemetry Systems for Reentry Research. Paper No. CP 63-663, Inst. Elec. Electron. Engr., Apr. 1963.

22. Falanga, Ralph A.; Hinson, William F.; and Crawford, Davis H.: Exploratory Tests of the Effects of Jet Plumes on the Flow Over Cone-Cylinder-Flare Bodies. NASA TN D-1000, 1962.

23. Hinson, William F.; and Falanga, Ralph A.: Effect of Jet Pluming on the Static Stability of Cone-Cylinder-Flare Configurations at a Mach Number of 9.65. NASA TN D-1352, 1962.

24. McIver, Duncan E., Jr.: Radio-Frequency Signal Attenuation by Plasmas of Rocket Exhaust Gases. A Compilation of Recent Research Related to the Apollo Mission. NASA TM X-890, 1963, pp. 135-144.

25. Levine, Jack: Performance and Some Design Aspects of the Four-Stage Solid-Propellant Rocket Vehicle Used in the RAM A1 Flight Test. NASA TN D-1611, 1963.

26. Sims, Theo E.; and Jones, Robert F.:   Flight Measurements of VHF Signal Attenuation and Antenna Impedance for the RAM A1 Slender Probe at Velocities up to 17,800 Feet Per Second.   NASA TM X-760, 1963.

27. Swift, Calvin T.; and Evans, John S.:   Generalized Treatment of Plane Electromagnetic Waves Passing Through an Isotropic Inhomogeneous Plasma Slab at Arbitrary Angles of Incidence.   NASA TR R-172, 1963.

28. Carter, Howard S; and Wright, Robert L.:   Heat Transfer to a Hemispherically Blunted 9° Half-Angle Cone During Free Flight at Mach Numbers up to 20.8. NASA TM X-908, 1963.

29. Russo, F. P.; and Hughes, J. K.:   Measurements of the Effects of Static Magnetic Fields on VHF Transmission in Ionized Flow Fields.   NASA TM X-907, 1964.

30. Cuddihy, William F.; Beckwith, Ivan E.; and Schroeder, Lyle C.:   RAM B2 Flight Test of a Method for Reducing Radio Attenuation During Hypersonic Reentry. NASA TM X-902, 1963.

31. Raper, James L.; Keynton, Robert J.; and Woodbury, Gerard E.:   Detailed Description and Flight Performance of the RAM B Vehicle.   NASA TN D-2437, 1964.

32. Grantham, William L.:   Preliminary Analysis of Plasma-Sheath Electron Density Measurements at Entry Velocities.   NASA TM X-1035, 1964.

33. Ball, W. H.:   Flow Field Prediction and Analysis Study for Project RAM B3. SID 65-1113 (Contract No. NAS1-4743), North Am. Aviation, Inc., Aug. 20, 1965.

34. Mechtly, E. A.:   The International System of Units − Physical Constants and Conversion Factors.   NASA SP-7012, 1964.

35. Russo, Francis P.; and Campbell, Thomas G.:   Antenna Response to a Plasma Environment.   Proceedings of the NASA Conference on Communicating Through Plasmas of Atmospheric Entry and Rocket Exhaust.   NASA SP-52, 1964, pp. 33-44.

36. McIver, Duncan E., Jr.:   The Radio-Frequency Signal Attenuation Problem of Rocket Exhausts.   Proceedings of the NASA Conference on Communicating Through Plasmas of Atmospheric Entry and Rocket Exhaust.   NASA SP-52, 1964, pp. 167-179.

37. Cresci, Robert J.; and Libby, Paul A.:   The Downstream Influence of Mass Transfer at the Nose of a Slender Cone.   PIBAL Rept. No. 634 (WADD Tech. Rept. 60-892), Polytech. Inst. Brooklyn, May 1961.

38. FitzGibbon, Sheila A.:   Real Gas Supersonic Flow Field Solutions in the Shock Layer Around a 9° Sphere-Cone at Mach = 20.4, 21.4, and 21.2.   Aerodyn. Data Mem. No. 1:48, Missile and Space Vehicle Dept., Gen. Elec. Co., May 1961.

39. Storer, E. M.: Summary of Shock Shapes for Sphere Cones as Determined by Flow Field Solutions. Aerodyn. Data Memo No. 1:51, Missile and Space Vehicle Dept., Gen. Elec. Co., June 1961.

40. Beckwith, Ivan E.; and Bushnell, Dennis M.: Effect of Intermittent Water Injection on Aerodynamic Heating of a Sphere-Cone at Flight Velocities to 18 000 Feet Per Second. NASA TM X-1128, 1965.

41. Zeleznik, Frank J.; and Gordon, Sanford: A General IBM 704 or 7090 Computer Program for Computation of Chemical Equilibrium Compositions, Rocket Performance, and Chapman-Jouguet Detonations. NASA TN D-1454, 1962.

42. Ingebo, Robert D.; and Foster, Hampton H.: Drop-Size Distribution for Crosscurrent Breakup of Liquid Jets in Airstreams. NACA TN 4087, 1957.

43. Beckwith, Ivan E.; Bushnell, Dennis M.; and Huffman, Jarrett K.: Investigation of Water Injection on Models of Gemini Vehicle and Resulting Predictions for GT-3 Reentry Communications Experiment. NASA TM X-1200, 1966.

44. Shapiro, A. H.; Wadleigh, K. R.; Gavril, B. D.; and Fowle, A. A.: The Aerothermopressor — A Device for Improving the Performance of a Gas-Turbine Power Plant. Trans. ASME, vol. 78, no. 3, Apr. 1956, pp. 617-653.

45. Masson, David J.; Morris, Deane N.; and Bloxom, Daniel E.: Measurements of Sphere Drag From Hypersonic Continuum to Free-Molecule Flow. Rarefied Gas Dynamics, L. Talbot, ed., Acedemic Press, Inc. (New York), 1961, pp. 643-661.

46. Aroesty, Jerome: Sphere Drag in a Low Density Supersonic Flow. Rept. No. HE-150-192 (Contract N-onr-222(45)), Inst. Eng. Res., Univ. of California, Jan. 3, 1962.

47. Sreekanth, A. K.: Drag Measurements on Circular Cylinders and Spheres in the Transition Regime at a Mach Number of 2. Rept. No. 74, Inst. Aerophys., Univ. of Toronto, Apr. 1961.

48. Ashkenas, Harry: Low-Density Sphere Drag With Equilibrium and Nonequilibrium Wall Temperature. Rarefied Gas Dynamics, Vol. II, J. A. Laurmann, ed., Academic Press, 1963, pp. 278-290.

49. May, Albert; and Witt, W. R., Jr.: Free-Flight Determinations of the Drag Coefficients of Spheres. J. Aeron. Sci., vol. 20, no. 9, Sept. 1953, pp. 635-638.

50. Hodges, A. J.: The Drag Coefficient of Very High Velocity Spheres. J. Aeron. Sci., vol. 24, no. 10, Oct. 1957, pp. 755-758.

51. Emmons, Howard W., ed.: Fundamentals of Gas Dynamics. Vol. III of High Speed Aerodynamics and Jet Propulsion. Princeton Univ. Press, c.1958.

52. Charters, A. C.; and Thomas, R. N.:   The Aerodynamic Performance of Small Spheres From Subsonic to High Supersonic Velocities.   J. Aeron. Sci., vol. 12, no. 4, Oct. 1945, pp. 468-476.

53. Rouse, Hunter: Elementary Mechanics of Fluids.   John Wiley & Sons, Inc., c.1946, p. 245.

54. Barnett, Henry C.; and Hibbard, Robert R., eds.:   Basic Considerations in the Combustion of Hydrocarbon Fuels With Air.   NACA Rept. 1300, 1957.

55. Brokaw, Richard S.:   Alignment Charts for Transport Properties Viscosity, Thermal Conductivity, and Diffusion Coefficients for Nonpolar Gases and Gas Mixtures at Low Density.   NASA TR R-81, 1961.

56. Svehla, Roger A.:   Estimated Viscosities and Thermal Conductivities of Gases at High Temperatures.   NASA TR R-132, 1962.

57. Fano, Lilla; Hubbell, John H.; and Beckett, Charles W.:   Compressibility Factor, Density, Specific Heat, Enthalpy, Entropy, Free-Energy Function, Viscosity, and Thermal Conductivity of Steam.   NACA TN 3273, 1956.

58. Reid, Robert C.; and Sherwood, Thomas K.:   The Properties of Gases and Liquids. McGraw-Hill Book Co., Inc., 1958, p. 226.

TABLE I.- RECEIVING SYSTEMS FOR RAM B2 MISSION

Location	Receiver frequency, Mc	Receiver bandwidth, kc	Antenna polarization (a)	Antenna gain, dB	Figure of signal-strength plot
Wallops					
Fixed-1	244.3	300	RCP	28	
Fixed-2	244.3	300	LCP	18	
Mobile	244.3	300	RCP	10	15
Mobile	244.3	16	RCP	10	
Mobile	244.3	16	LCP	10	
Fixed-1	225.7	300	RCP	28	15
Fixed-2	225.7	300	LCP	18	
Mobile	225.7	300	RCP	10	
Mobile	30.8	8	Linear	10	15
FPS-16	5690		Circular	43	20
X-band	9210		RCP	36	
Langley					
	244.3	300	RCP	10	
	244.3	16	RCP	10	16
	244.3	16	LCP	10	
	225.7	300	RCP	10	16
	30.8	8	Linear	10	16
Coquina					
	244.3	300	RCP	10	
	244.3	16	RCP	10	
	244.3	16	LCP	10	17
	225.7	300	RCP	10	17
	30.8	8	Linear	10	17
	9210		RCP	36	21
Range recoverer					
	244.3	300	RCP	18	18
	225.7	300	LCP	10	18
Bermuda					
Town Hill	244.3	300	RCP	18	
Town Hill	244.3	300	LCP	18	
Coopers I.	244.3	300	RCP	18	19
Town Hill	225.7	300	RCP	18	
Town Hill	225.7	300	LCP	18	19
Coopers I.	225.7	300	LCP	18	
Coopers I.	30.8		Linear	2	
FPS-16	5690		Circular	43	
X-band	9210		RCP	36	

[a]The abbreviation RCP means right circular polarization, and LCP means left circular polarization.

TABLE II.- SAMPLE CALCULATIONS FOR ADJUSTED

RECOVERY SIGNAL LEVEL AND W^*

[Coquina Station; 244.3 Mc; figure 14(b)]

Status of system	Time, sec	Signal level, -dB	Free space signal level, -dB	Adjusted signal level, -dB	Flow rate		W^*
					lbm/sec	kg/sec	
Pre-attenuation	100.2	15	15	0	0	0	0
Pre-injection	109.7	32		17	0	0	0
No injection	112.2	35		20	0	0	0
Stagnation injection	114.0	14	14	0			
No injection	114.9	36		22	0	0	0
Side injection	115.6	22		8	.20	.09	.108
Cycle 2	115.9	20		6	.35	.16	.19
	116.2	18.5		4.5	.52	.23	.27
	116.5	17		3	.65	.29	.35
	116.9	16		2	.82	.37	.455
	117.2	15		1	.94	.42	.515
	117.4	15		1	1.05	.47	.57
No injection	118.3	44			0	0	0
Stagnation injection	120.0	15	15	0			
No injection	121.3	>50		>35	0	0	0
Side injection	121.7	26		11	.17	.08	.112
Cycle 3	122.0	22.5		7.5	.30	.13	.196
	122.3	19.5		4.5	.45	.20	.295
	122.6	18.5		3.5	.55	.25	.36
	122.9	18.25		3.25	.70	.31	.46
	123.3	18.25		3.25	.80	.36	.525
	123.5	19.0		4.0	.93	.42	.61
No injection	124.4	>50		>35	0	0	0
Stagnation injection	126.5	18	18	0			

TABLE III.- VALUES USED TO COMPUTE VARIATION OF $\bar{f}_c$ FOR FIGURE 31

	115 sec	145 sec	165 sec
Trajectory time	115 sec	145 sec	165 sec
Altitude	157 000 ft (47.8 km)	210 000 ft (64.0 km)	235 000 ft (71.6 km)
V_∞	16 900 ft/sec	17 650 ft/sec	17 500 ft/sec
	(5.2 km/sec)	(5.4 km/sec)	(5.3 km/sec)
r_1	2.21×10^{-5} ft	3.45×10^{-5} ft	4.54×10^{-5} ft
	(6.7 microns)	(10.7 microns)	(13.8 microns)
$\rho_{m,1}$	9.39×10^{-5} lbm/ft^3	1.44×10^{-5} lbm/ft^3	0.542×10^{-5} lbm/ft^3
	(1.5×10^{-3} kg/m^3)	(2.3×10^{-4} kg/m^3)	(8.6×10^{-5} kg/m^3)
$C_{D,1}$	2.52	2.54	2.59
T_1	7290° R (4050° K)	7480° R (4160° K)	7370° R (4090° K)
$V_{m,1}$	10 100 ft/sec	10 400 ft/sec	10 000 ft/sec
	(3.1 km/sec)	(3.2 km/sec)	(3.0 km/sec)
W_{av}^* (for x = 0.4 ft (0.1 m))	0.20	0.30	0.55
$A_{m,1}$	0.0066 ft^2 (0.0006 m^2)	0.028 ft^2 (0.003 m^2)	0.054 ft^2 (0.005 m^2)
$N_{e,1}$	7.6×10^{11} e/cm^3	2.5×10^{11} e/cm^3	2.0×10^{11} e/cm^3
$\dot{m}_c$ per side (minimum)	0.1 lbm/sec	0.06 lbm/sec	0.04 lbm/sec
	(0.05 kg/sec)	(0.03 kg/sec)	(0.02 kg/sec)

TABLE IV.- PARAMETERS IN DROPLET

DRAG COEFFICIENT EXPRESSION

M	$C_{D,C}$	$C_{D,FM}$	A	n
0.5	0.520	7.80	0.315	0.410
.6	.551	6.50	.240	.460
.7	.586	5.57	.182	.500
.8	.625	4.92	.141	.545
.9	.666	4.45	.110	.590
1.0	.712	4.10	.090	.620
1.2	.801	3.60	.065	.670
1.4	.880	3.23	.055	.690
1.6	.929	2.98	.049	.710
1.8	.955	2.80	.047	.715
2.0	.971	2.68	.046	.720
2.4	.981	2.48	.0455	.725
2.8	.969	2.36	.0455	.725
3.2	.949	2.28	.0453	.730
4	.919	2.17	.0452	.730
5	.910	2.10	.0451	.735
6	.910	2.05	.0449	.735
8	.910	2.02	.0448	.740
10	.910	2.00	.0447	.745
12	.910	2.00	.0447	.745
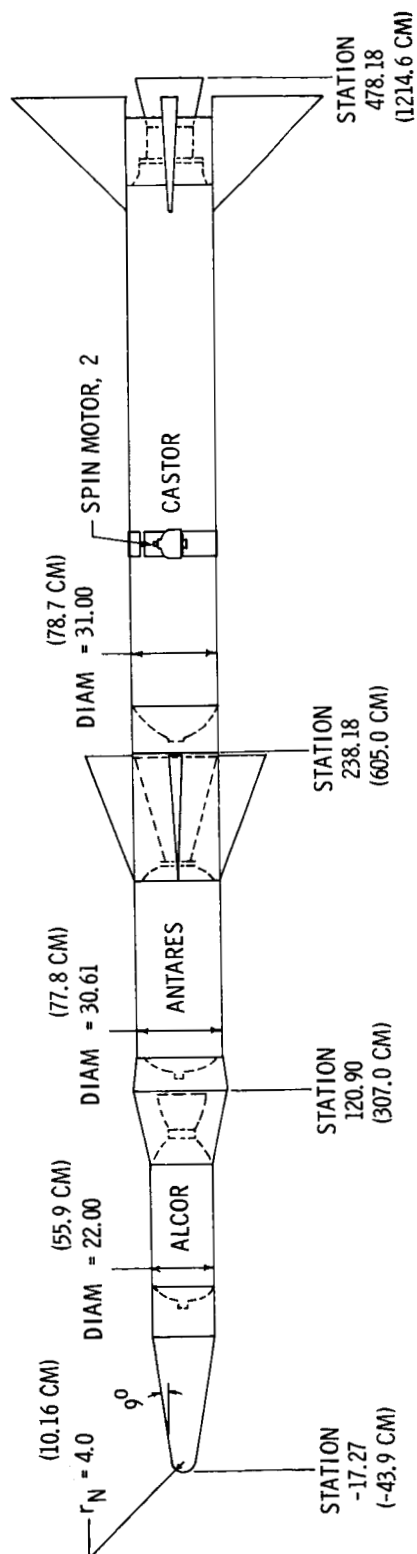
Figure 1.- Launch vehicle. All dimensions are in inches (centimeters).
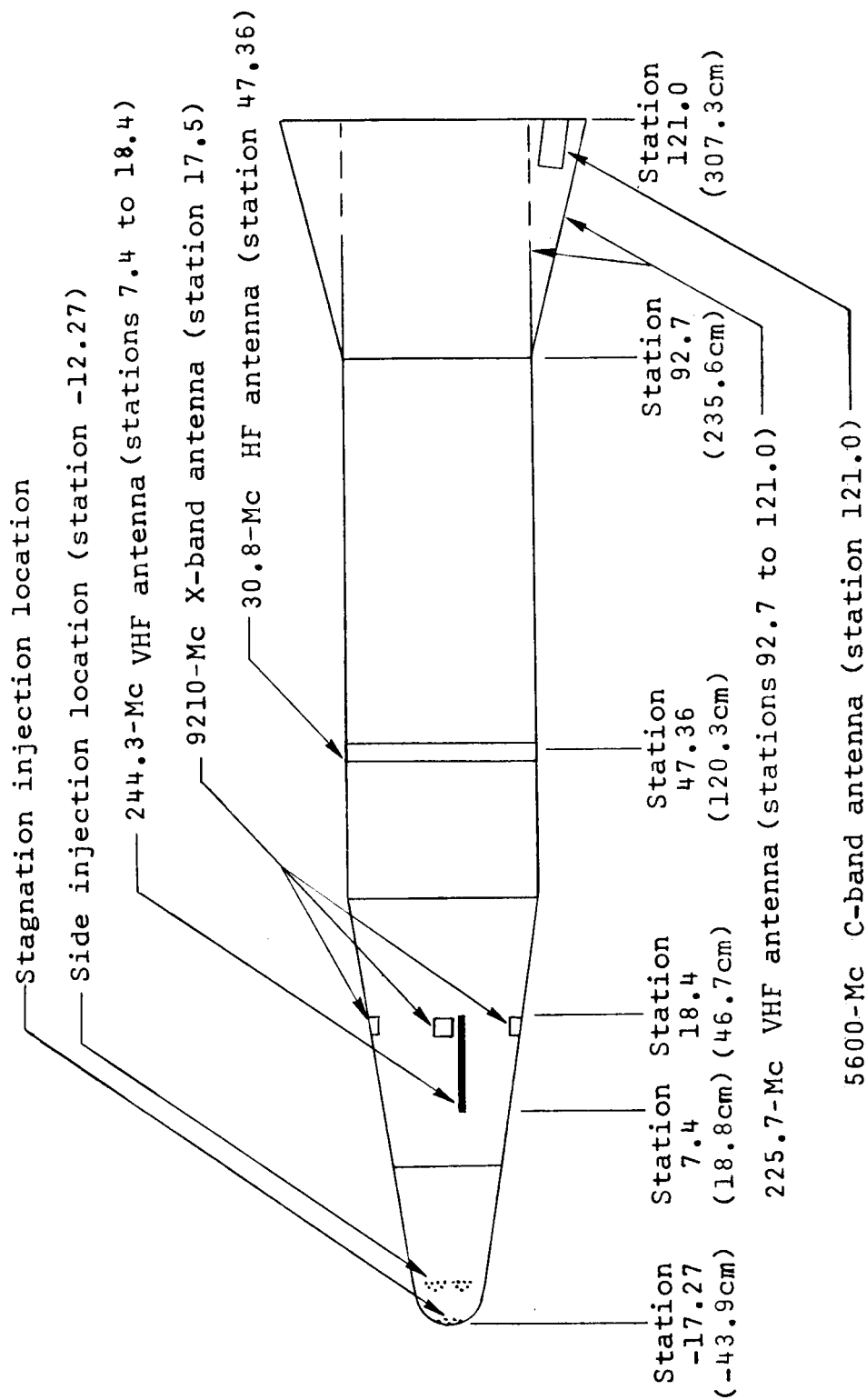
Figure 2.- Test vehicle. All dimensions are in inches (centimeters).

Stagnation injection location

Side injection location (station -12.27)

244.3-Mc VHF antenna (stations 7.4 to 18.4)

9210-Mc X-band antenna (station 17.5)

30.8-Mc HF antenna (station 47.36)

Station 121.0 (307.3cm)

Station 92.7 (235.6cm)

Station 47.36 (120.3cm)

225.7-Mc VHF antenna (stations 92.7 to 121.0)

5600-Mc C-band antenna (station 121.0)

Station 18.4 (46.7cm)

Station 7.4 (18.8cm)

Station -17.27 (-43.9cm)

72
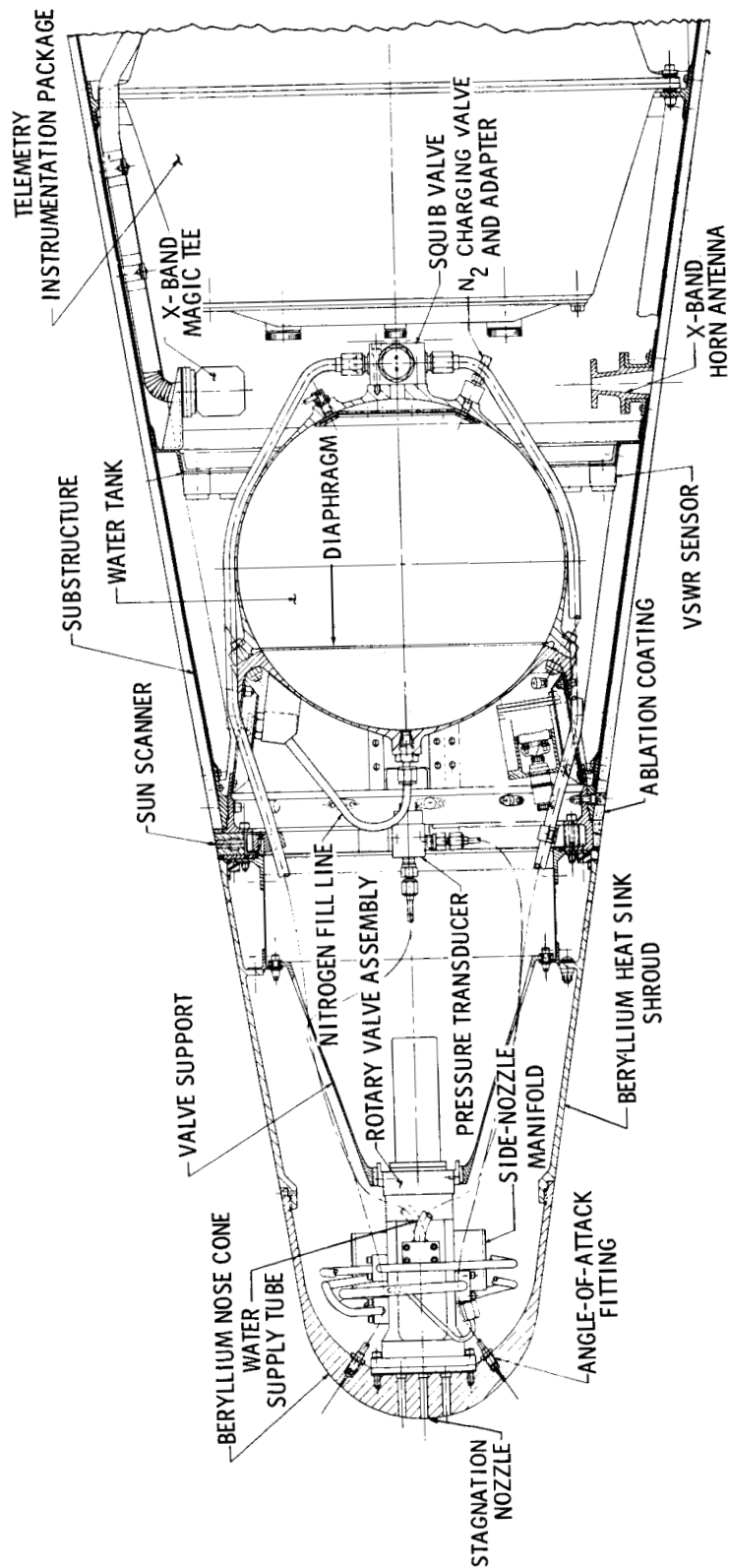
Figure 3.- Internal arrangement of equipment in nose portion of test vehicle.

73
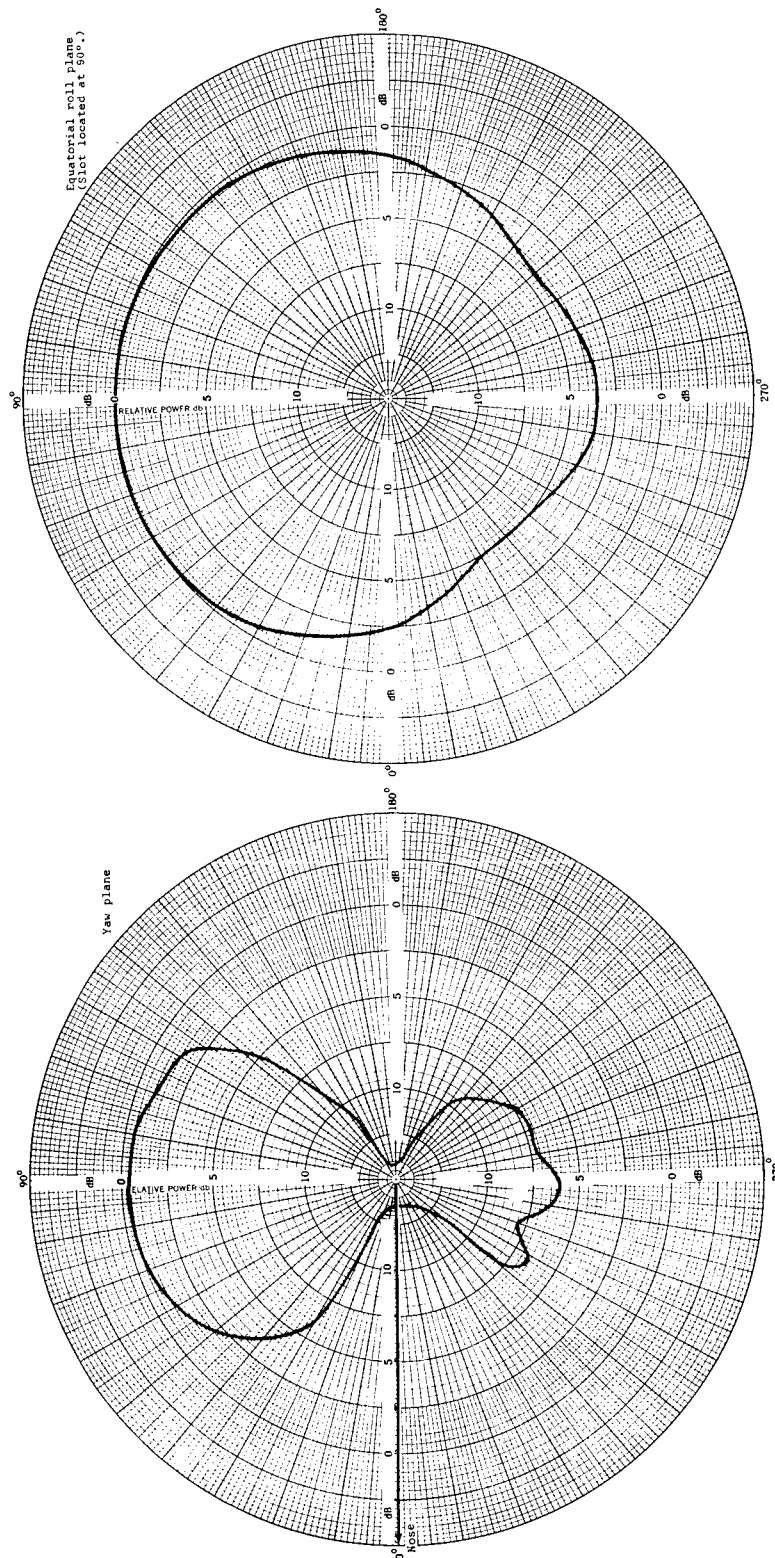
(a) Patterns for 244.3-Mc antenna.

Figure 4.- Antenna patterns.
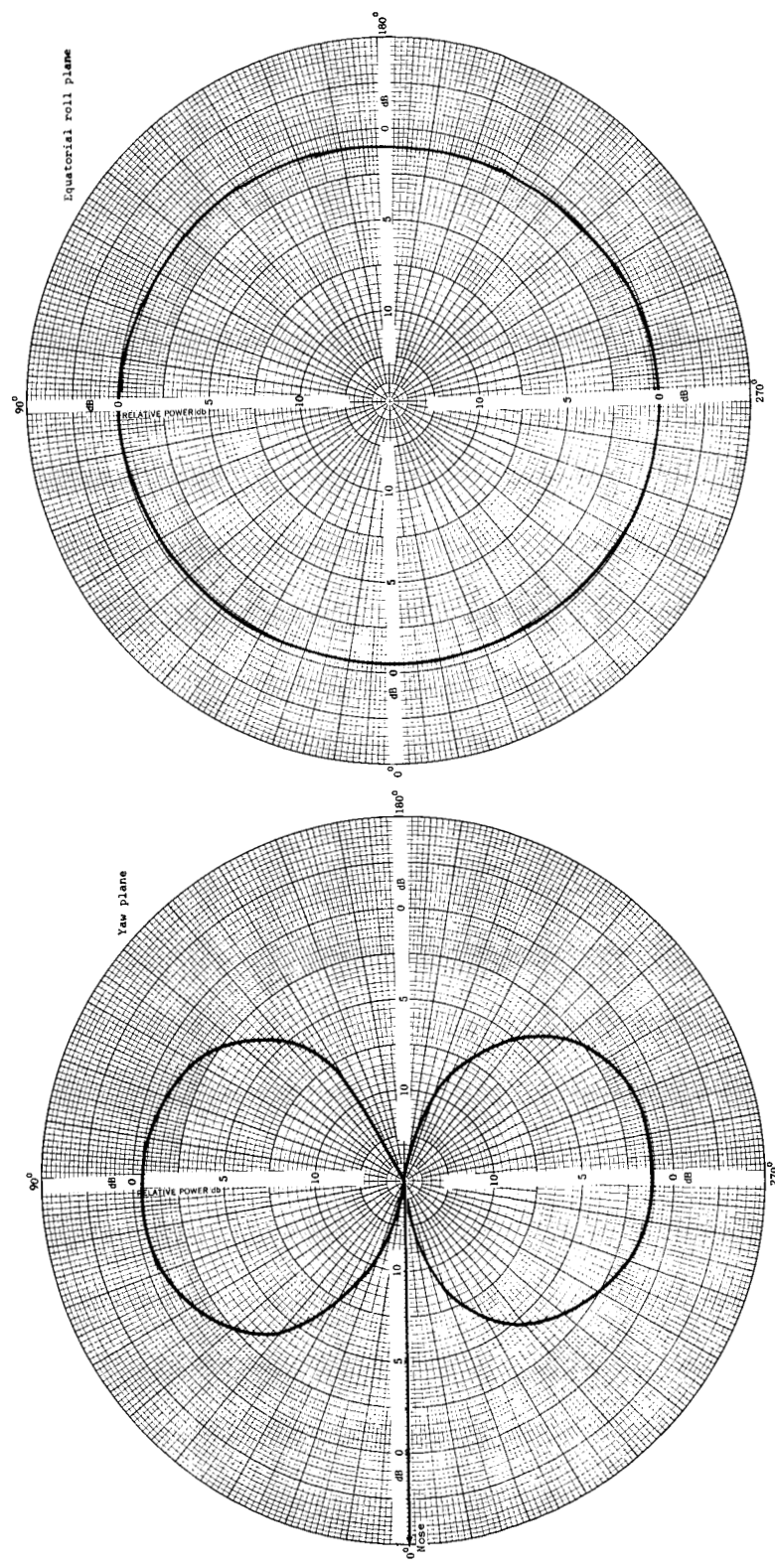
(b) Patterns for 30.8-Mc antenna.

Figure 4.- Continued.
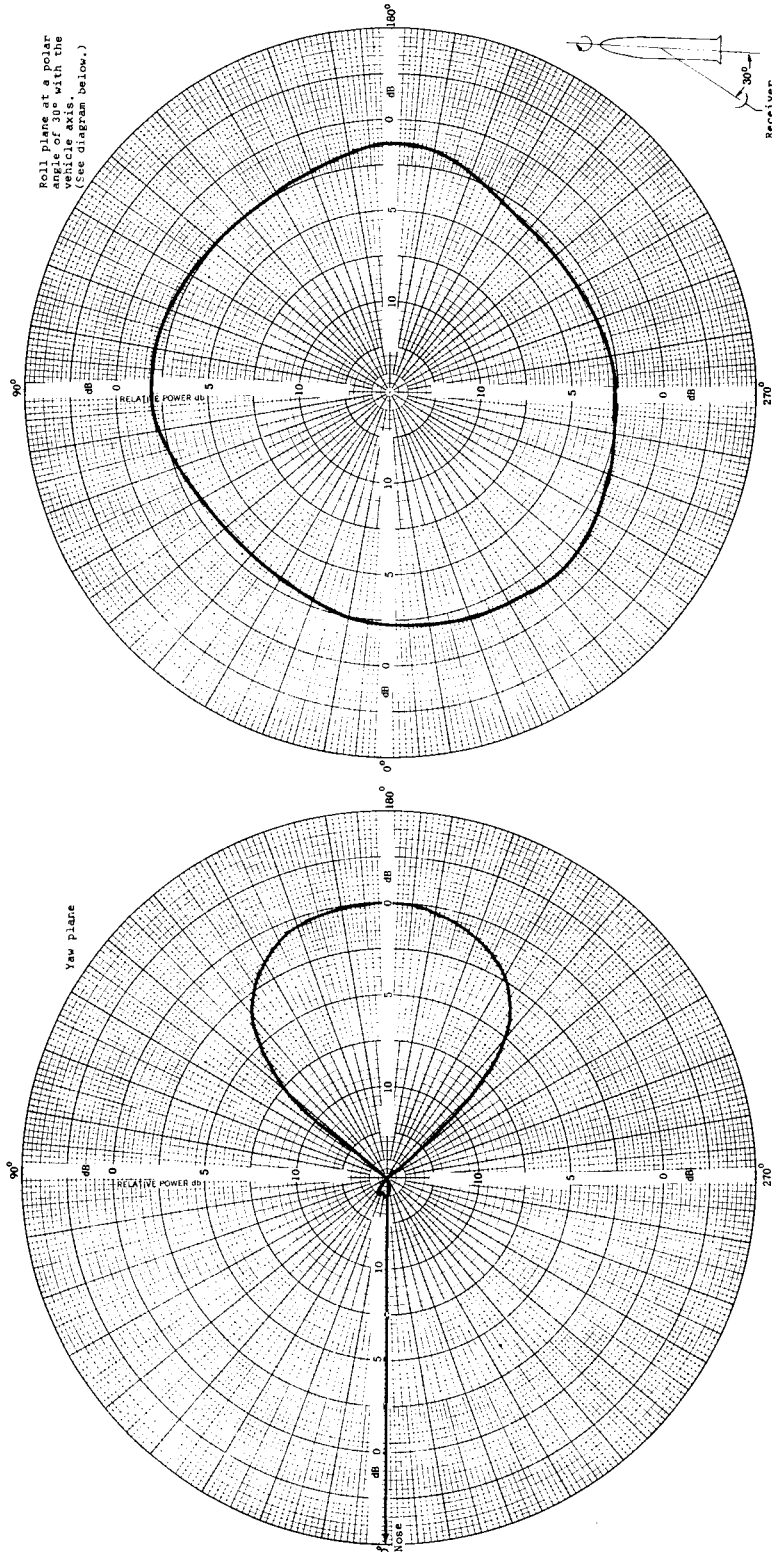
(c) Patterns for 225.7-Mc antenna.

Figure 4.- Concluded.
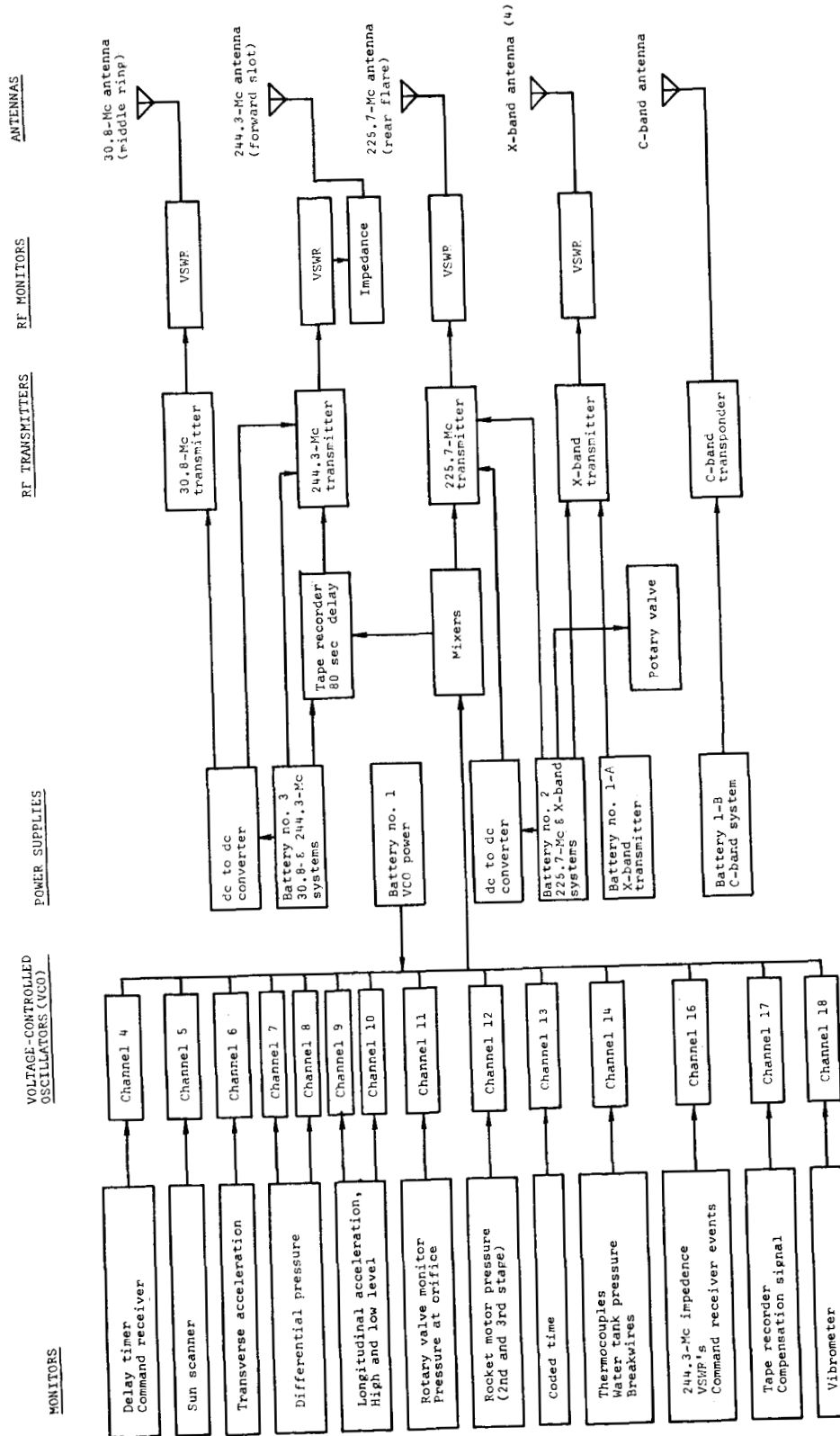
Figure 5.- Block diagram of telemetry system.

77
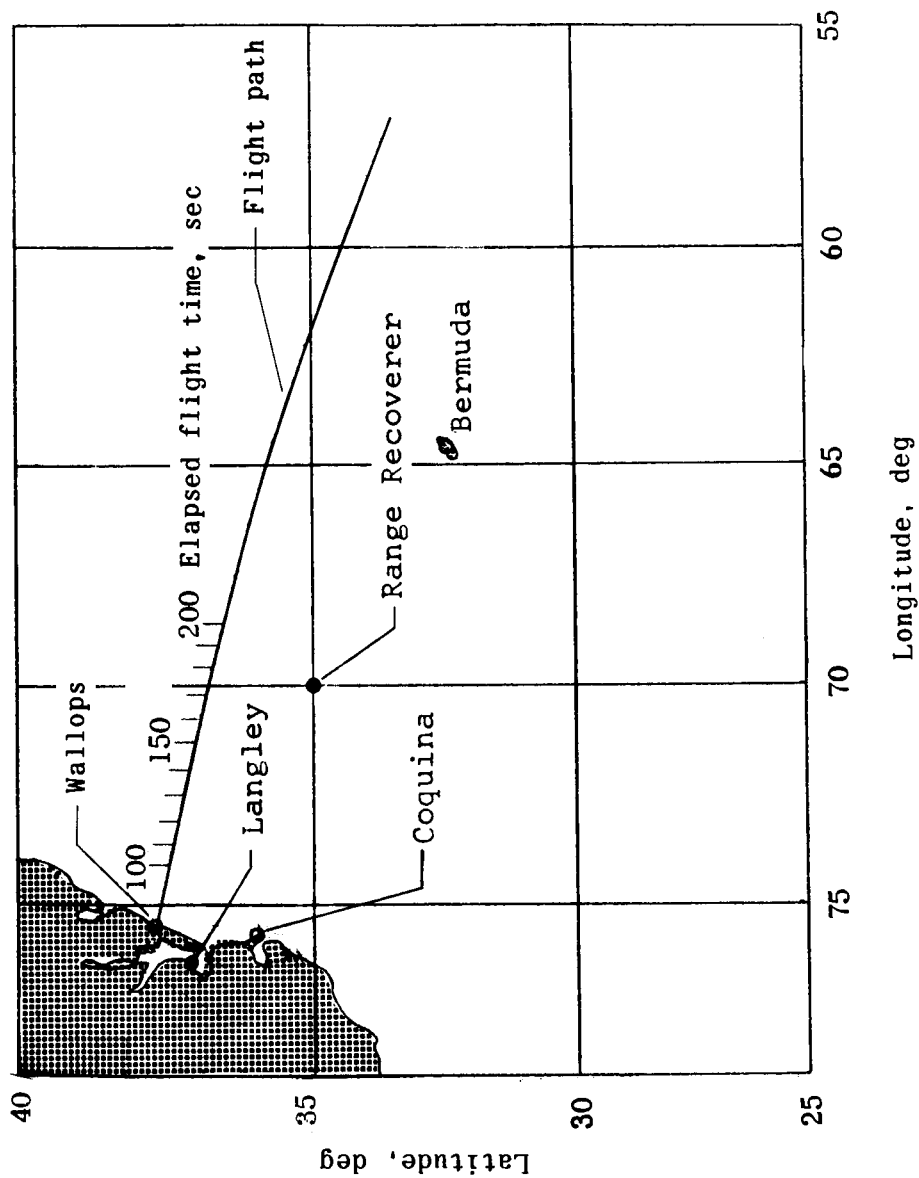
Figure 6.- Range stations and ground track.
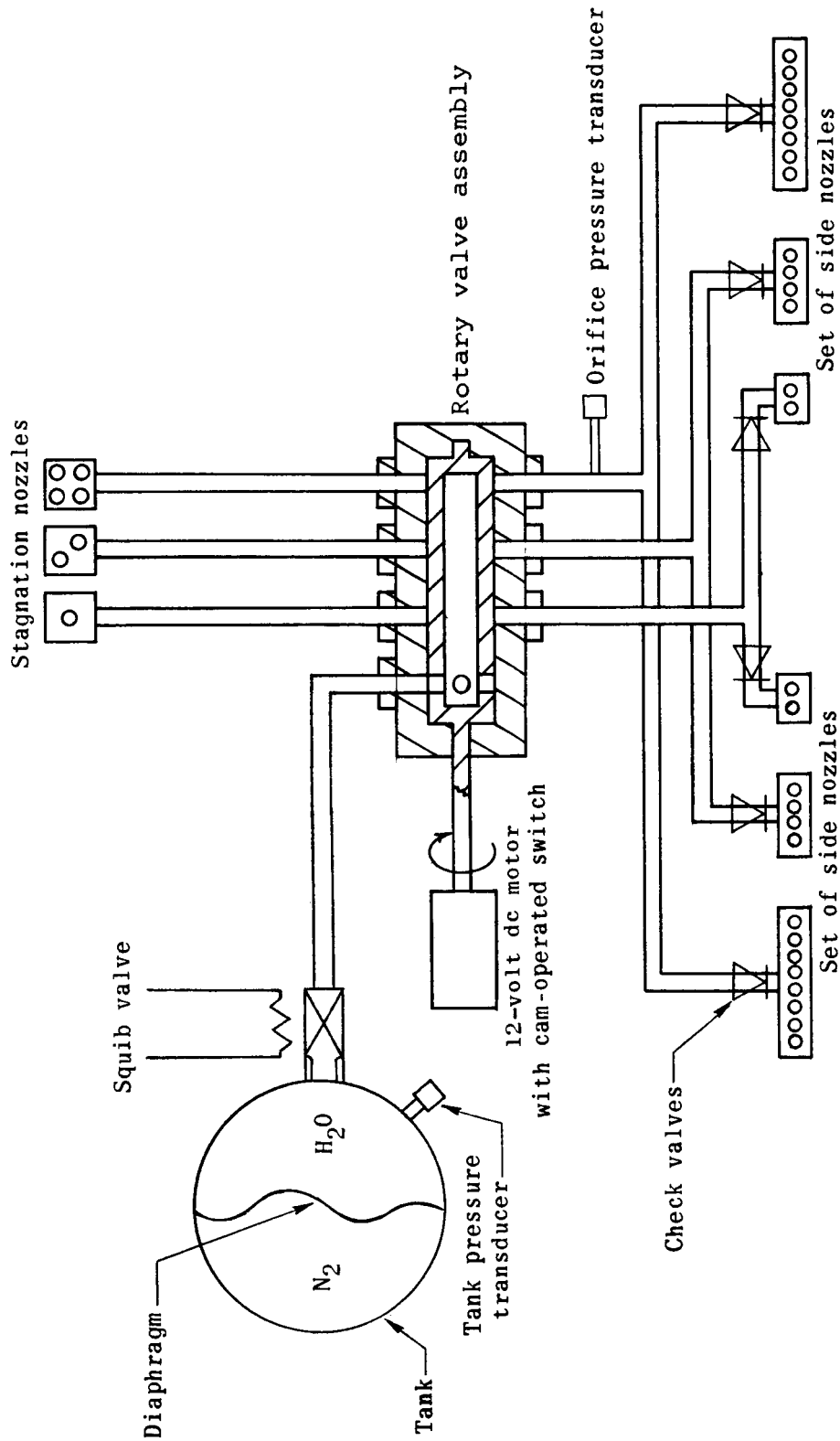
Figure 7.- Schematic layout of water injection system.
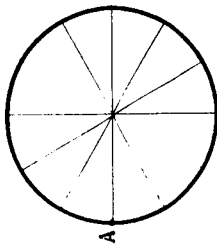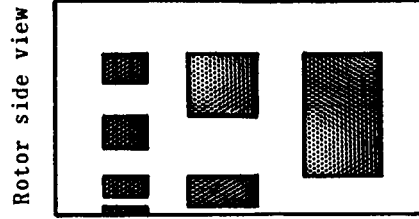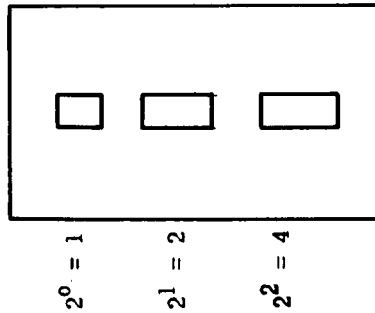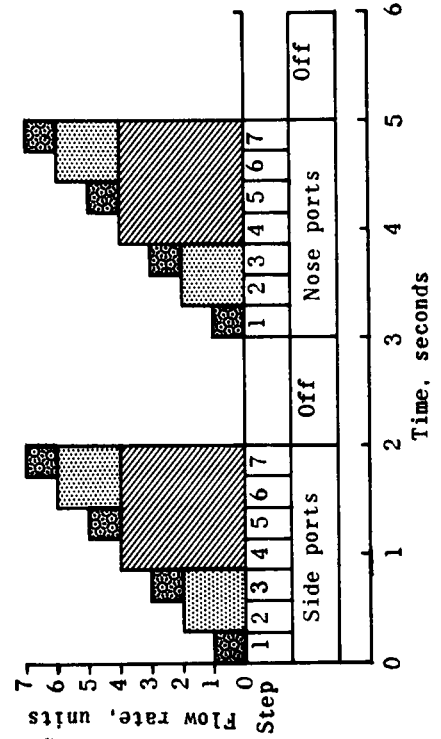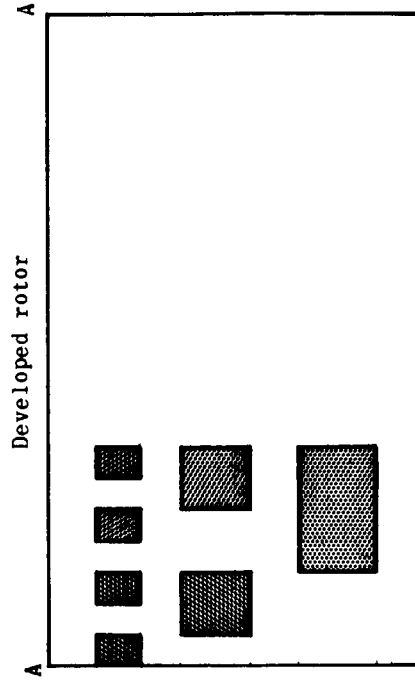
Figure 8.- Arrangement of ports in rotary valve and resulting idealized injection flow.
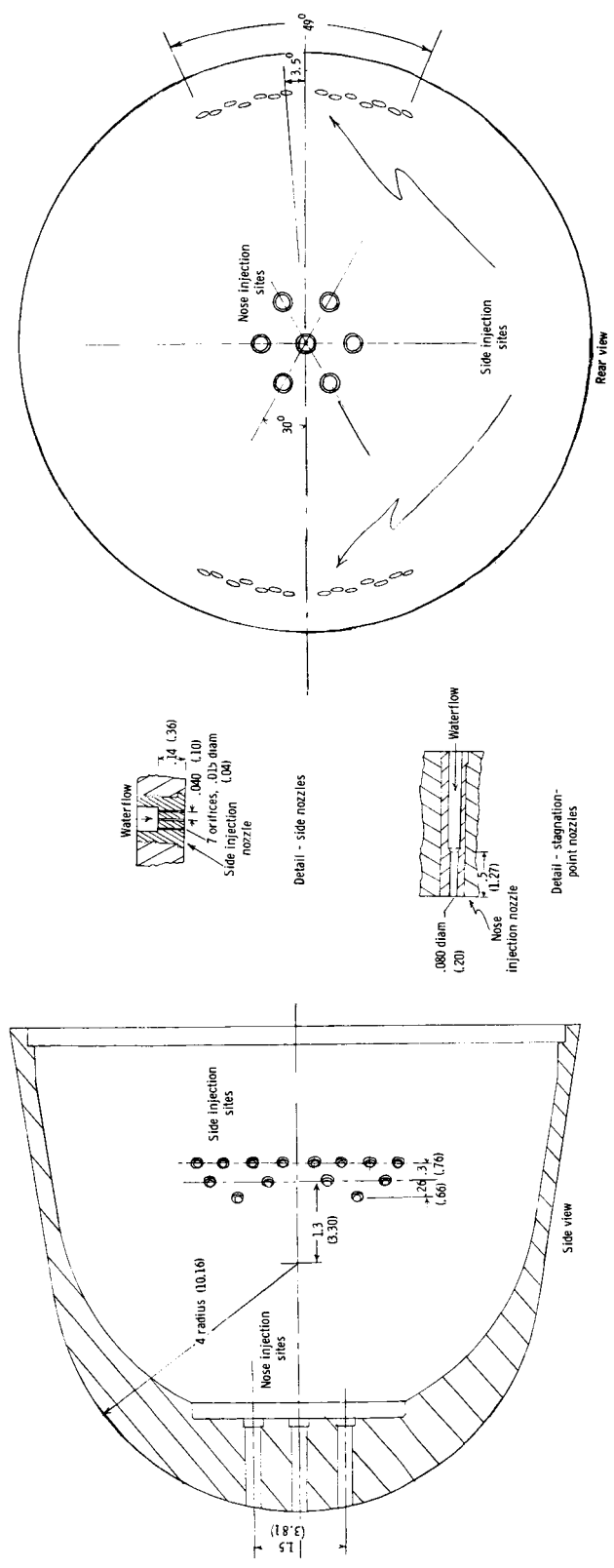
Figure 9.- Location and arrangement of side and stagnation injection sites and details of injection nozzles. All dimensions are in inches (centimeters).

81
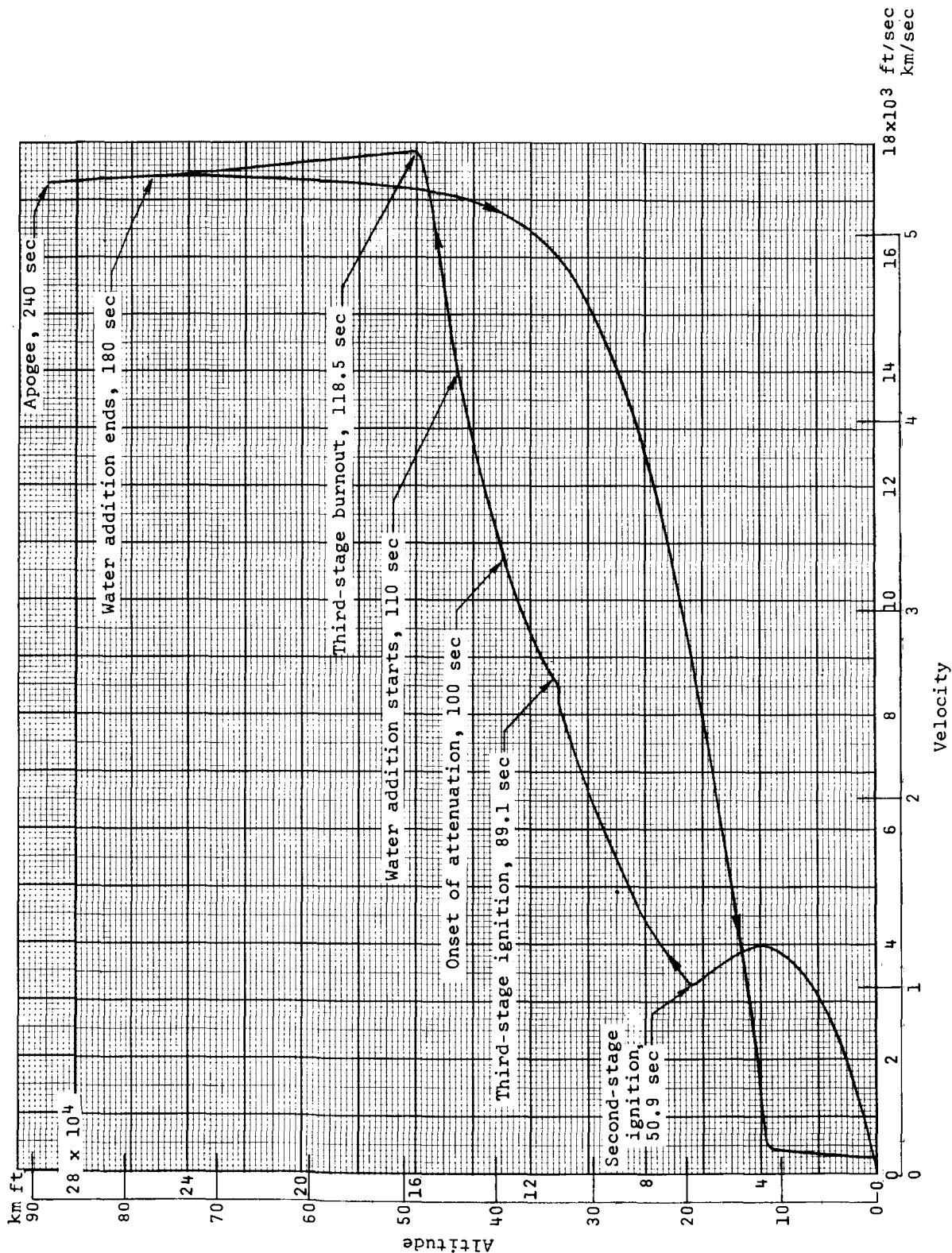
(a) Altitude plotted as a function of velocity.

Figure 10.- Trajectory parameters.
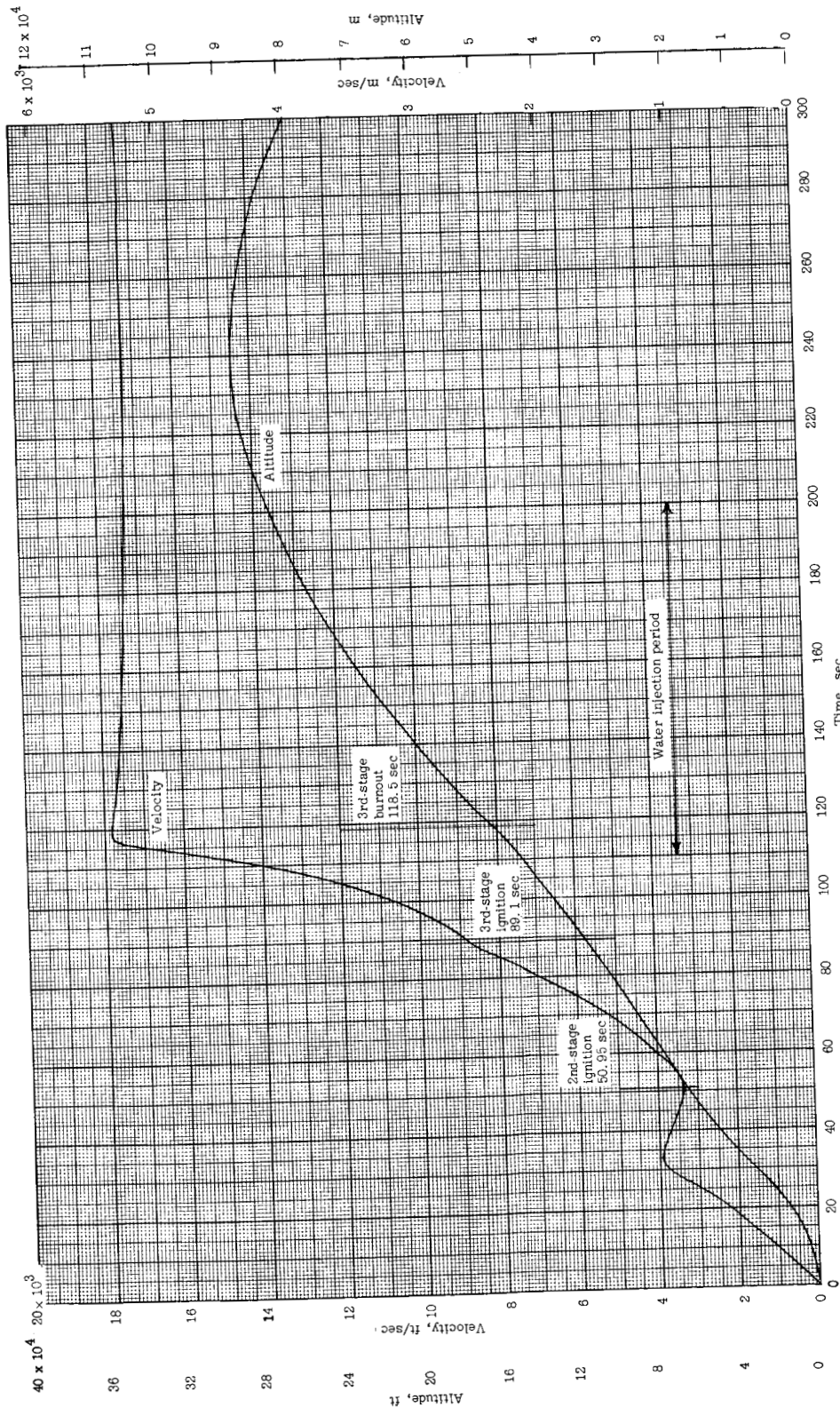
(b) Altitude and velocity plotted as a function of time.

Figure 10.- Concluded.
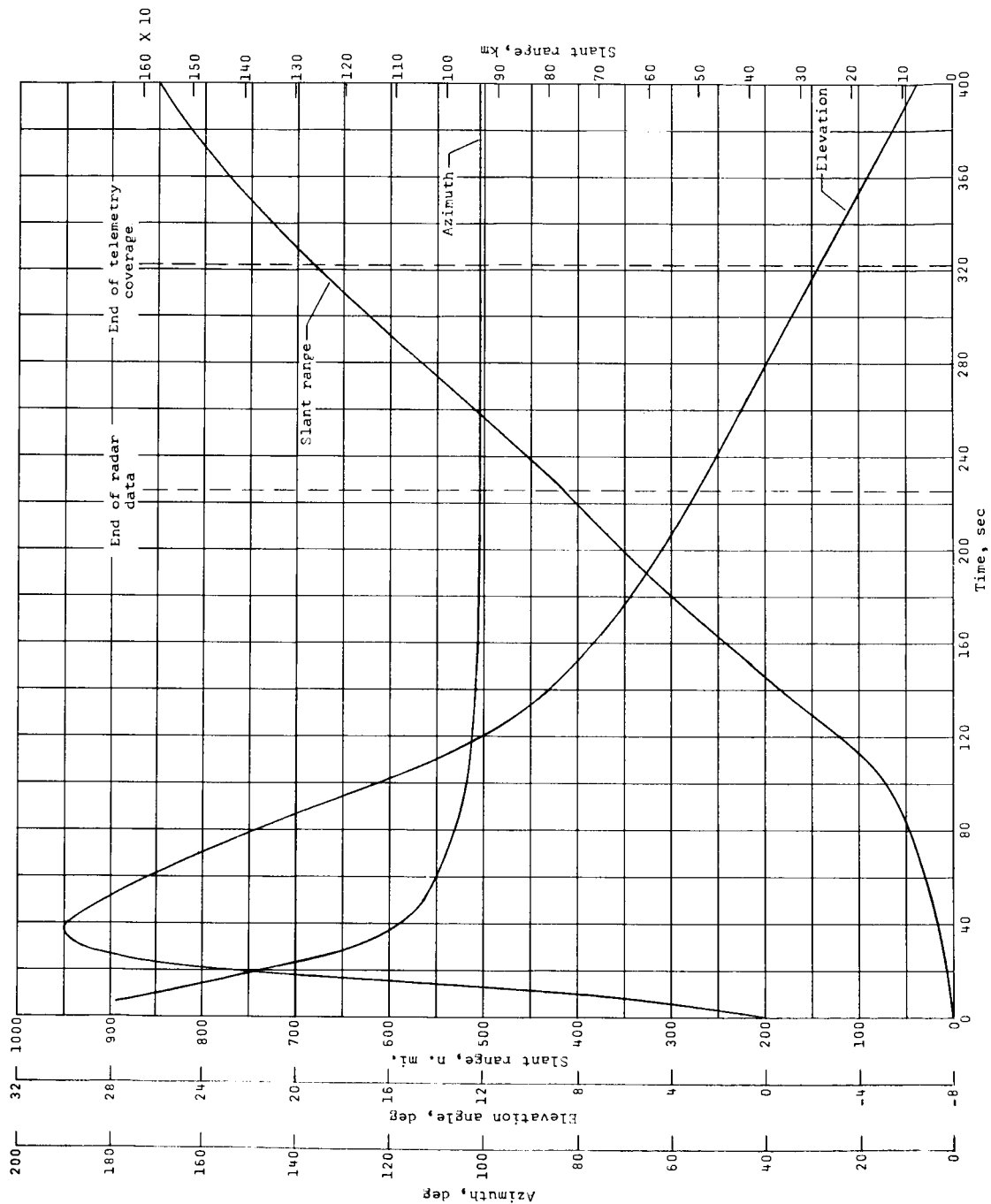
(a) Wallops Station.

Figure 11.- Azimuth, elevation, and slant range for RAM B2 flight.
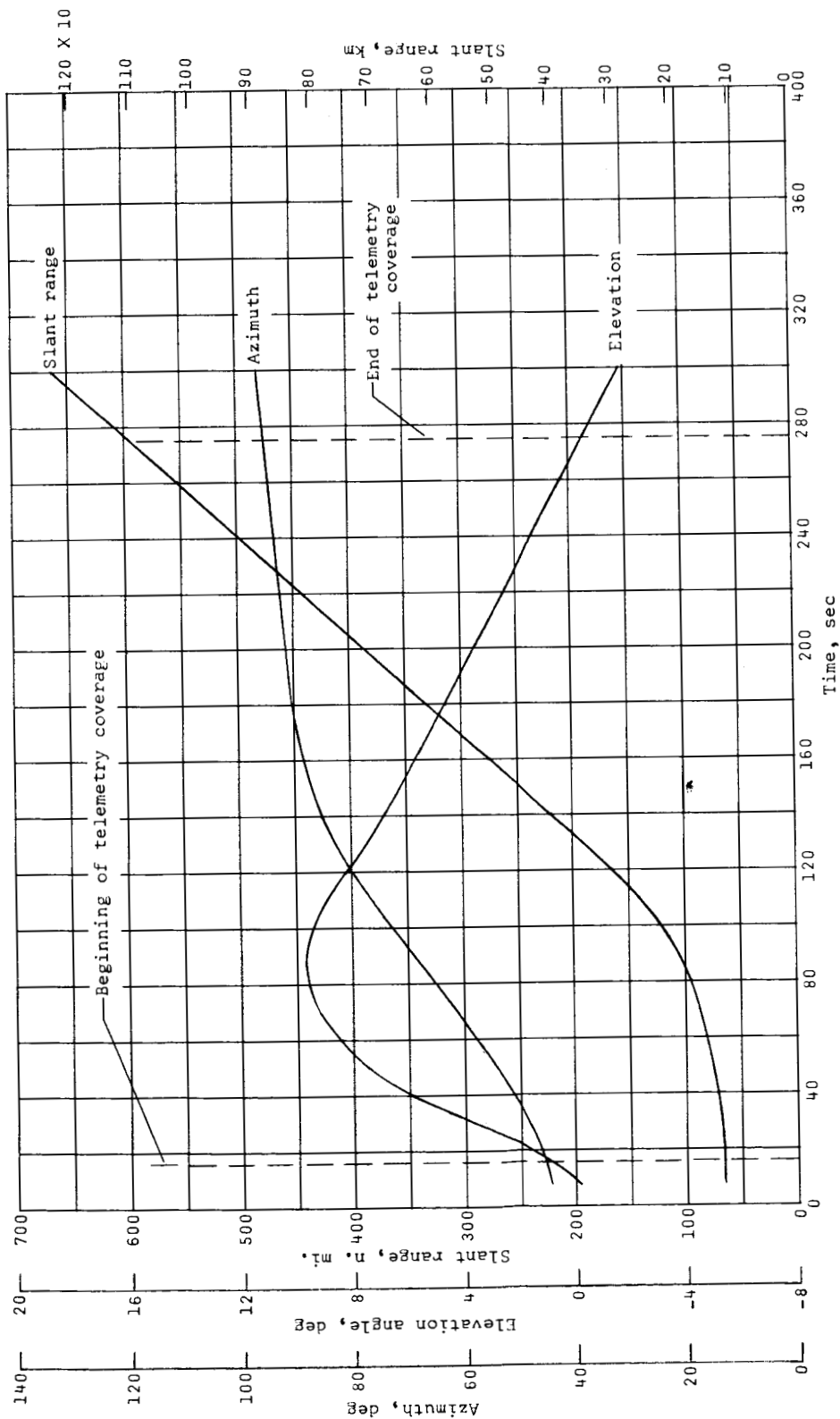
(b) Langley Station.

Figure 11.- Continued.
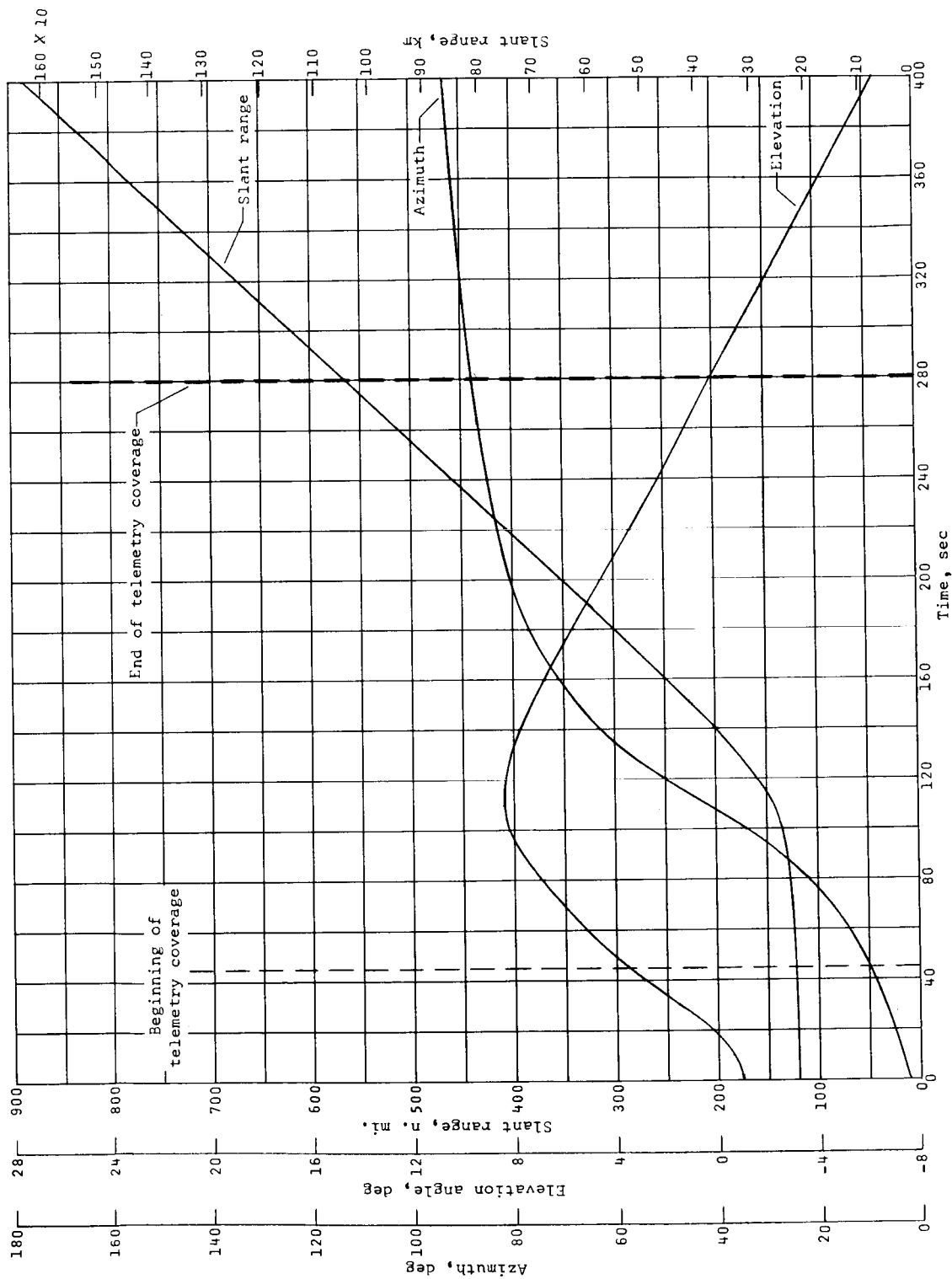
(c) Coquina Beach.

Figure 11.- Continued.
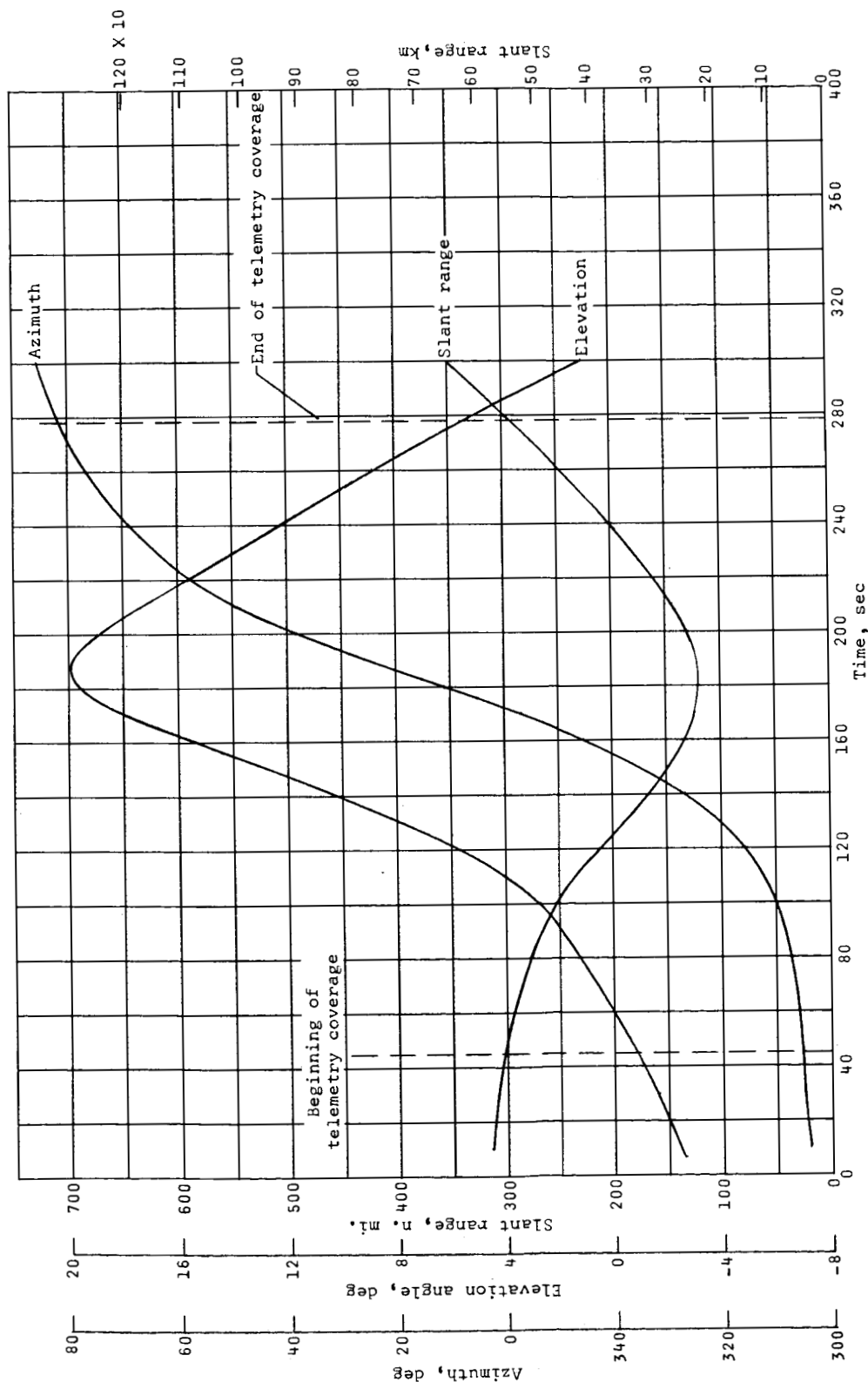
(d) Range Recoverer.

Figure 11.- Continued.
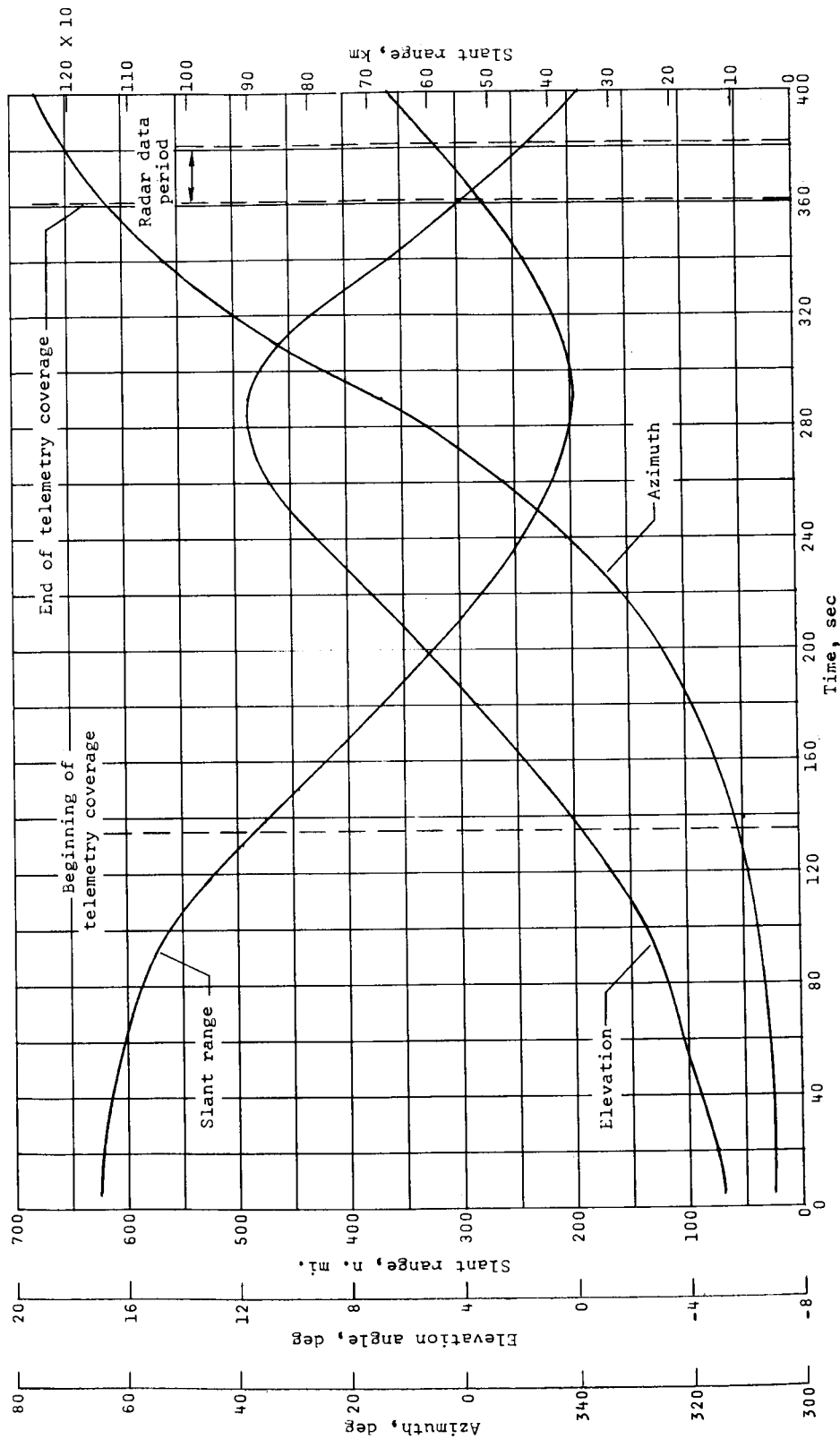
(e) Bermuda.

Figure 11.- Concluded.
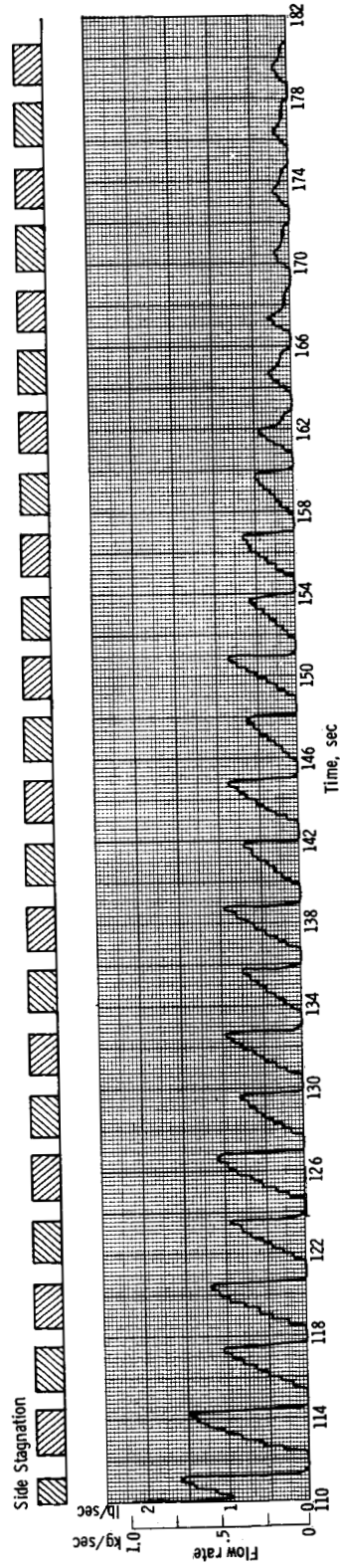
Figure 12.- Variation of flow rate with time.
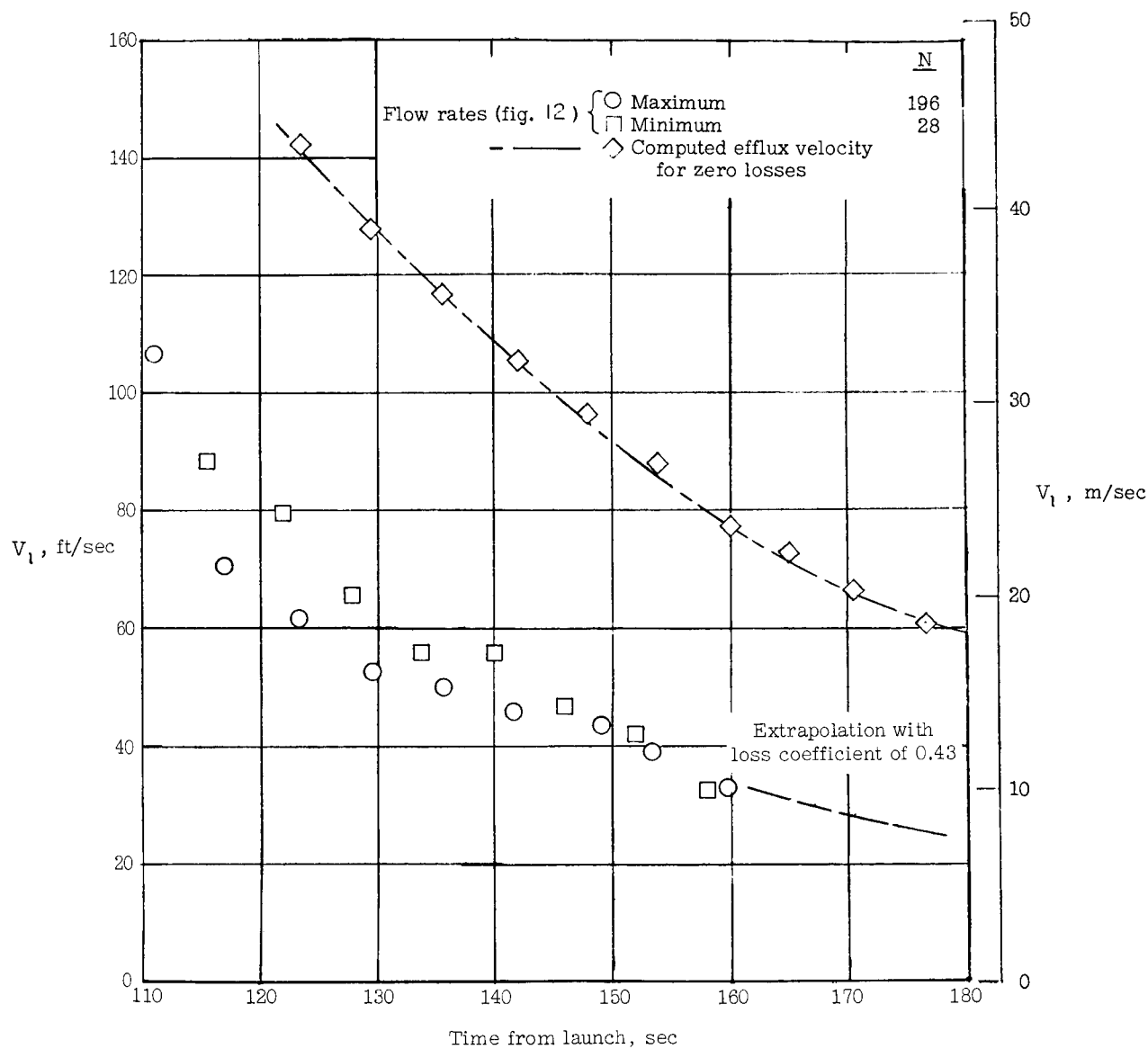
(a) Side injection. $d_0 = 0.015$ inch (0.04 cm).

Figure 13.- Water efflux velocity at exit of orifices.
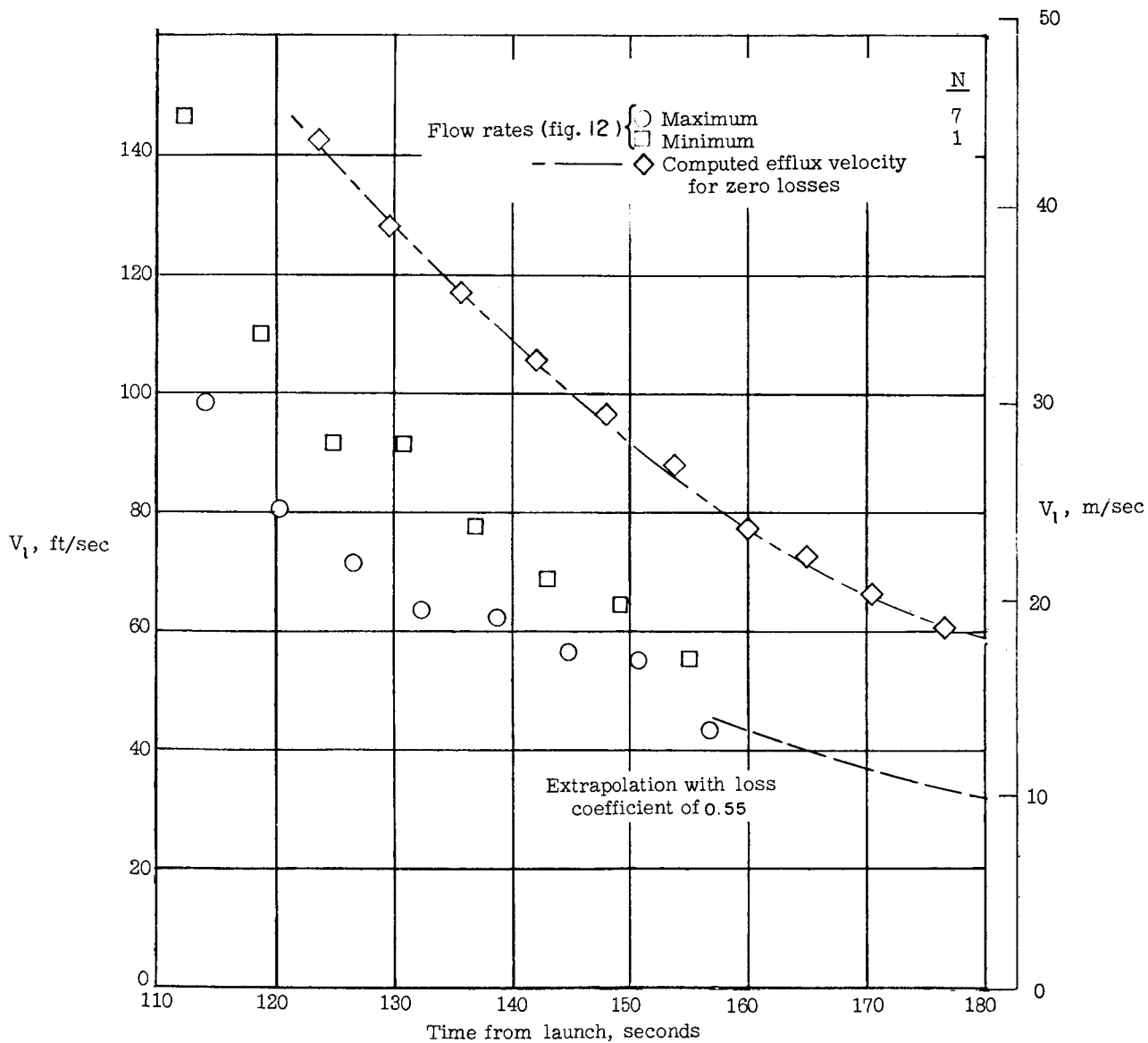
(b) Stagnation injection. d_0 = 0.08 inch (0.2 cm).

Figure 13.- Concluded.
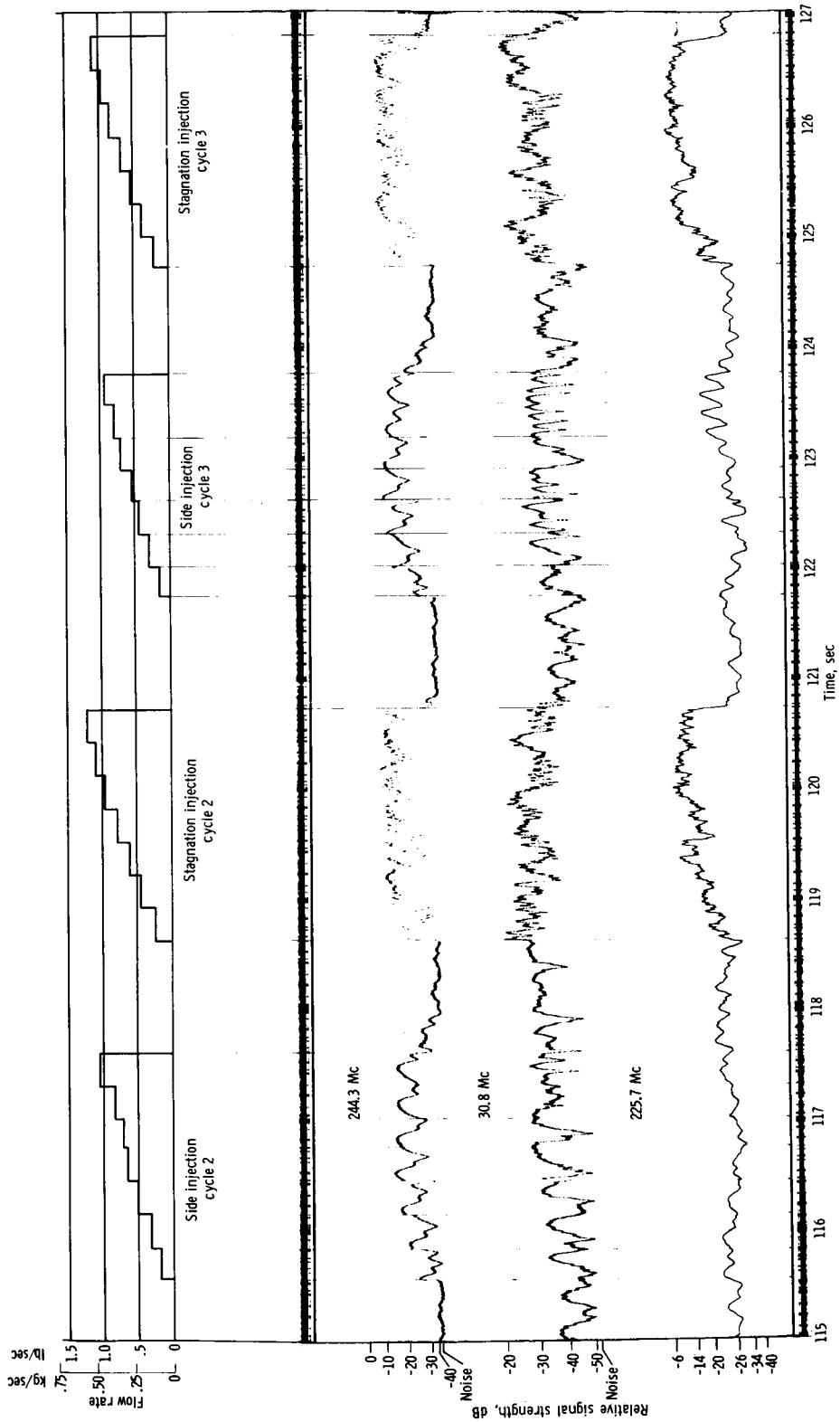
(a) Wallops Station.

Figure 14.- Typical signal-strength oscillograph records.
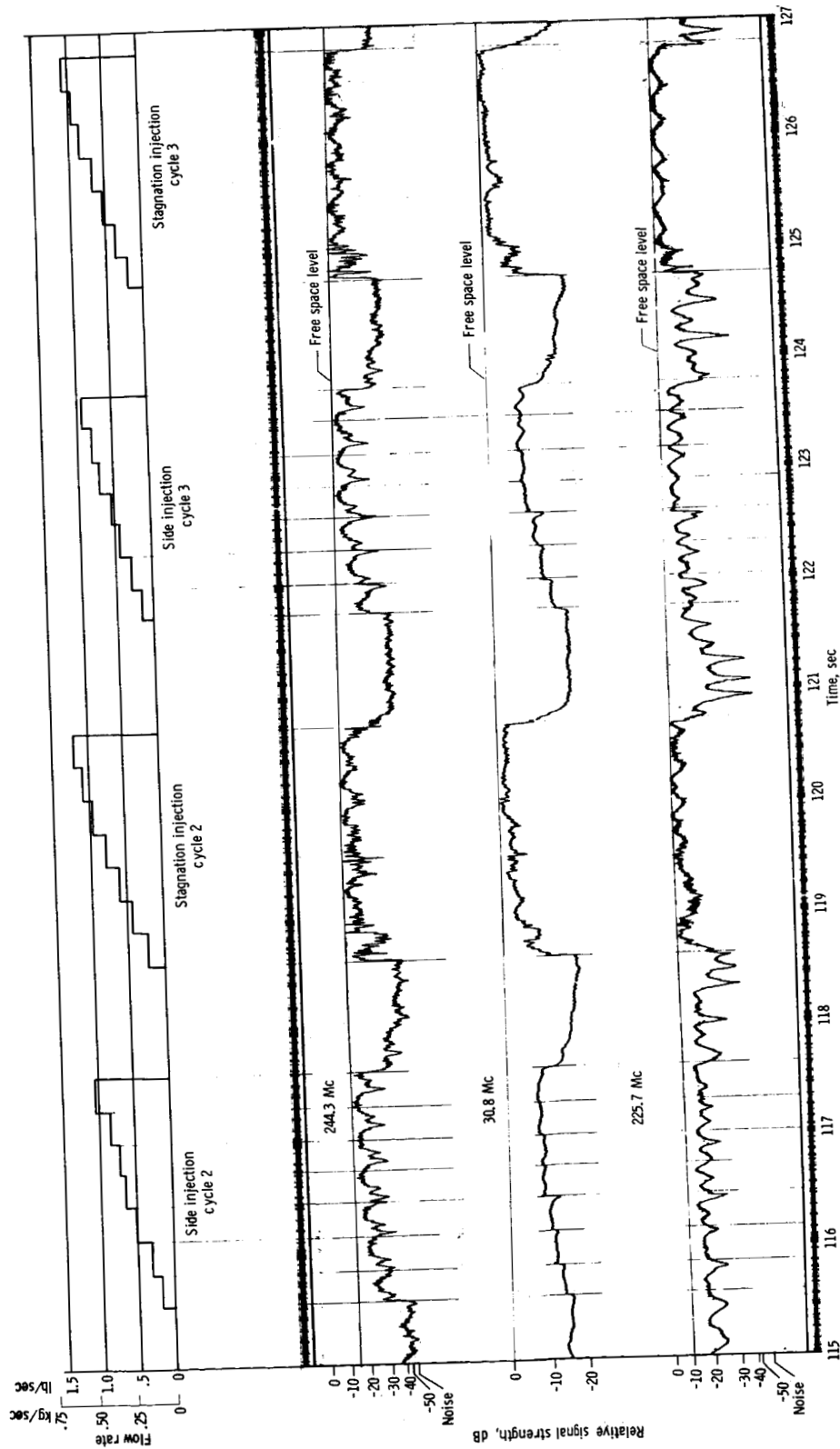
(b) Coquina Beach.

Figure 14.- Concluded.

(a) 244.3 Mc.

(b) 30.8 Mc.

(c) 225.7 Mc.
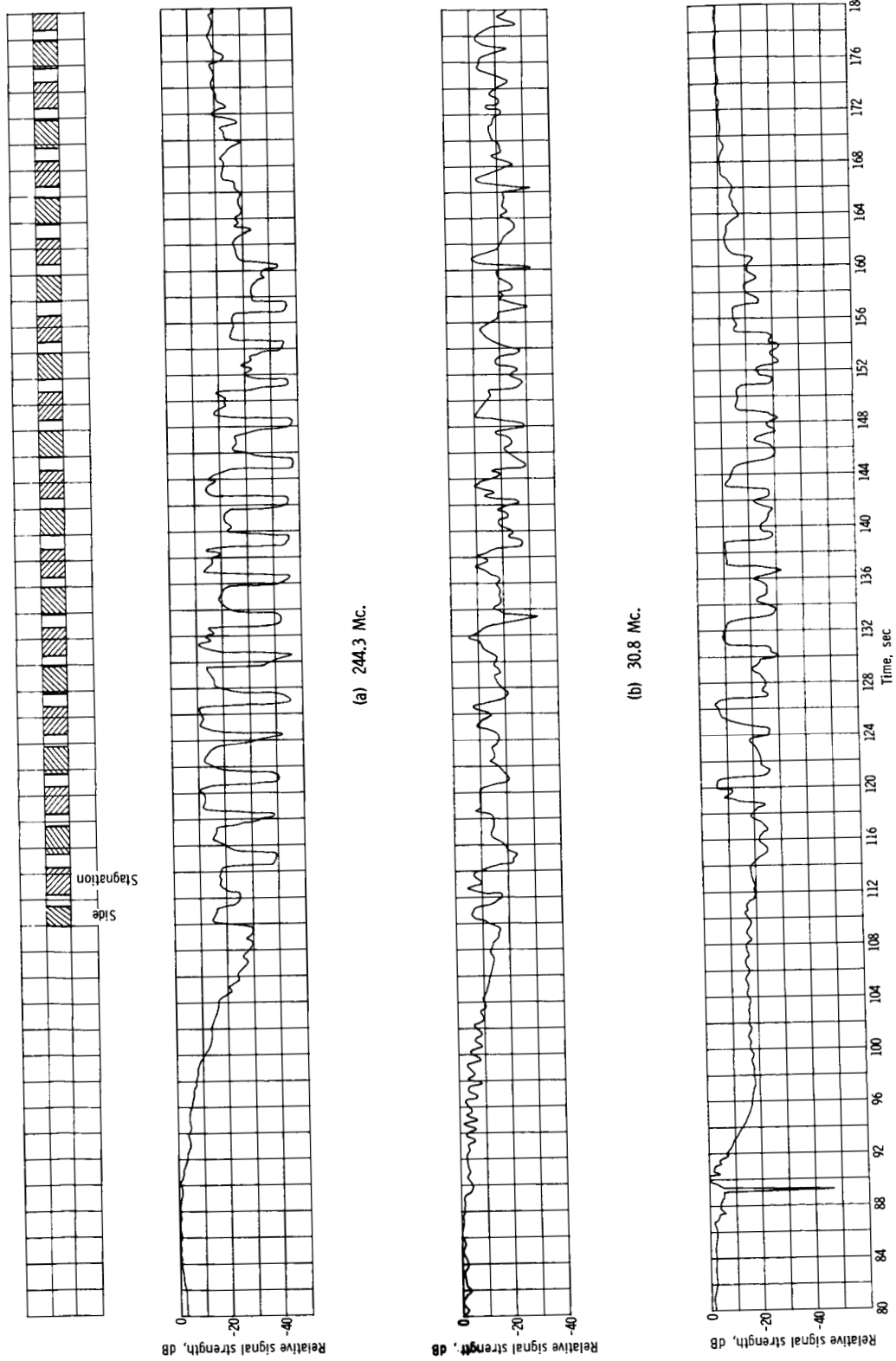
Figure 15.- Selected signal-strength record for Wallops Station.

Side
Stagnation

(a) 244.3 Mc.

(b) 30.8 Mc.

(c) 225.7 Mc.

Relative signal strength, dB

Time, sec
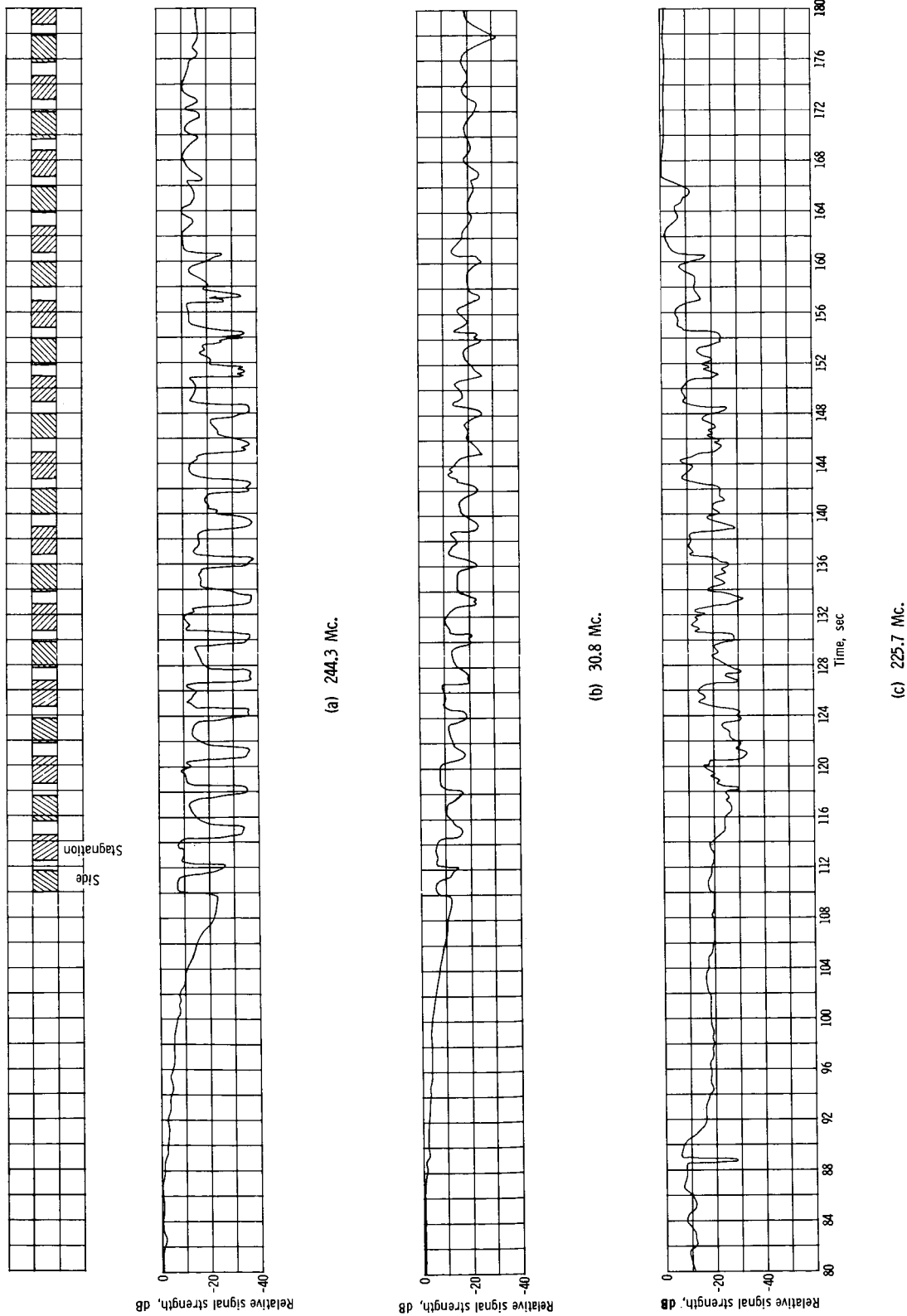
Figure 16.- Selected signal-strength record for Langley Station.
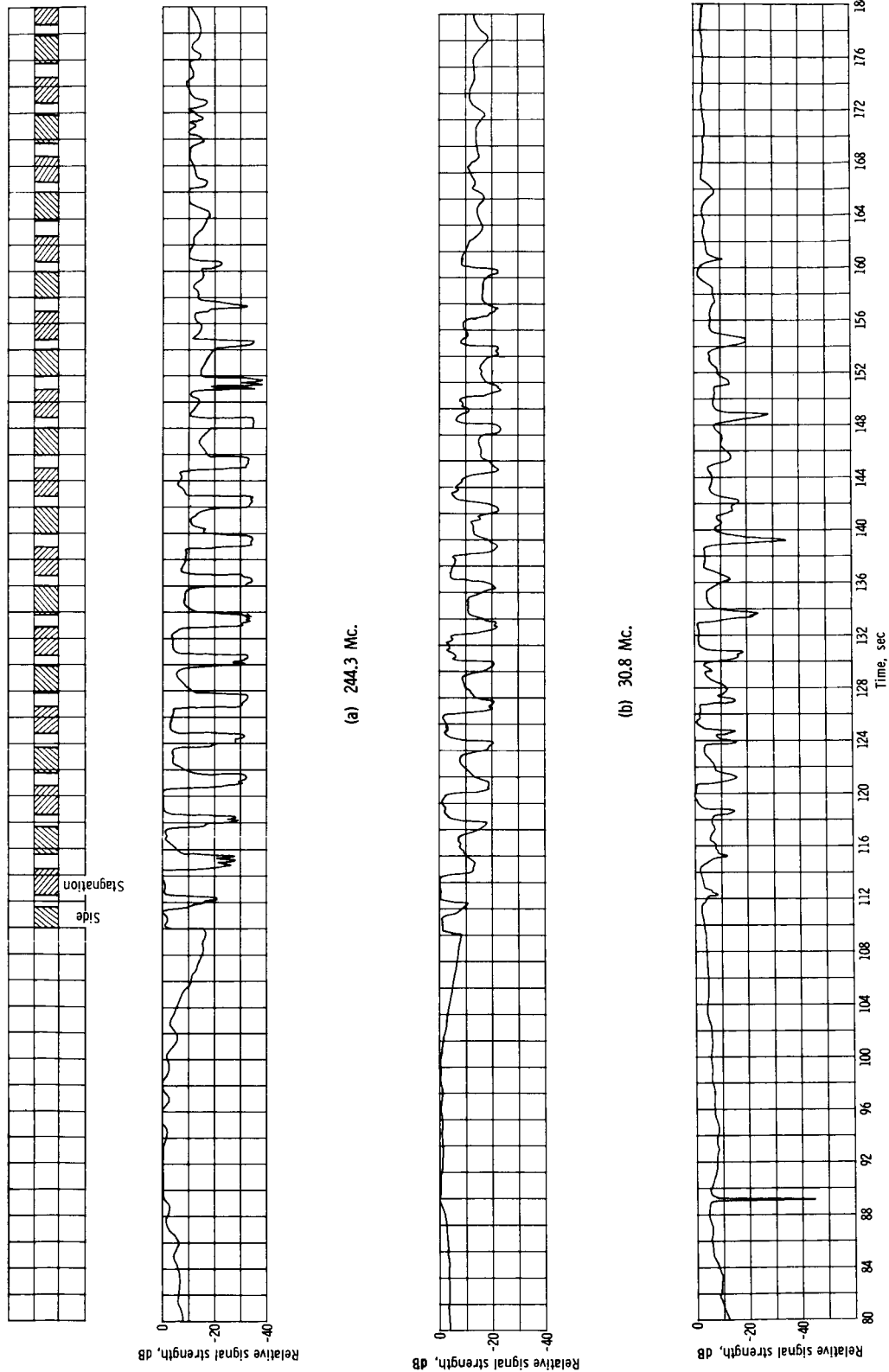
Figure 17.- Selected signal-strength record for Coquina Beach.

(a) 244.3 Mc.

(b) 30.8 Mc.

(c) 225.7 Mc.

(a) 244.3 Mc.

(b) 225.7 Mc.
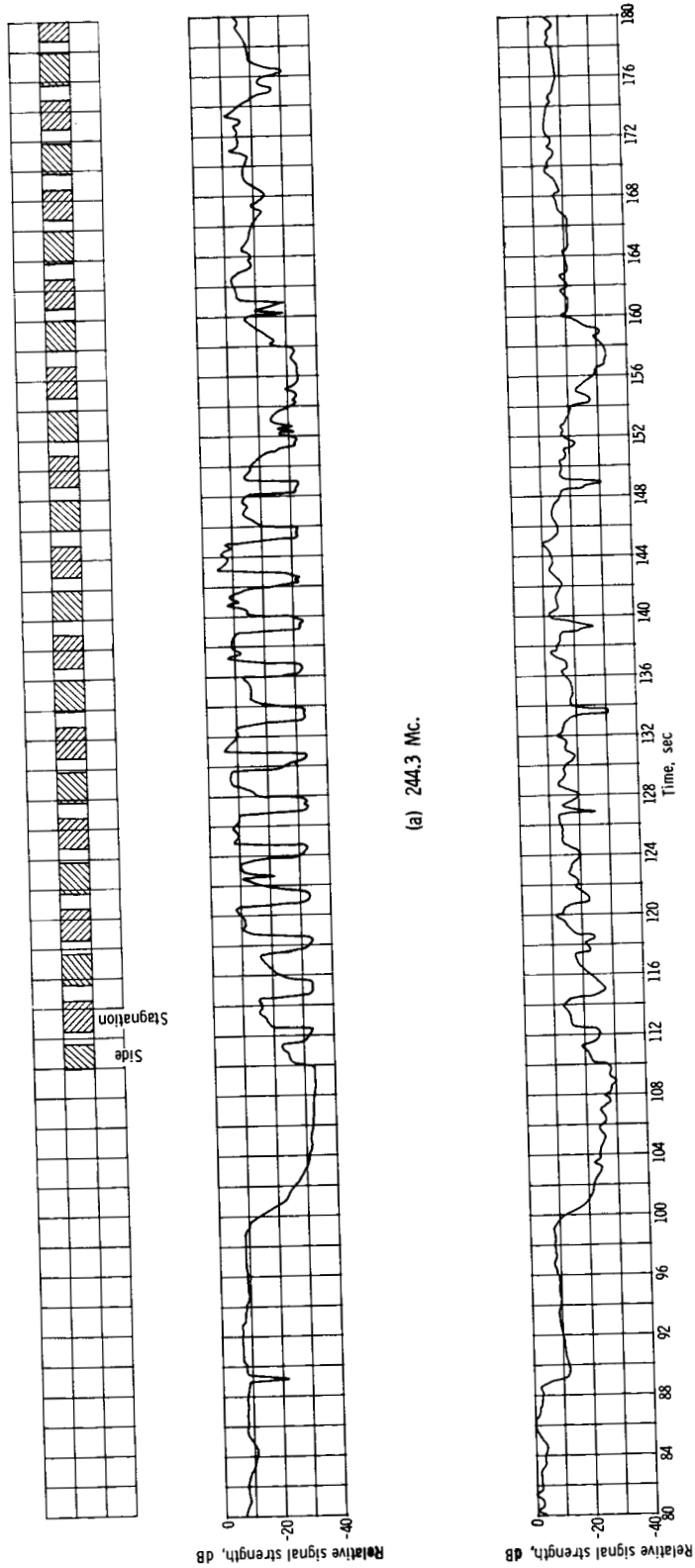
Figure 18.- Selected signal-strength record for Range Recoverer.

(a) 244.3 Mc.

(b) 225.7 Mc.
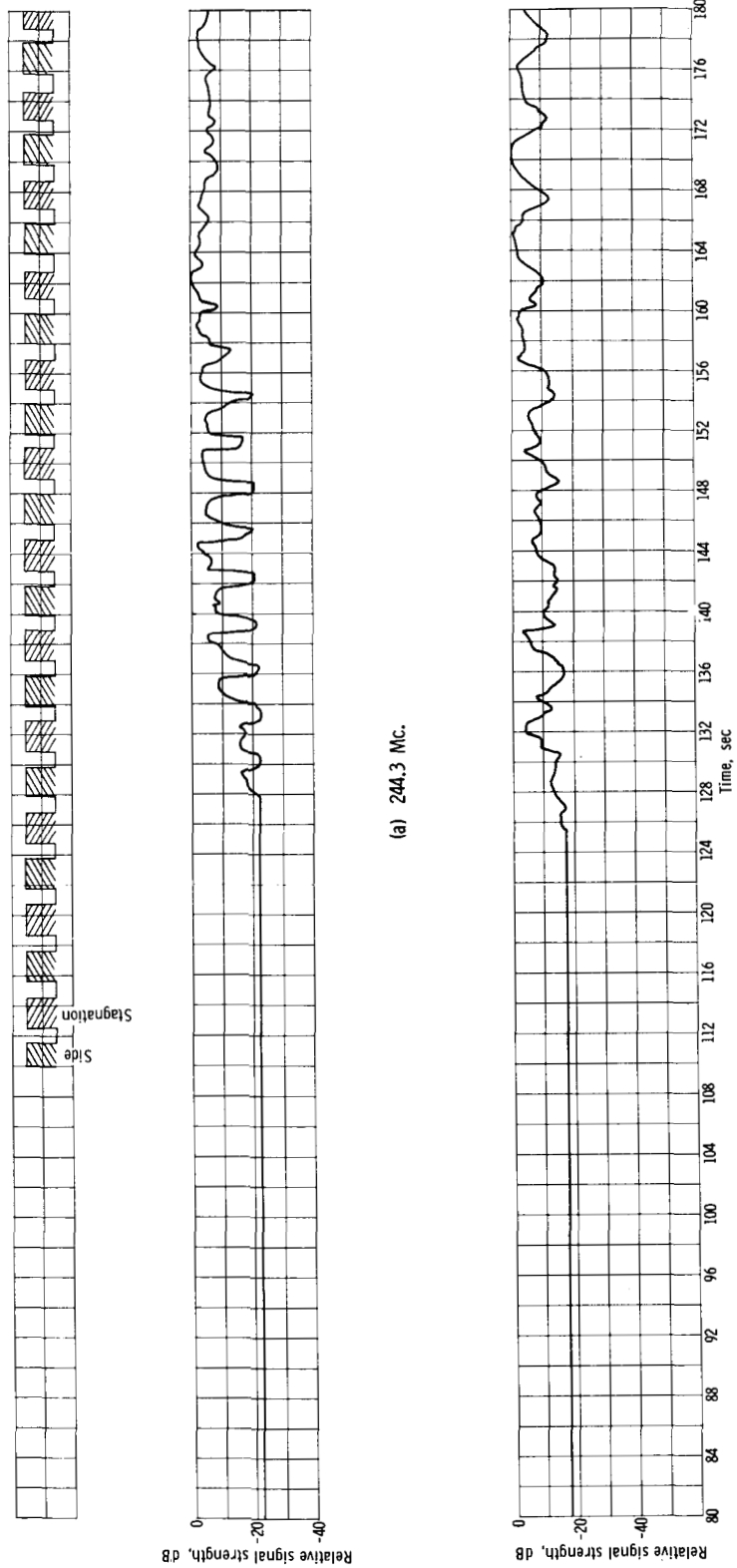
Figure 19.- Selected signal-strength record for Bermuda.
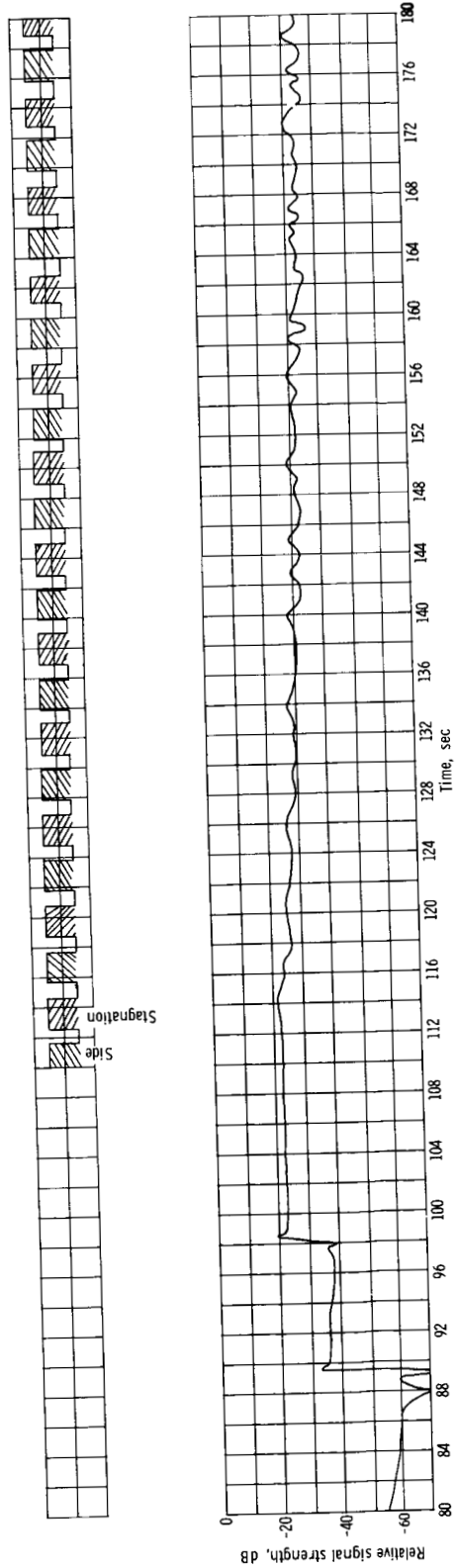
Figure 20.- C-band signal-strength record for Wallops Station.
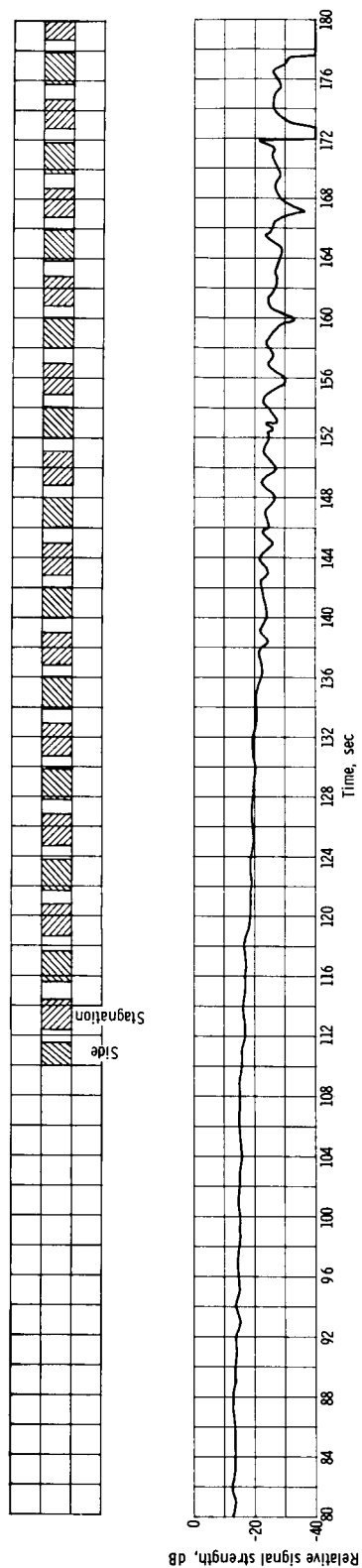
Figure 21.- X-band signal-strength record for Coquina Beach.

100
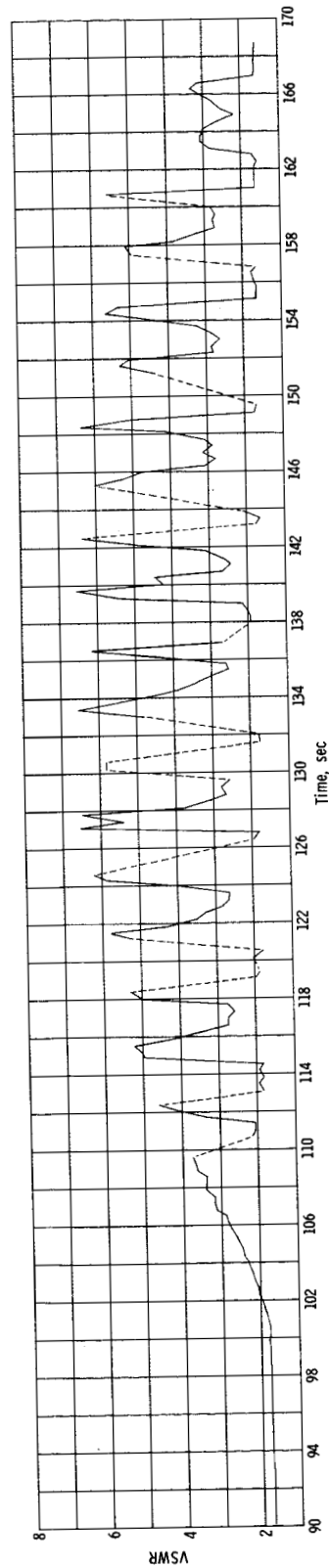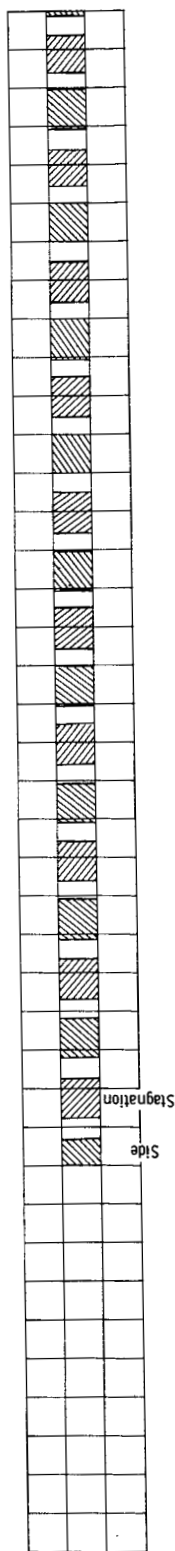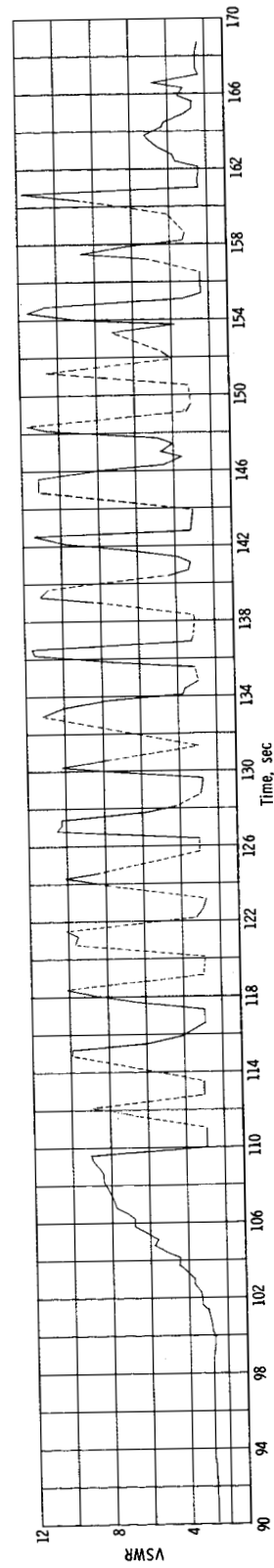
Figure 22.- Measured voltage standing-wave ratio on 244.3-Mc and 30.8-Mc systems. Dashed lines indicate regions of a limited amount of data.
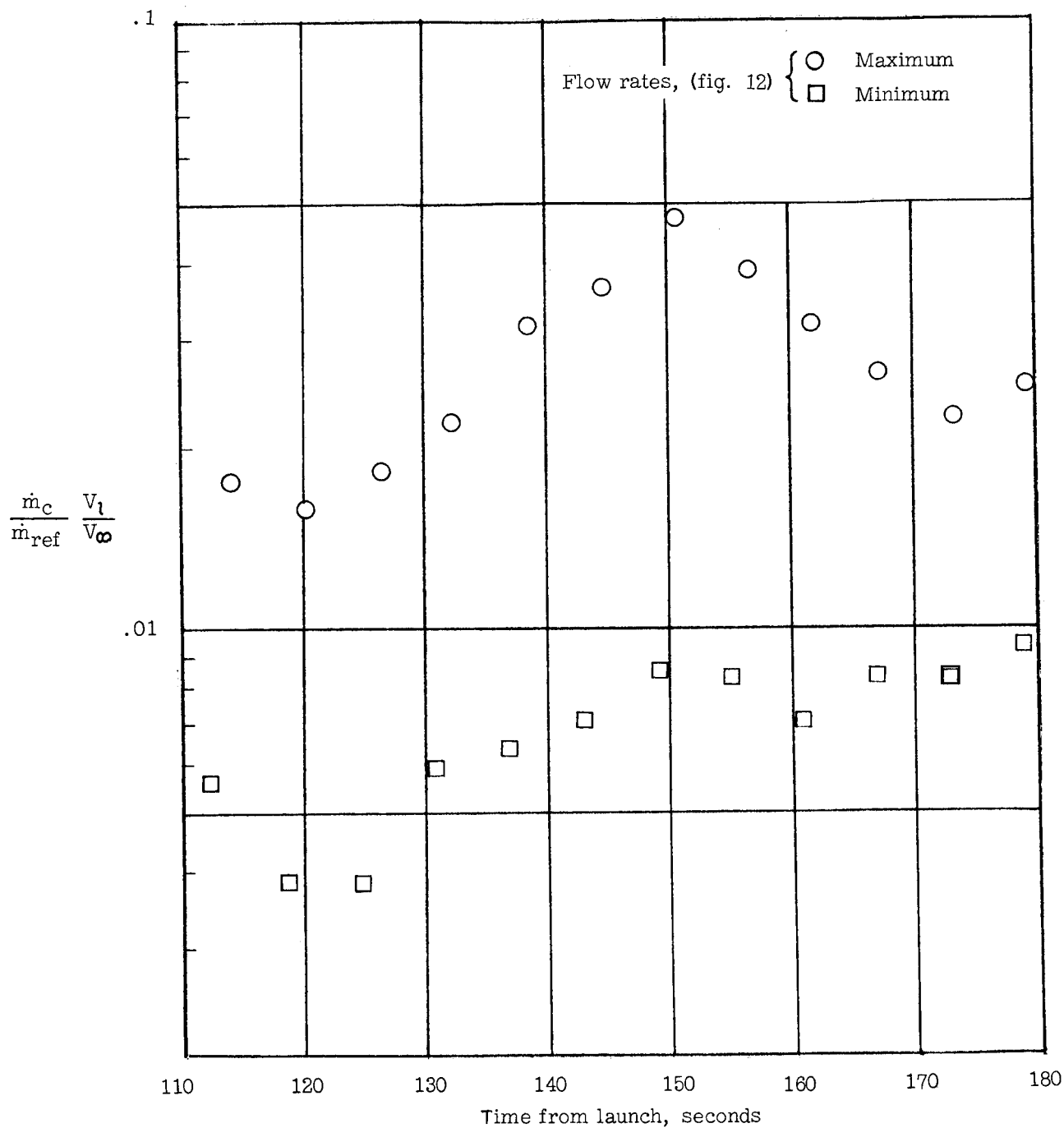
(a) Momentum flux ratio based on actual efflux velocity from figure 13.

Figure 23.- Variation in stagnation-point-injection parameters.
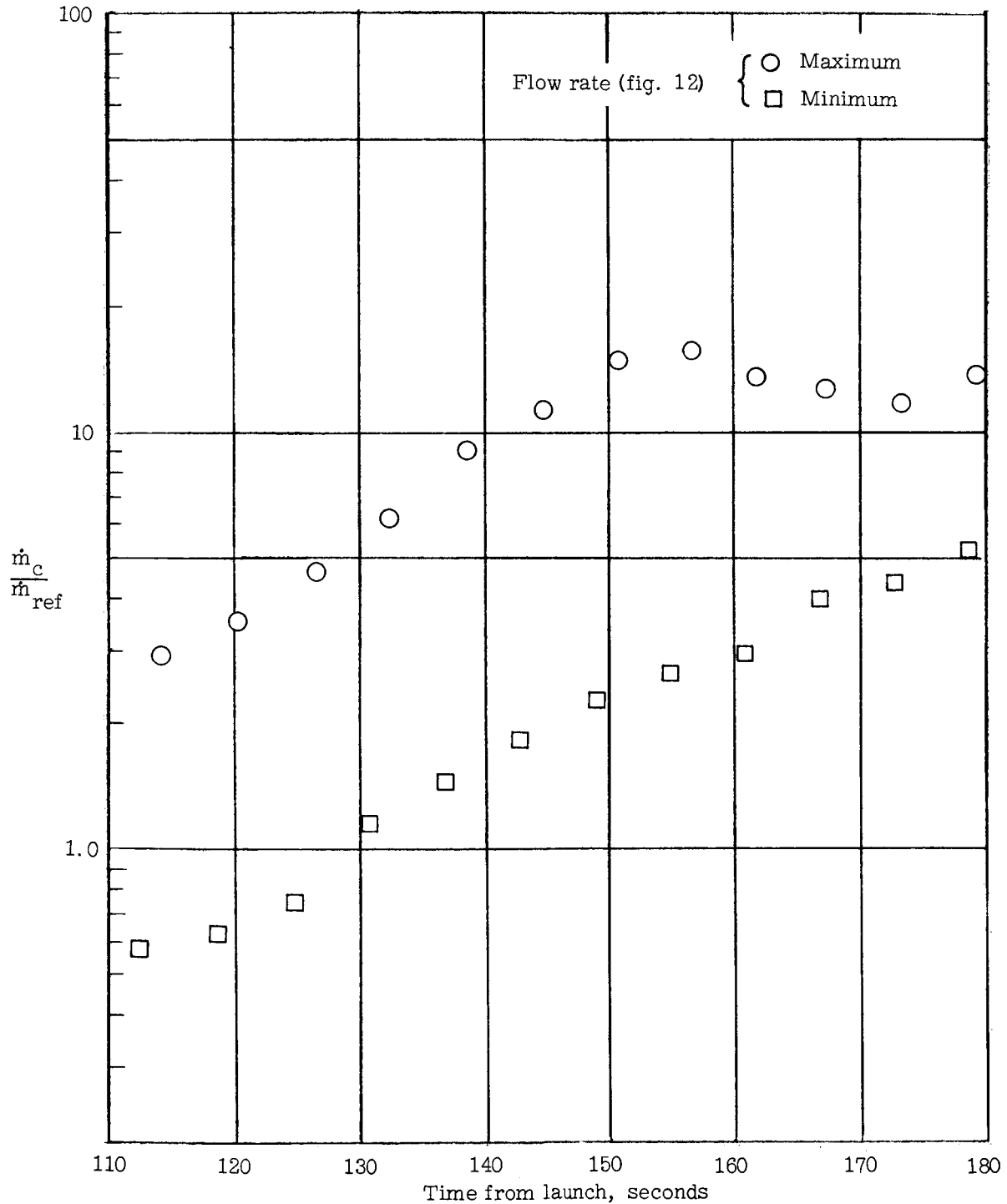
(b) Mass flux ratio.

Figure 23.- Concluded.
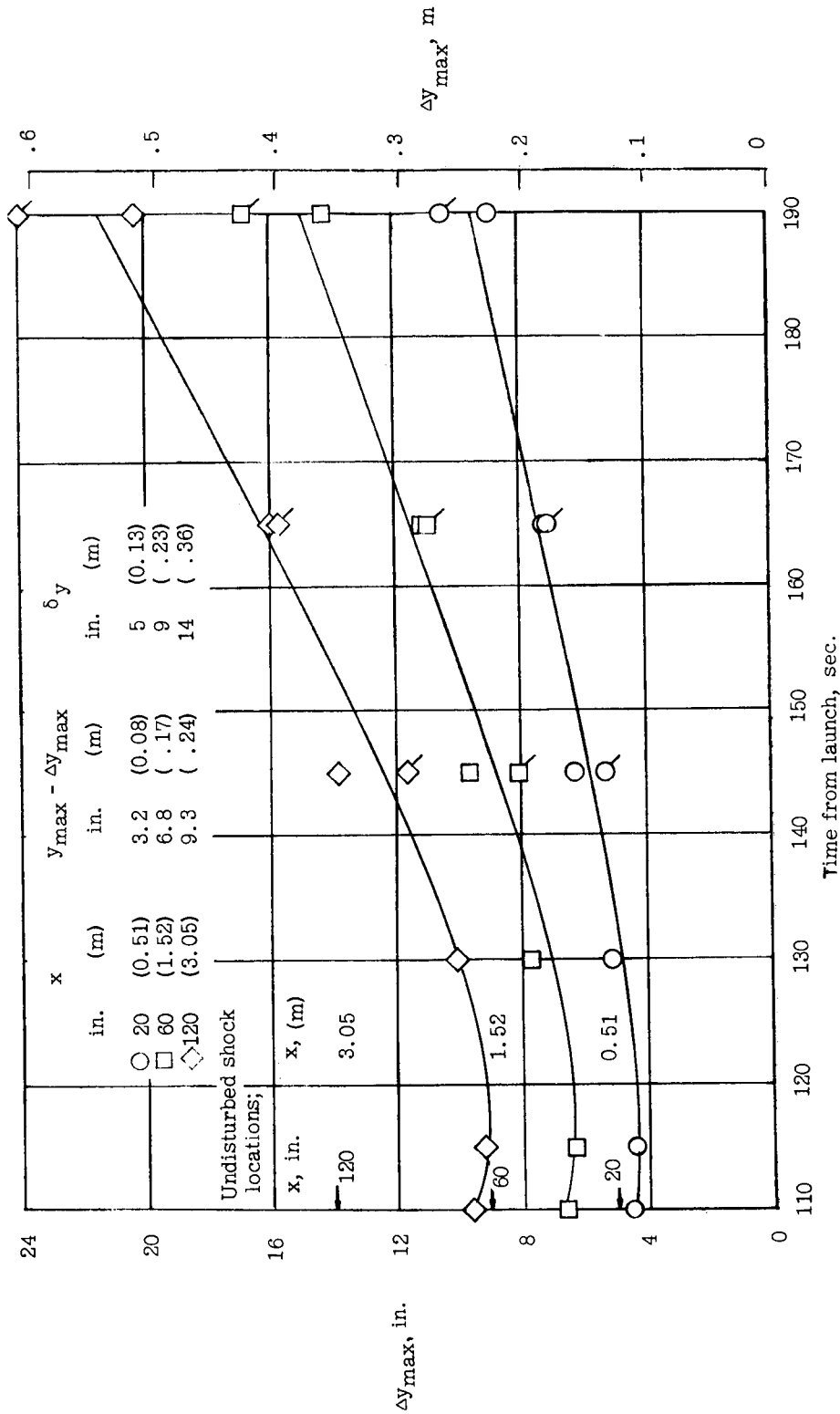
Figure 24.- Maximum predicted spray penetration for side injection on RAM B2 flight as obtained from wind-tunnel correlations. Plain symbols from equation (3) for $1 < \frac{p_v}{p_a} < 10$; tagged symbols from equation (4) for $90 < \frac{p_v}{p_a} < 700$.

104
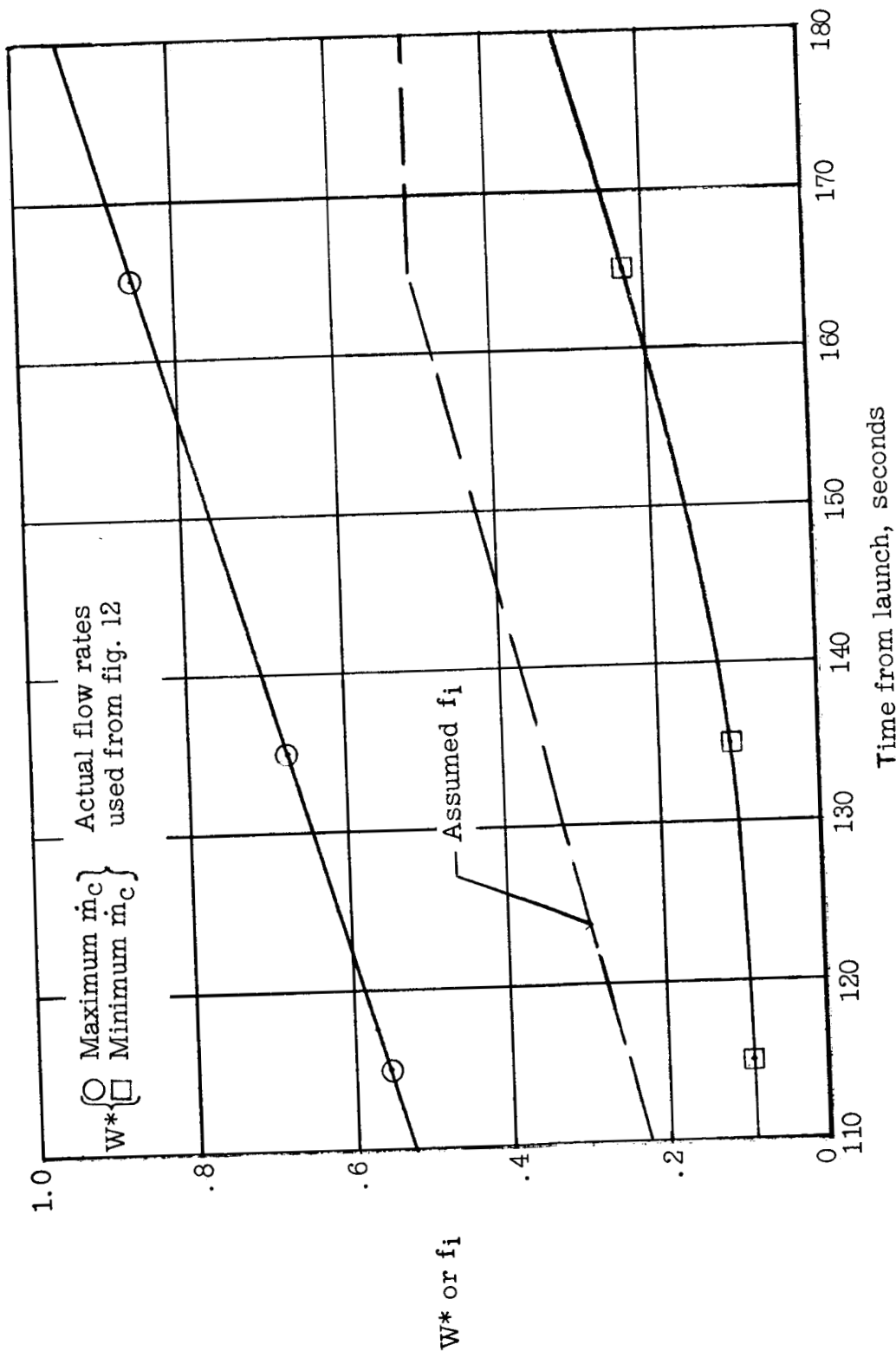
Figure 25.- Estimated values of W* at forward antenna station (x = 20 in. (50.8 cm)) based on f_i variation shown.
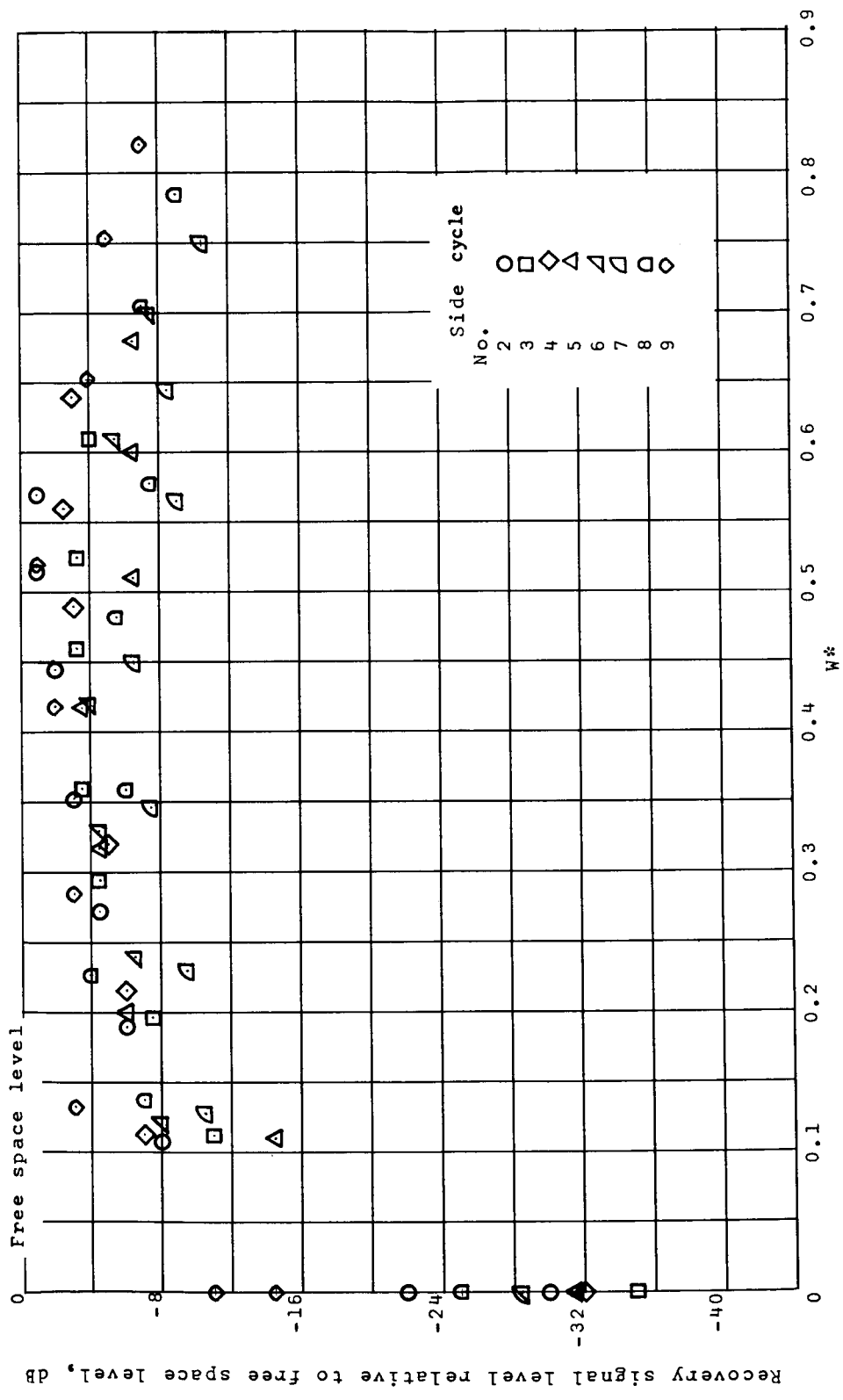
(a) Coquina Beach. 244,3 Mc.

Figure 26.- Recovery signal-strength level relative to free space signal level as plotted as a function of W^* for side injection on RAM B2.
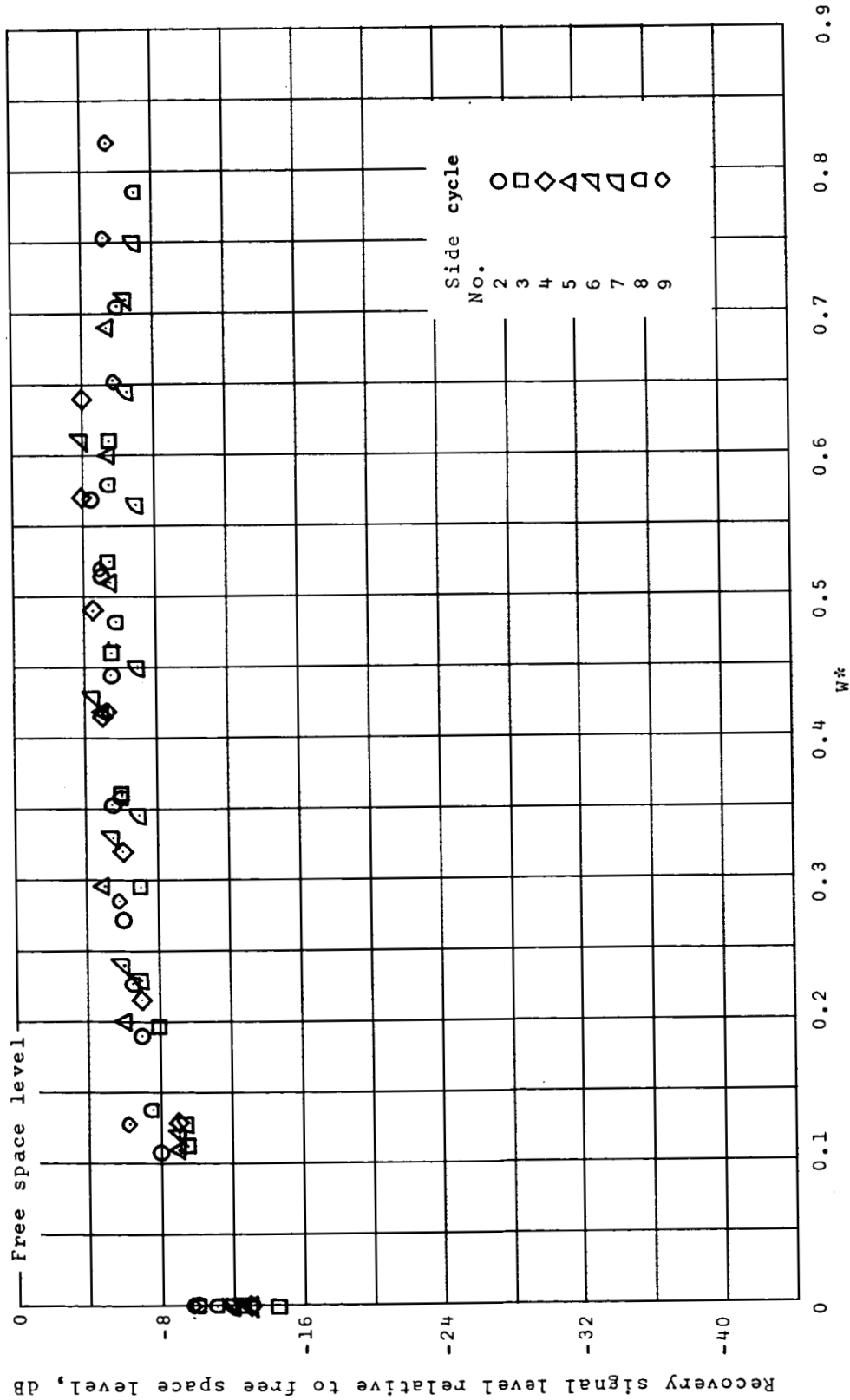
(b) Coquina Beach. 30.8 Mc.

Figure 26.- Continued.
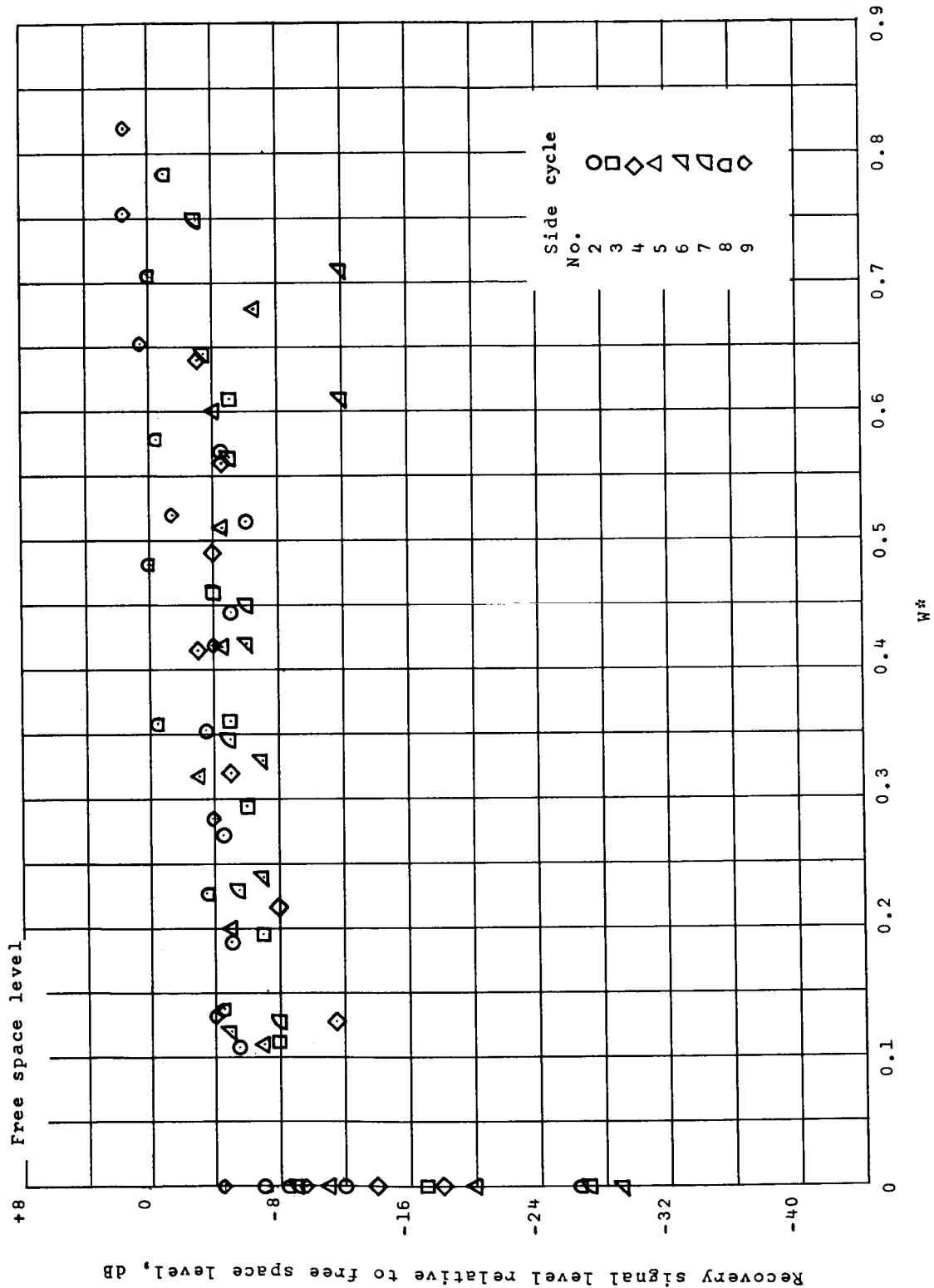
(c) Coquina Beach. 225.7 Mc.

Figure 26.- Continued.

108
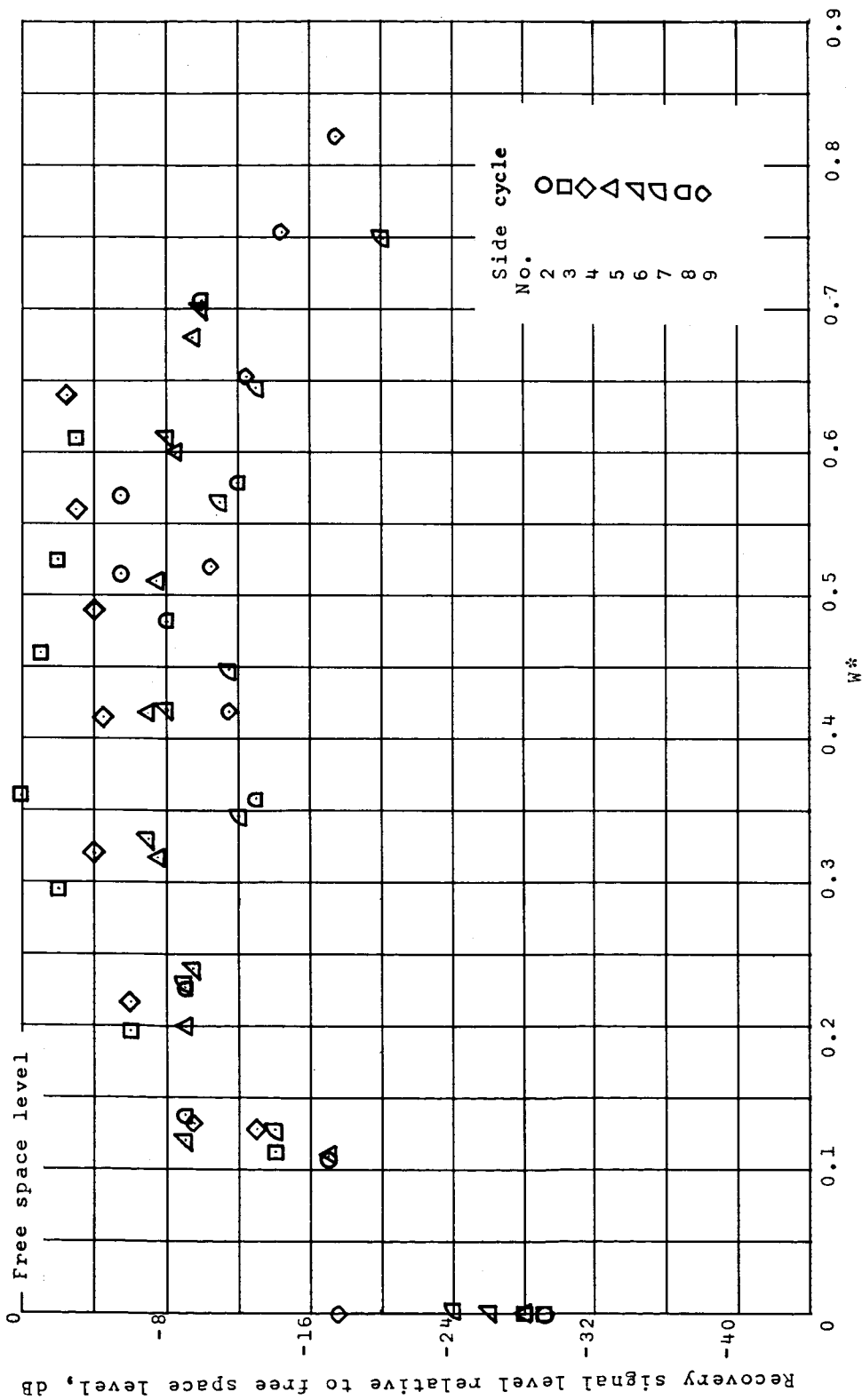
(d) Wallops Station. 244.3 Mc.

Figure 26.- Concluded.
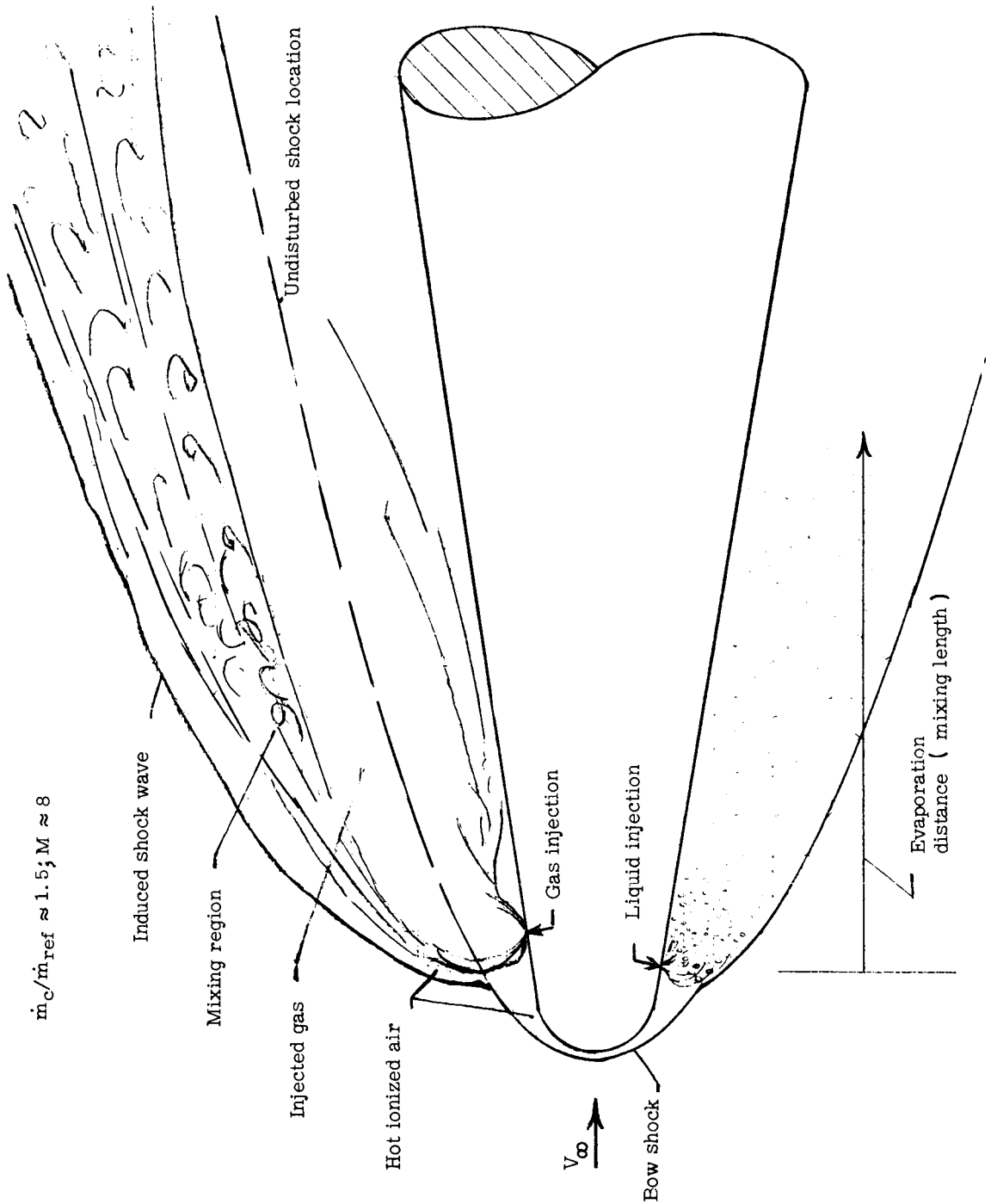
Figure 27.- Comparison of liquid injection with gas injection.
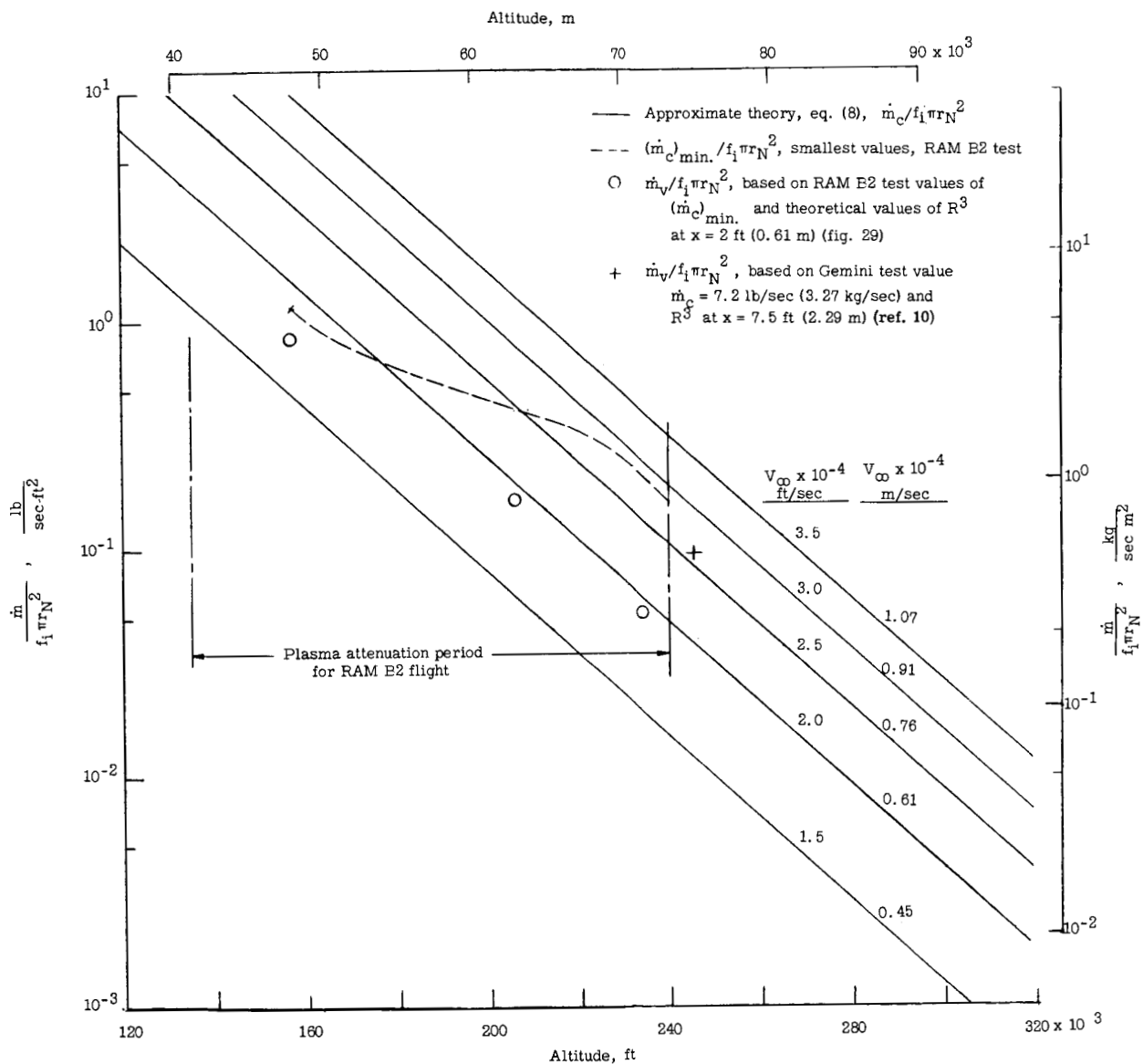
Figure 28.- Comparison of theoretical and experimental values of water-flow-rate parameter required to give $N_e < 10^9$ electrons/cm³. Theoretical predictions from equation (8) with $\rho_{ref} = 0.0765$ lbm/ft³ (1.2 kg/m³), $\beta = 4.16 \times 10^{-5}$ per foot (per 0.3 m), $\Delta h_{a,2} = 0.5 \times 10^8$ ft²/sec² (0.1 × 10¹² J/kg), $\Delta h_{c,2} = 4.4 \times 10^8$ ft²/sec² (1.0 × 10¹² J/kg), and $(r_i/r_N)^2 = 2.0$.
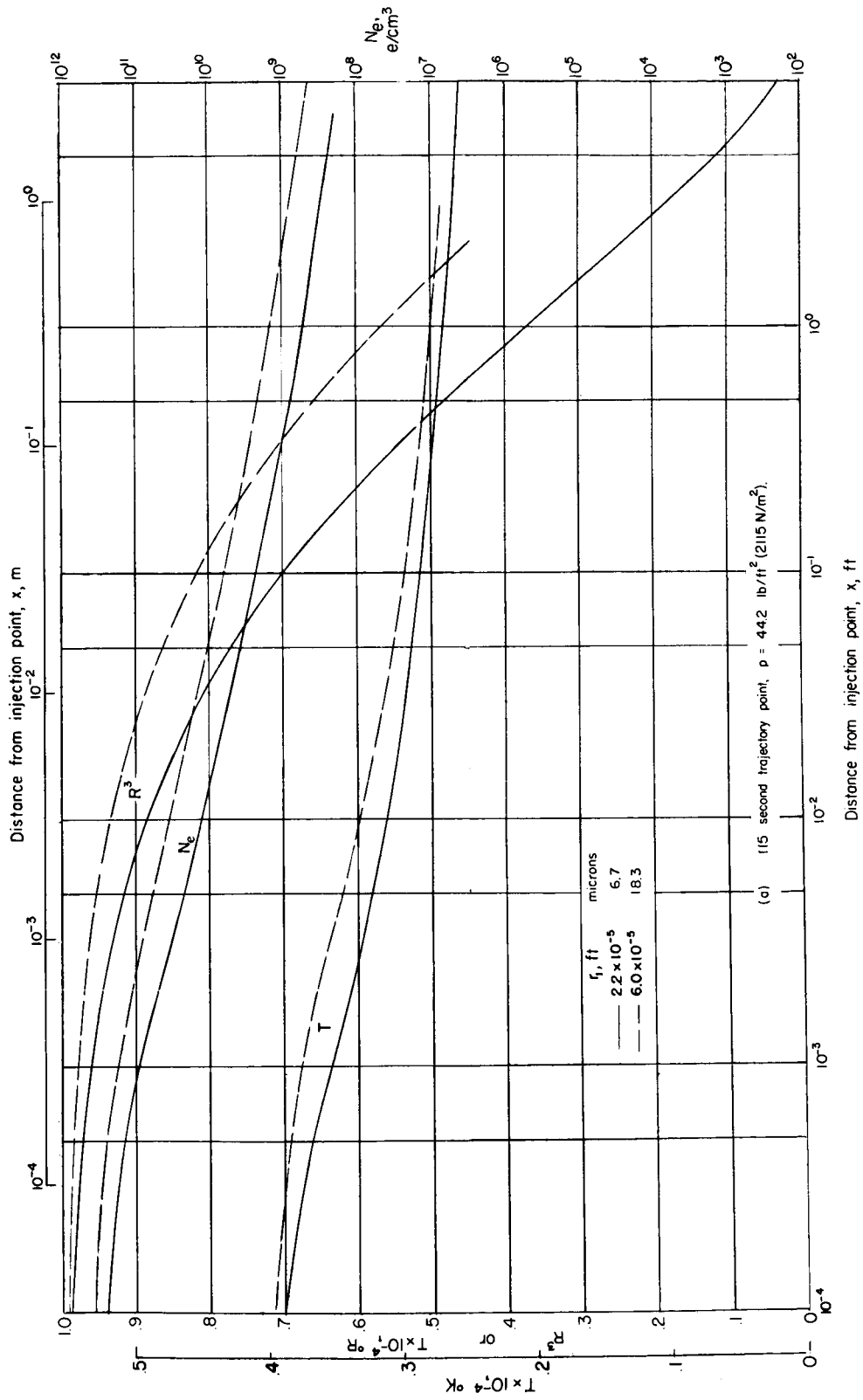
Figure 29.- Variation of mixture temperature T, weight fraction of water in liquid phase R^3, and electron concentration N_e. $W^* = 0.5$.

(a) 115 second trajectory point, $p = 44.2$ lb/ft^2 (2115 N/m^2).

112

(b) 145 second trajectory point, p = 7.07 lb/ft², (338.51 N/m²), r_j = 3.5×10⁻⁵ ft, (10.7 microns).

(c) 165 second trajectory point, p = 2.64 lb/ft², (126.40 N/m²), r_j = 4.5×10⁻⁵ ft, (13.8 microns).
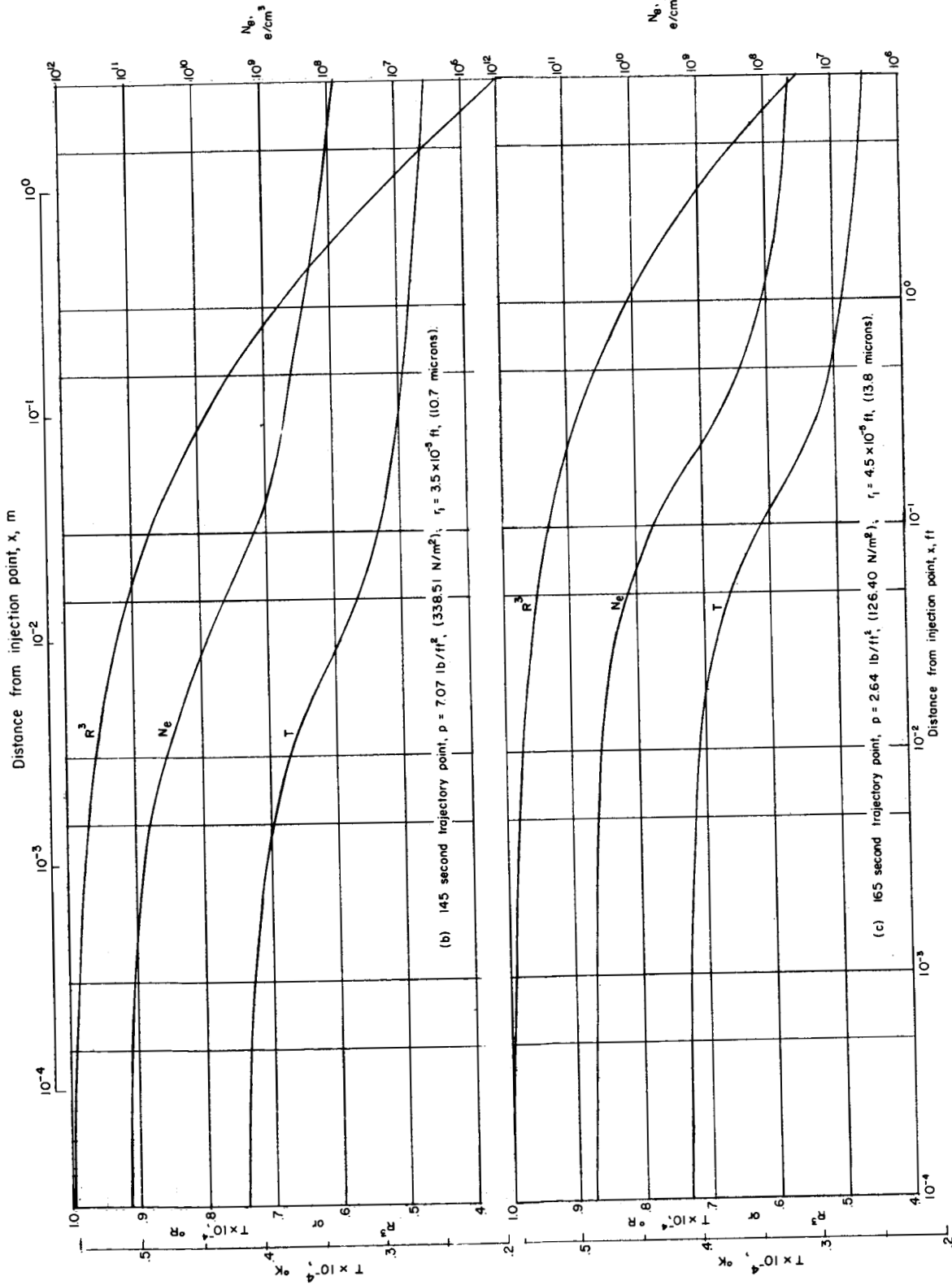
Figure 29.- Concluded.
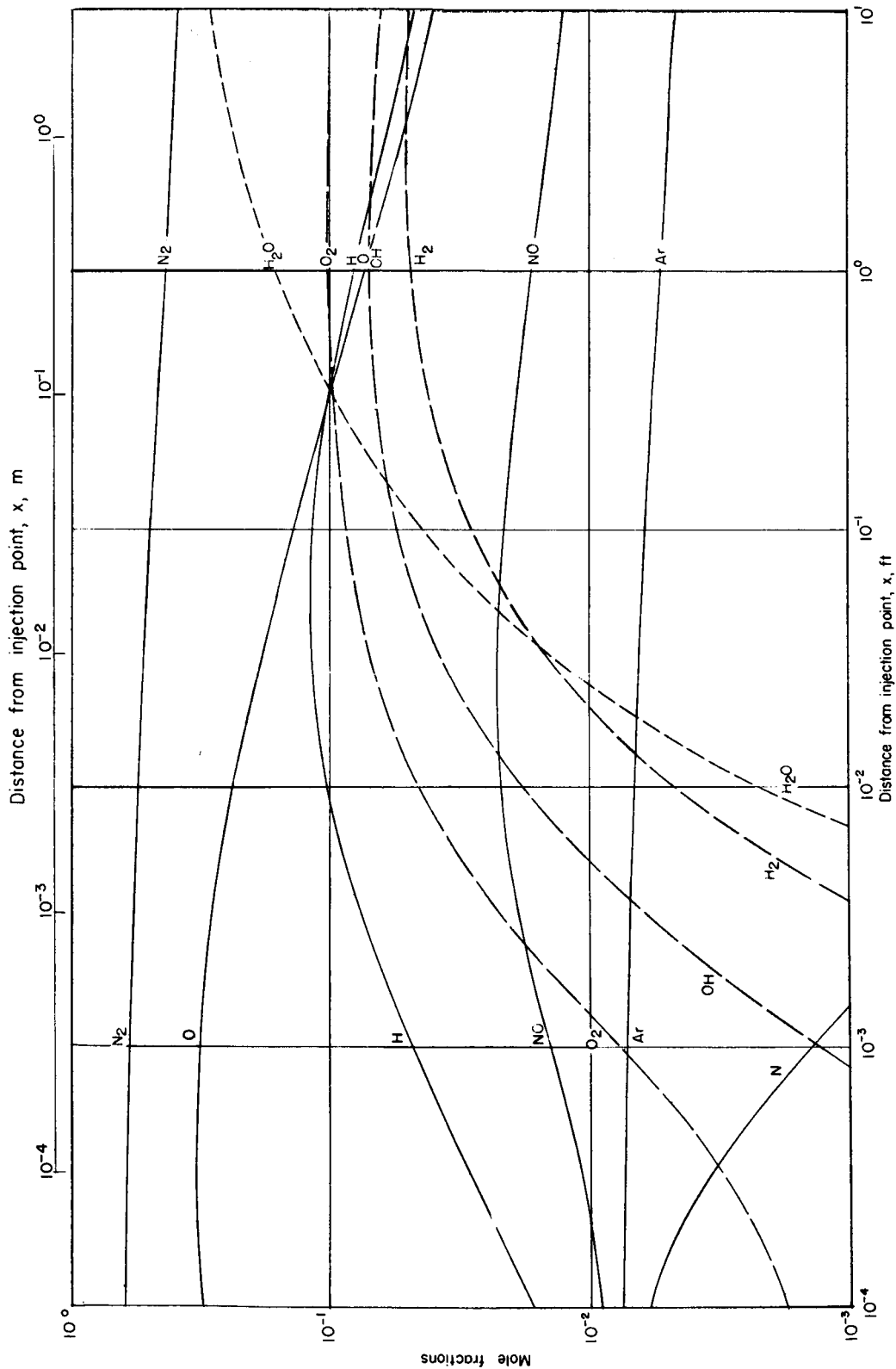
(a) 115 second trajectory point. $p = 44.2$ lbf/ft² (2116.3 N/m²).

Figure 30.- Variation of mole fractions of various constituents of mixture. $W^* = 0.5$.

114
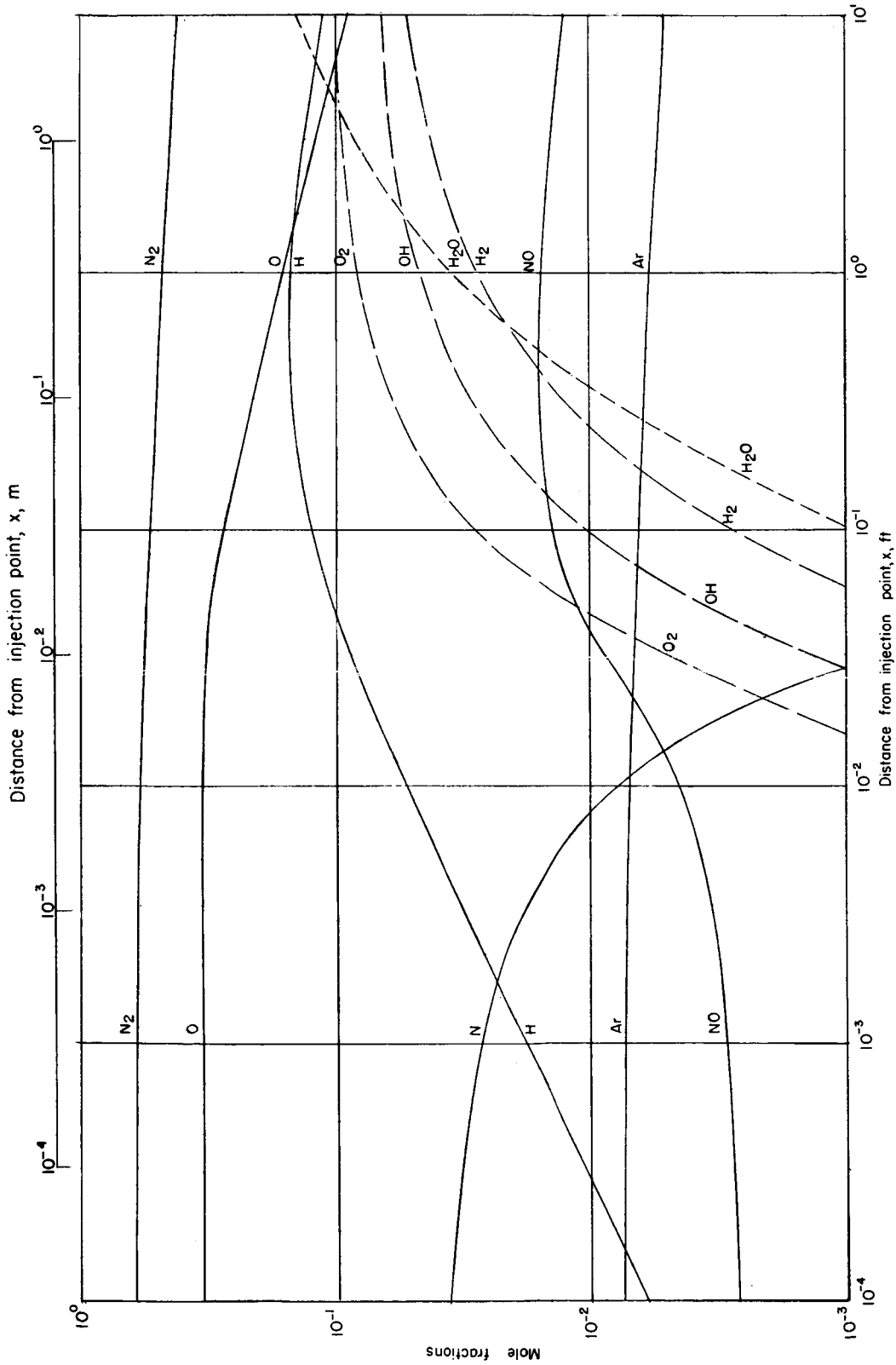
(b) 145 second trajectory point, $p = 7.07$ lbf/ft^2 (338.5 N/m^2).

Figure 30.- Continued.

(c) 165 second trajectory point. $p = 2.64$ lbf/ft^2 (126.4 N/m^2).

Figure 30.- Concluded.
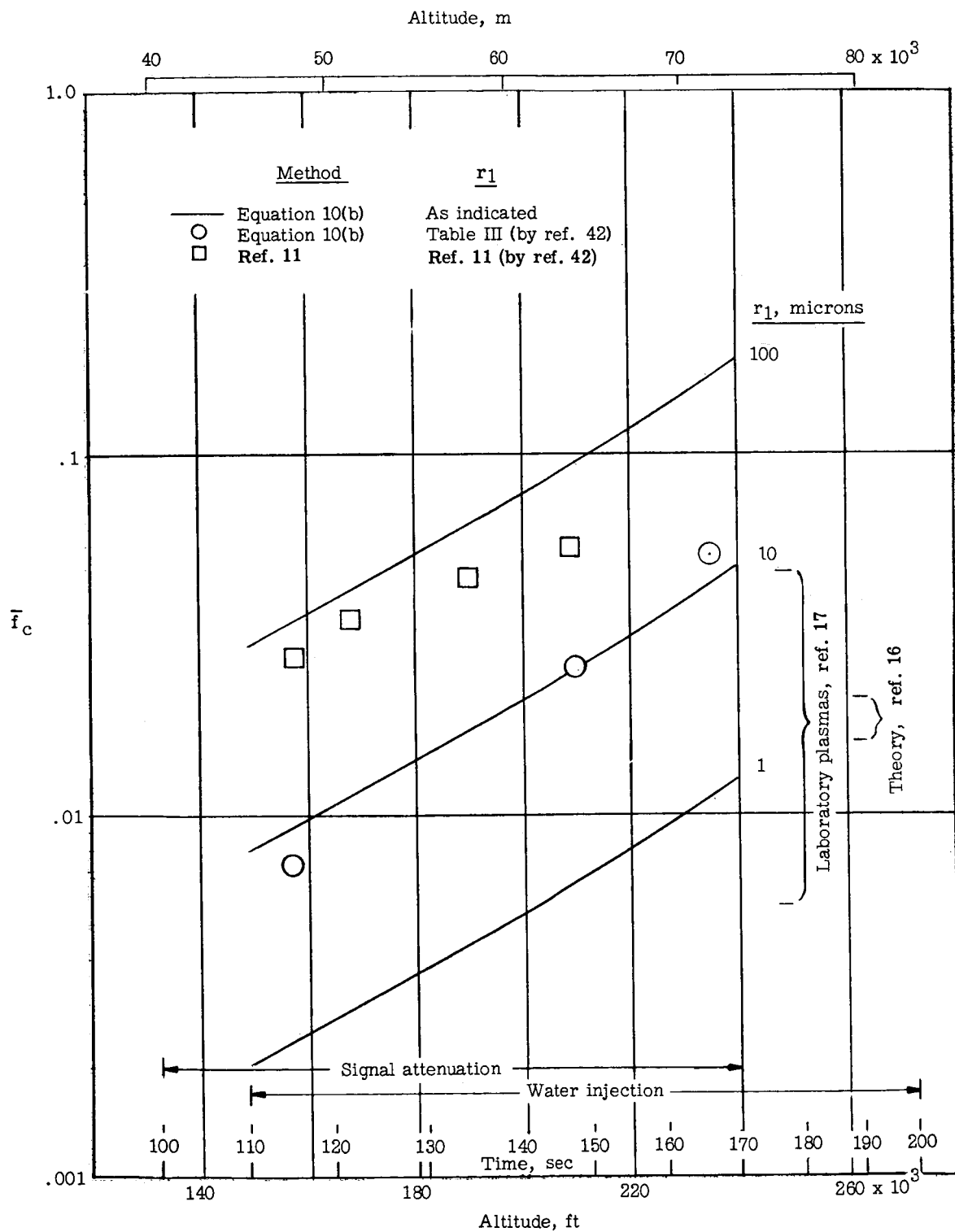
Figure 31.- Variation of recombination efficiency factor $\bar{f}_c$ with altitude for various computational methods. x = 2 ft (0.6 m).
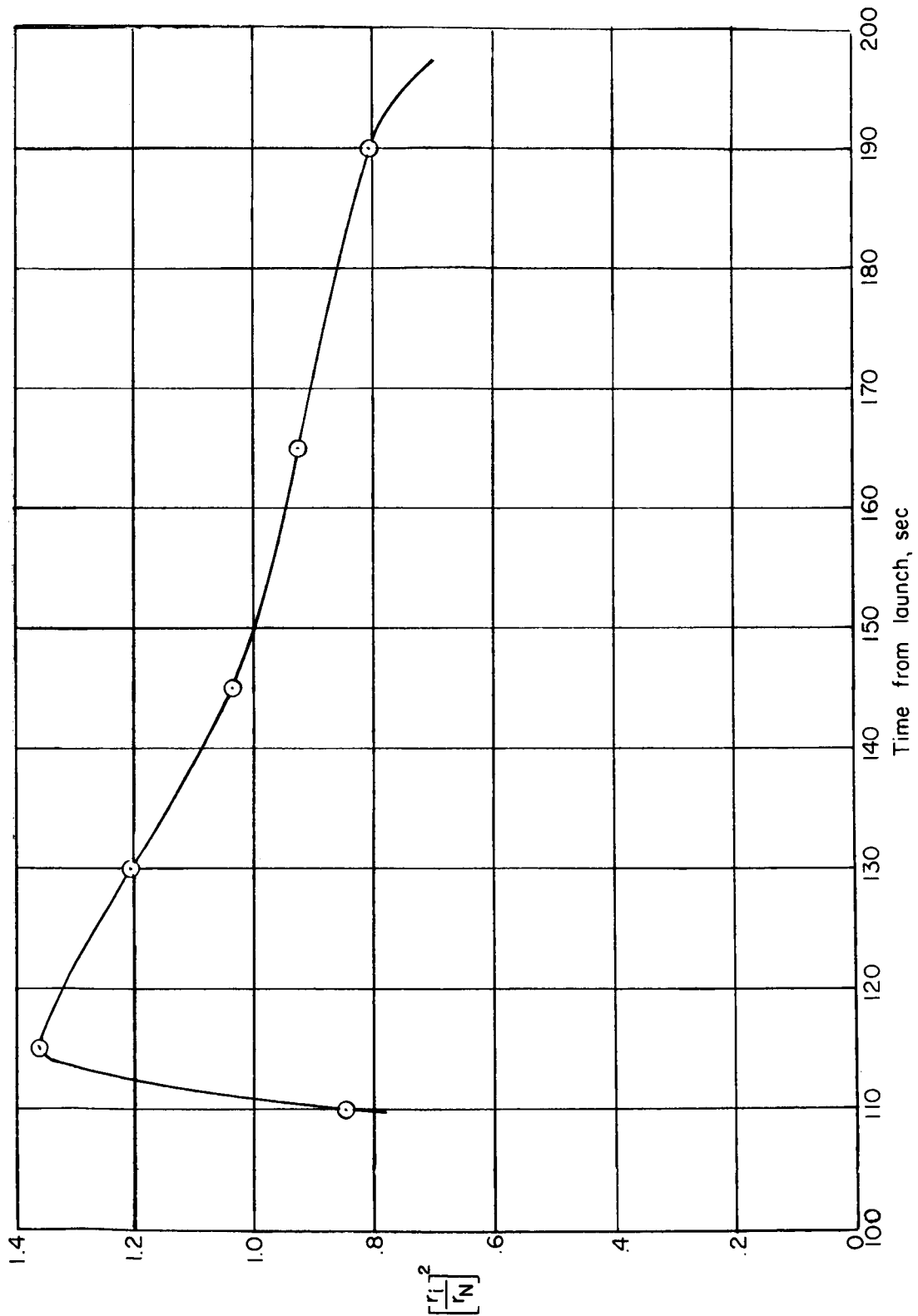
Figure 32.- Variation of $\left(\dfrac{r_i}{r_N}\right)^2$ with time as computed for RAM B2 flight.
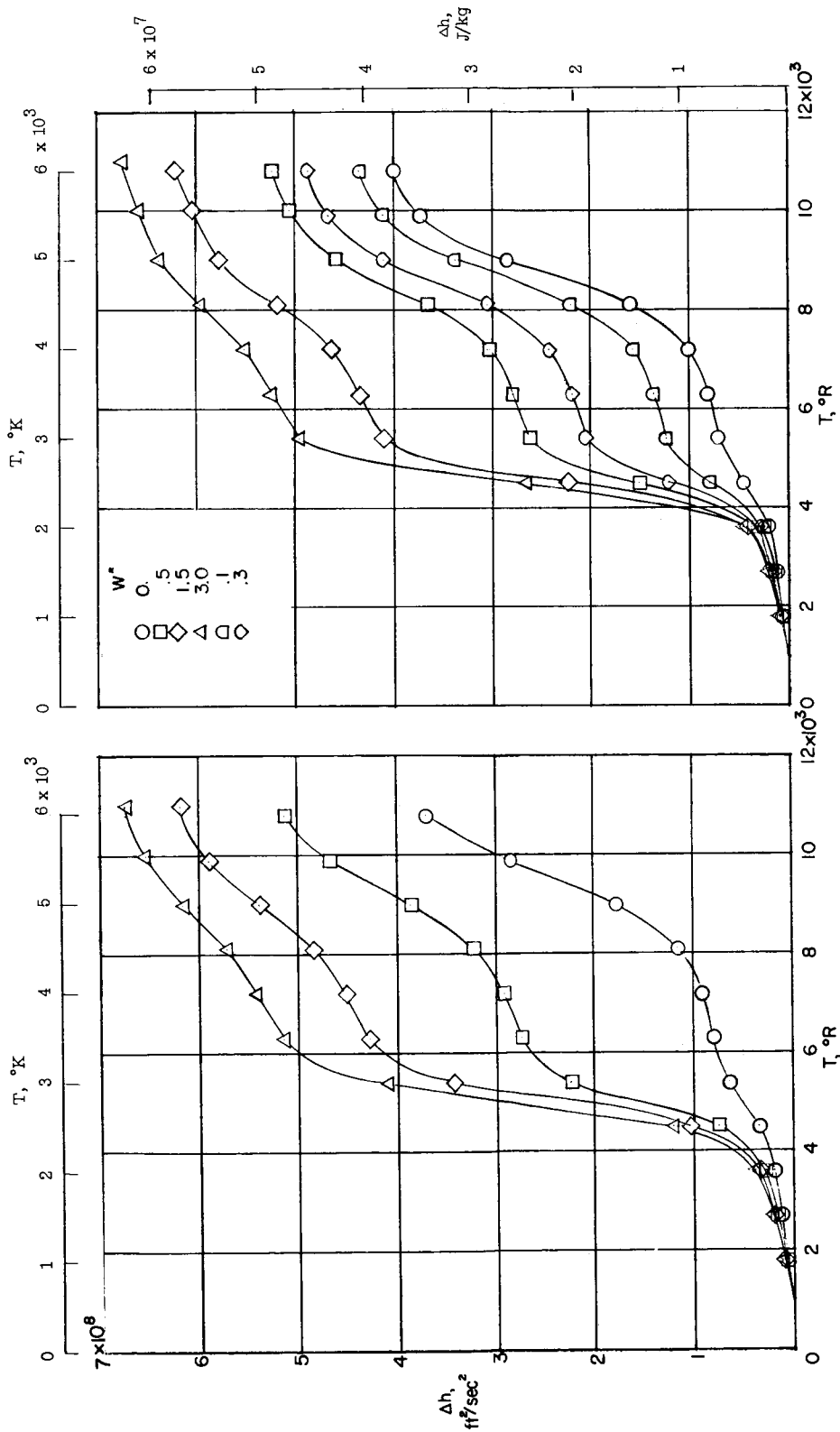
(b) $p = 0.0005$ atm (50.7 N/m^2).

(a) $p = 0.005$ atm (506.6 N/m^2).

Figure 33.- Variation of enthalpy with temperature for various values of W^* (mass ratio of water vapor to air) as obtained for $T_{ref} = 900^0$ R (500^0 K).
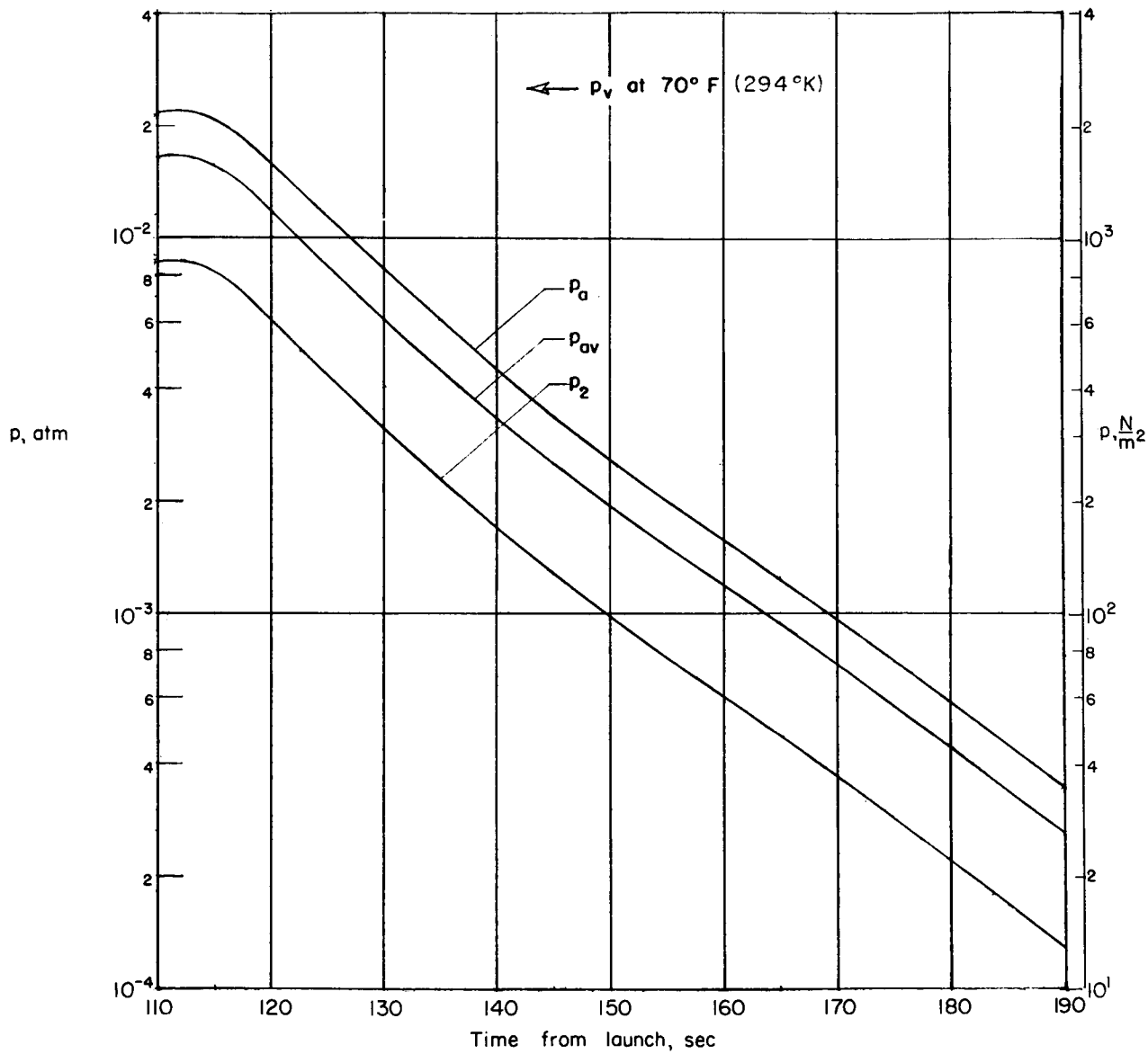
Figure 34.- Typical flow-field pressure for RAM B2 flight based on normalized pressure coefficients of $\overline{C}_{p,a} = 0.06$, $\overline{C}_{p,av} = 0.044$, and $\overline{C}_{p,2} = 0.021$. (See ref. 38.)
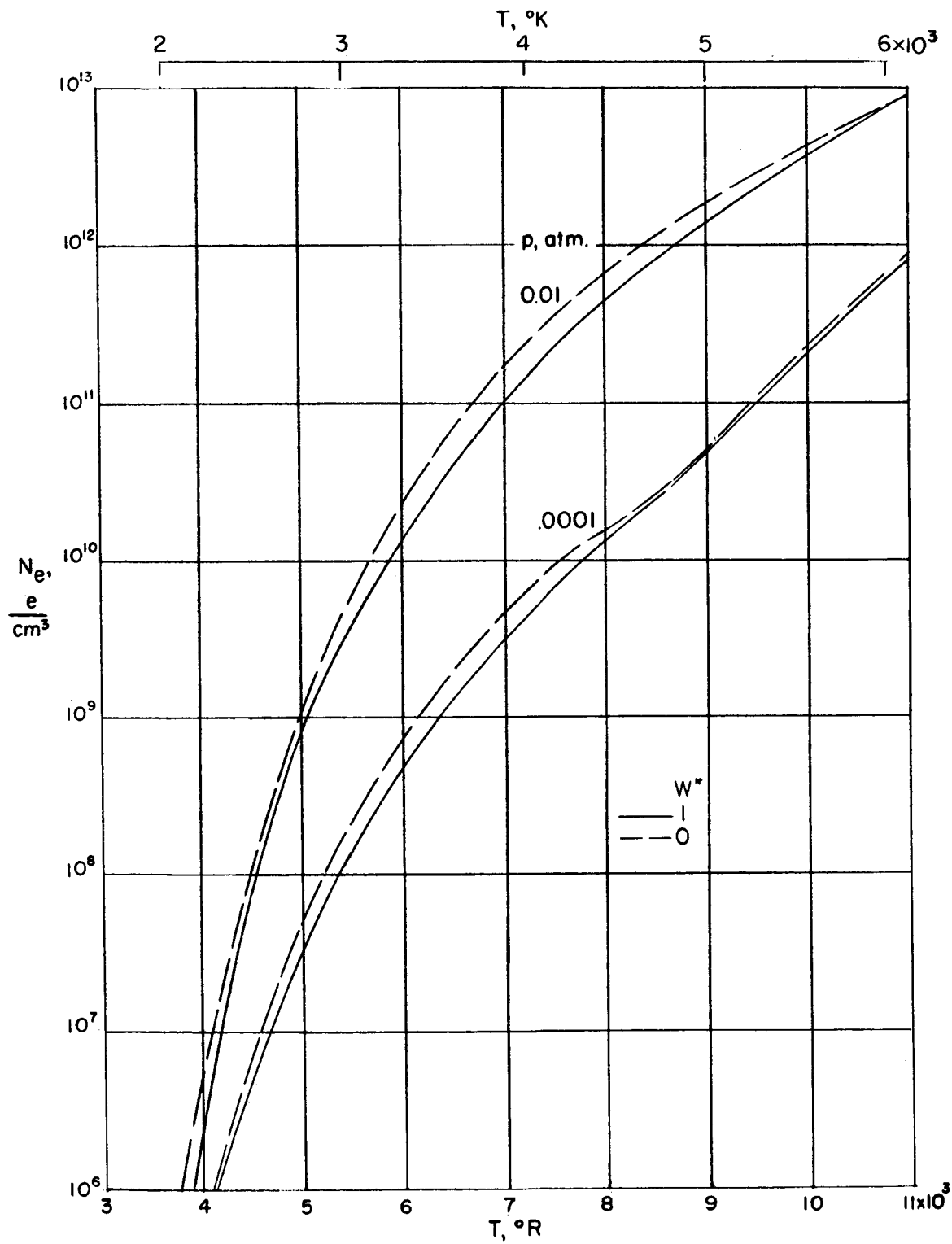
Figure 35.- Electron concentration for equilibrium mixtures of air and water vapor.
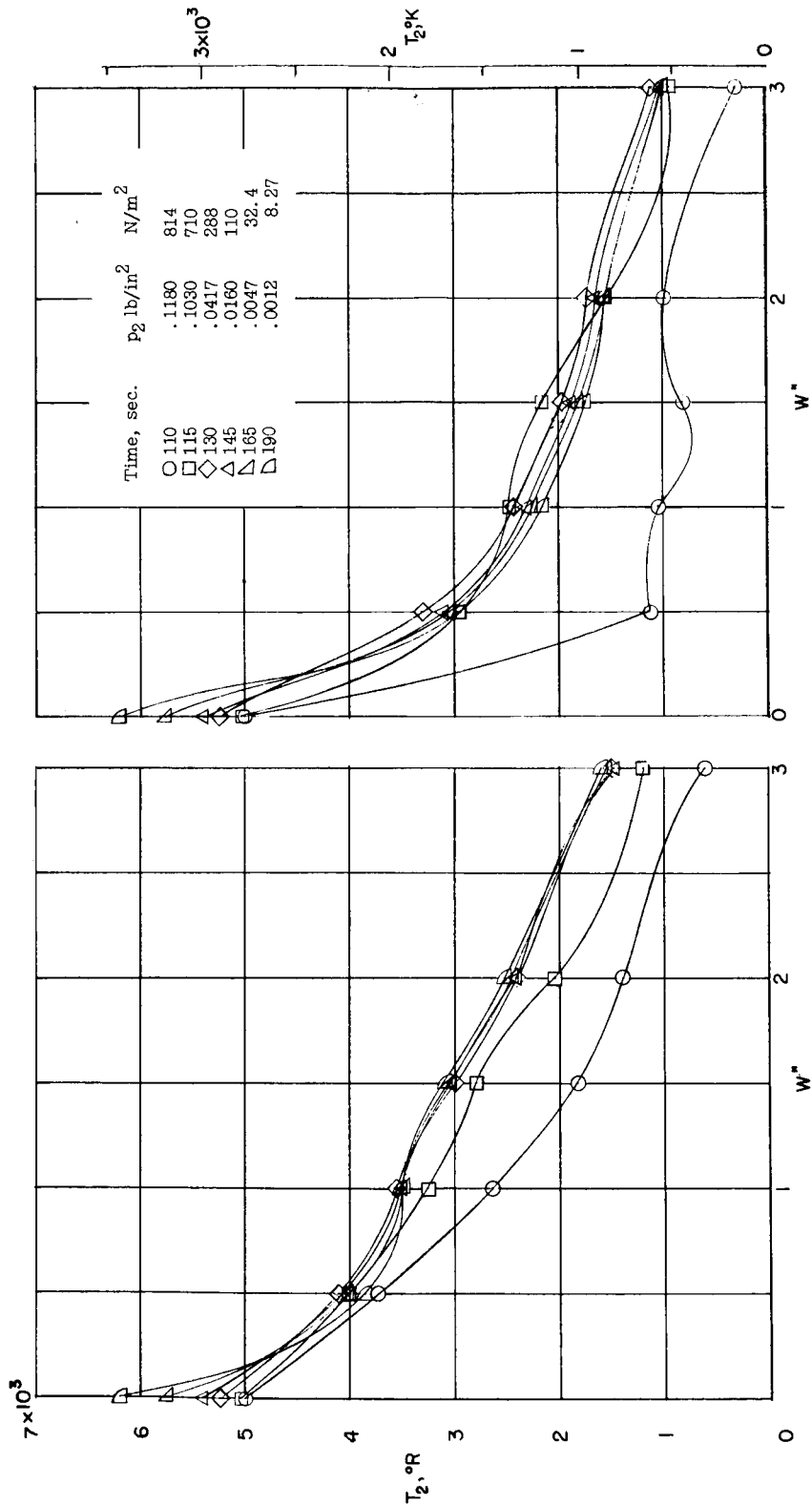
(b) Stagnation injection. $C_{D,B} = 0.06$.

(a) Side injection. $C_{D,B} = 0.30$.

Figure 36.- Variation of computed mean flow-field temperature at station 2 with coolant mass flow ratio W^* at several trajectory times on RAM B2 flight.
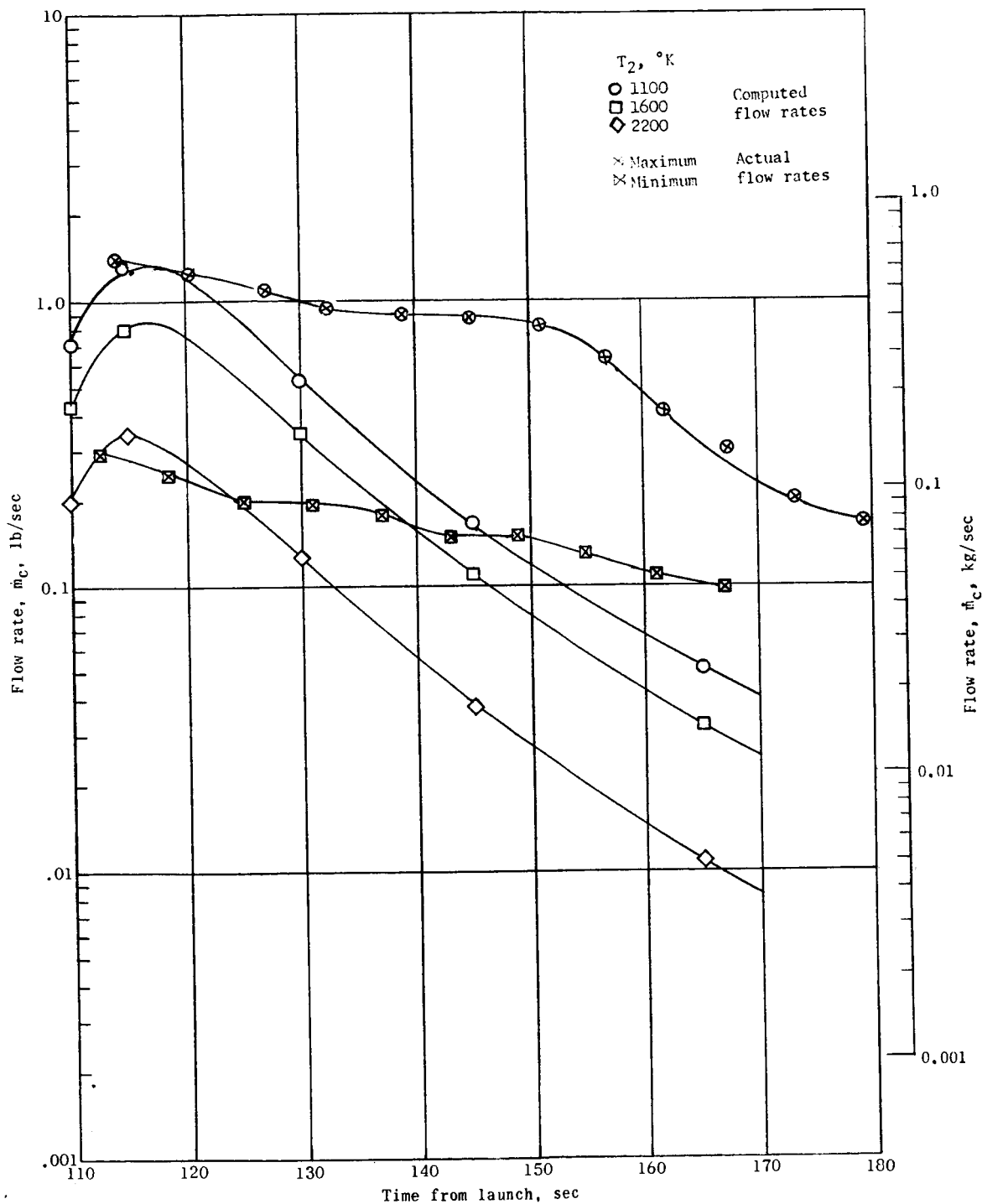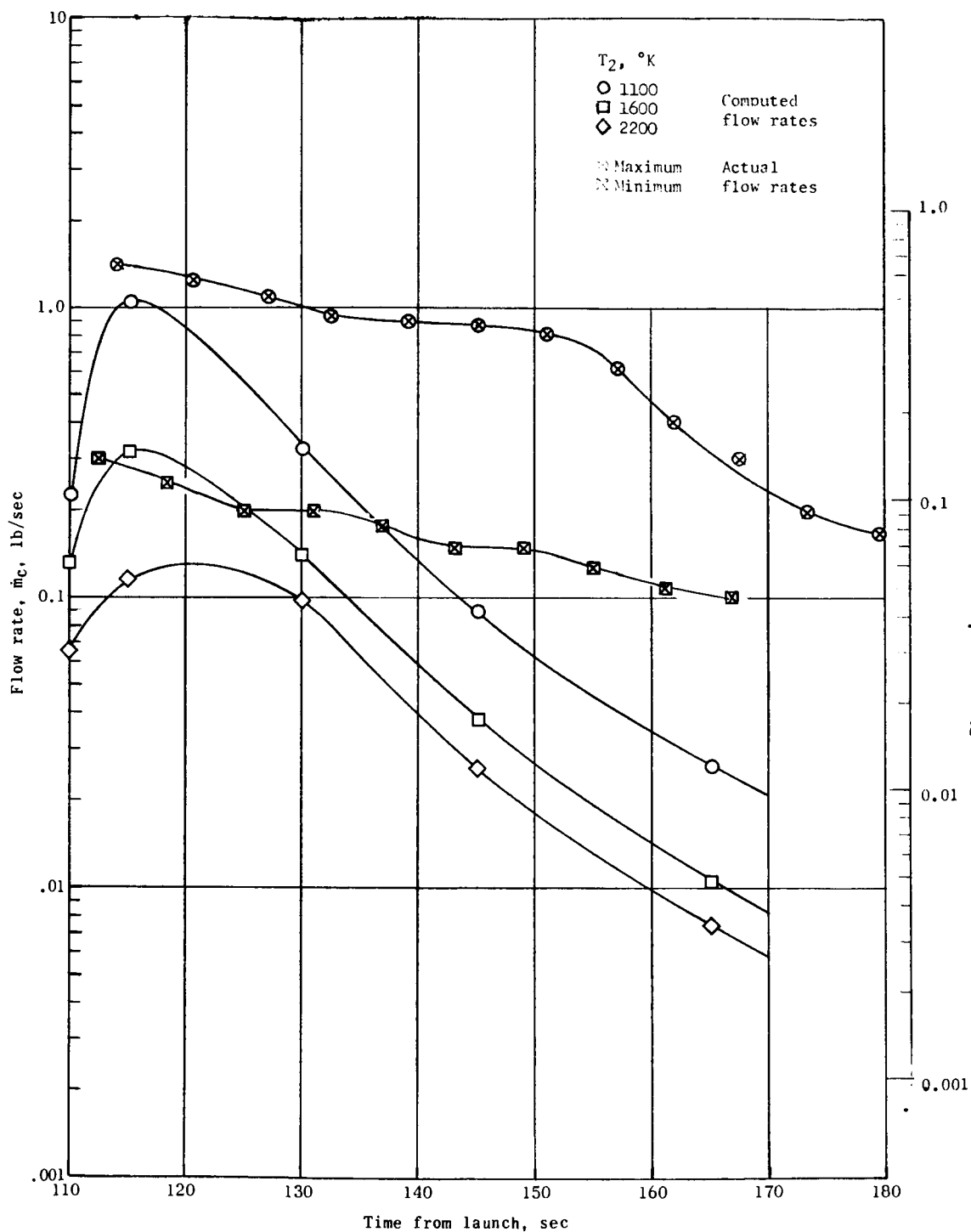
(a) Maximum body drag corresponding to small injection rates.

Figure 37.- Comparison of computed flow rates with actual flow rates for injection from stagnation nozzles.

(b) Minimum body drag corresponding to large ratios of injected momentum to stream momentum.
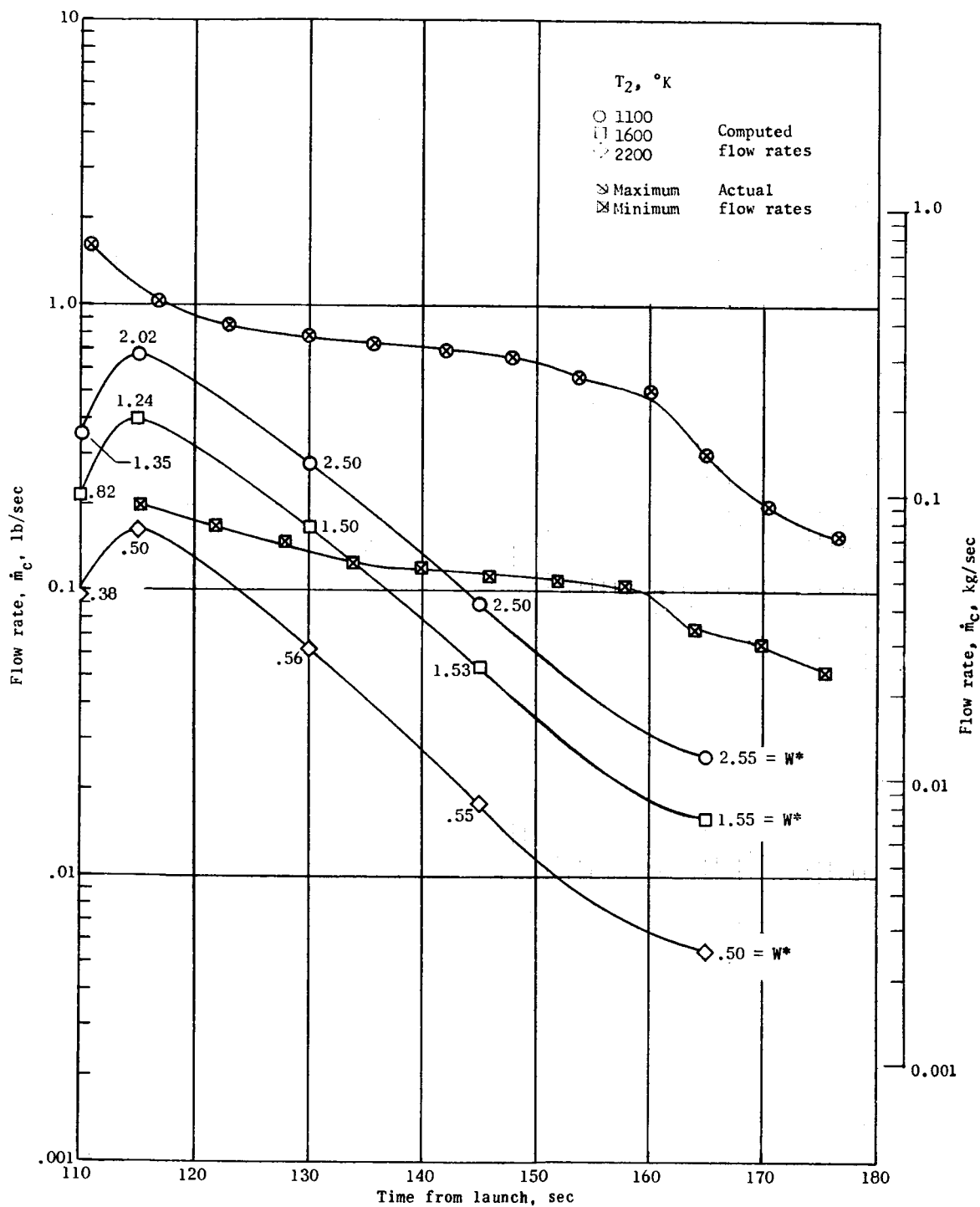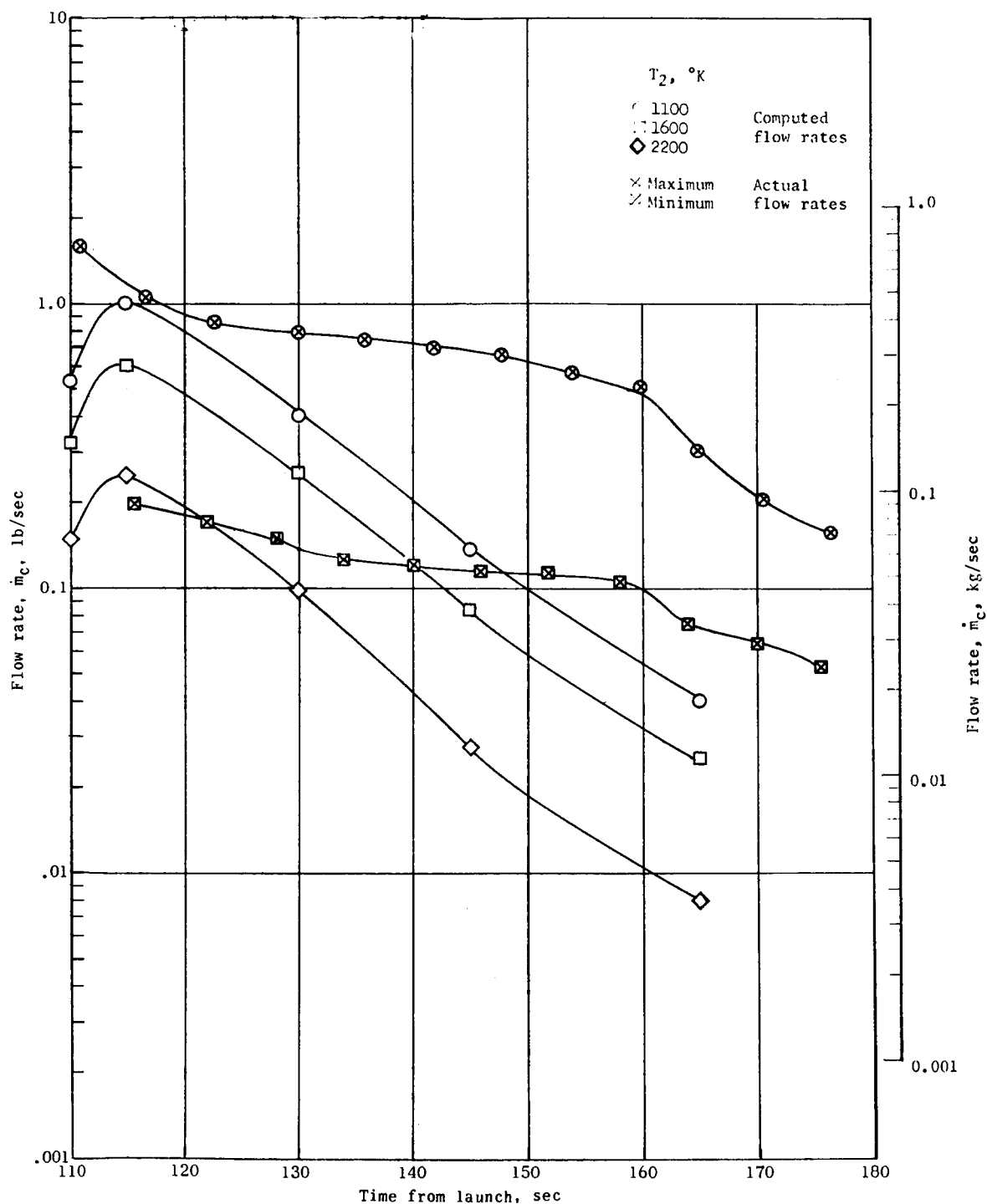
Figure 37.- Concluded.

(a) $f_i = 0.5$.

Figure 38.- Comparison of computed water flow rates with actual flow rates for side injection. The numbers are values of W^* obtained for specified temperatures.
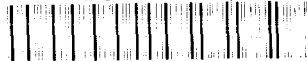
(b) $f_i = 0.75.$

Figure 38.- Concluded.

NASA Technical Library

‖‖‖‖‖‖‖‖‖‖‖‖‖‖‖‖‖‖‖‖‖‖‖

3 1176 01473 7523

"The aeronautical and space activities of the United States shall be conducted so as to contribute . . . to the expansion of human knowledge of phenomena in the atmosphere and space. The Administration shall provide for the widest practicable and appropriate dissemination of information concerning its activities and the results thereof."

—NATIONAL AERONAUTICS AND SPACE ACT OF 1958

NASA SCIENTIFIC AND TECHNICAL PUBLICATIONS

TECHNICAL REPORTS: Scientific and technical information considered important, complete, and a lasting contribution to existing knowledge.

TECHNICAL NOTES: Information less broad in scope but nevertheless of importance as a contribution to existing knowledge.

TECHNICAL MEMORANDUMS: Information receiving limited distribution because of preliminary data, security classification, or other reasons.

CONTRACTOR REPORTS: Technical information generated in connection with a NASA contract or grant and released under NASA auspices.

TECHNICAL TRANSLATIONS: Information published in a foreign language considered to merit NASA distribution in English.

SPECIAL PUBLICATIONS: Information derived from or of value to NASA activities. Publications include conference proceedings, monographs, data compilations, handbooks, sourcebooks, and special bibliographies.

TECHNOLOGY UTILIZATION PUBLICATIONS: Information on technology used by NASA that may be of particular interest in commercial and other nonaerospace applications. Publications include Tech Briefs; Technology Utilization Reports and Notes; and Technology Surveys.

Details on the availability of these publications may be obtained from:

SCIENTIFIC AND TECHNICAL INFORMATION DIVISION

NATIONAL AERONAUTICS AND SPACE ADMINISTRATION

Washington, D.C. 20546